In compliance with the
Canadian Privacy Legislation
some supporting forms
may have been removed from
this dissertation.

While these forms may be included
in the document page count,
their removal does not represent
any loss of content from the dissertation.

# University of Alberta

Experimental Study on the Speciation and Solubility of Sulfur, and the Behavior

of Highly Siderophile Elements in Sulfide- and Sulfate-saturated Basaltic Melts

at 1300 °C and 1 GPa

by

Pedro J. Jugo  Ⓒ

A thesis submitted to the Faculty of Graduate Studies and Research

in partial fulfillment of the requirements for the degree of

Doctor of Philosophy

Department of Earth and Atmospheric Sciences

Edmonton, Alberta

Fall 2003

# Canadä

# University of Alberta

## Library Release Form

**Name of Author:**    Pedro J. Jugo

**Title of Thesis:**    Experimental Study on the Speciation and Solubility of Sulfur, and the Behavior of Highly Siderophile Elements in Sulfide- and Sulfate-saturated Basaltic Melts at 1300 °C and 1 GPa

**Degree:**    Doctor of Philosophy

**Year this Degree Granted:**    2003

Permission is hereby granted to the University of Alberta Library to reproduce single copies of this thesis and to lend or sell such copies for private, scholarly or scientific research purposes only.

The author reserves all other publication and other rights in association with the copyright in the thesis, and except as herein before provided, neither the thesis nor any substantial portion thereof may be printed or otherwise reproduced in any material form whatever without the author's prior written permission.

Date submitted: September 22, 2003

# University of Alberta

## Faculty of Graduate Studies and Research

The undersigned certify that they have read, and recommend to the Faculty of Graduate Studies and Research for acceptance, a thesis entitled "Experimental Study on the Speciation and Solubility of Sulfur, and the Behavior of Highly Siderophile Elements in Sulfide- and Sulfate-saturated Basaltic Melts at 1300 °C and 1 GPa" submitted by Pedro J. Jugo in partial fulfillment of the requirements for the degree of Doctor of Philosophy.

For Dr. Malcolm J. Rutherford
(Brown University)

Date: September 22, 2003

"Shaping your stone means quietly doing your job, as well as you can. Your identity will soon be lost to history but your stone, if well shaped and polished, will fit into the structure we call civilization and hold its weight, as time sweeps past us and others build upon us. History is full of greed, horror, and the worst in mankind – but *humanness* is built of well-shaped loving lives.

What we do matters, and if there is beauty in the world it is because many quiet souls have shaped their stones well, and the cathedral of life is beautiful after all."

<div align="right">Thomas R. McGetchin</div>

To my parents, Consuelo and Francisco

# Abstract

The speciation and solubility of sulfur, and the solubilities of Pd, Ir, Pt, and Au were investigated in sulfide- and sulfate-saturated basaltic melts between 1300 to 1355 °C and 1.0 to 1.2 GPa. Sulfur solubilities (as wt. % S) of $0.14 \pm 0.02$ wt.% and of $1.5 \pm 0.2$ wt.% were determined for sulfide-saturated and sulfate-saturated experiments, respectively.

Sulfur speciation in the melt changed from $S^{2-}$-dominated ($X(S^{6+})$ = molar $S^{6+}/[S^{6+}+S^{2-}]$) $= 0.03 \pm 0.04$) in sulfide-saturated experiments to $S^{6+}$-dominated ($X(S^{6+}) = 0.81 \pm 0.06$) in sulfate-saturated experiments. This change in speciation was combined with previous data on sulfur speciation in basalts to derive an expression for the change in sulfur speciation as a function of oxygen fugacity.

Models for the change in sulfur solubility as a function of oxygen fugacity were derived. These models predict a decrease in the degree of partial melting required to produce sulfur-undersaturated melts with increasing oxygen fugacity in supra-subduction zone settings. Thus, if the source region is oxidized, the magmas generated can be both sulfur-rich and sulfur-undersaturated at relatively low degrees of partial melting.

Concentrations of $[Pd]_{melt} = 11.9 \pm 1.2$ ppm and $[Au]_{melt} = 4.7 \pm 0.9$ ppm in glasses from sulfate-saturated experiments were much higher than in sulfide-saturated experiments ($[Pd]_{melt} = 0.63 \pm 0.31$ ppm; $[Au]_{melt} = 0.52 \pm 0.08$ ppm). In contrast, platinum concentrations were not affected by oxidation state and were similar in oxidized ($[Pt]_{melt} = 1.6 \pm 0.3$ ppm) and reduced experiments ($[Pt]_{melt} = 1.23 \pm 0.46$ ppm). Iridium

concentrations decreased with increasing oxidation state (from $[Ir]_{melt} = 0.24 \pm 0.08$ ppm in sulfide-saturated experiments to $[Ir]_{melt} = 0.07 \pm 0.02$ ppm in sulfate-saturated experiments).

The results of this work support the hypothesis that oxidation of mantle sulfides in supra-subduction zone settings favors Au-enrichment in the generated magmas, which translates to potentially higher Au-content in associated porphyry and epithermal deposits. Reduction of a relatively oxidized magma by assimilation of carbon-bearing country rocks can trigger sulfide saturation and produce orthomagmatic ore deposits.

Because the solubility of sulfur in oxidized melts decreases significantly with decompression, oxidized, water- and sulfur-rich basaltic magmas are likely to exsolve water- and sulfur-rich volatile phases upon ascent. Therefore, the results are consistent with the contribution of a volatile phase exsolved from basaltic magmas at depth to explain the high-sulfur degassing in some arc-related volcanoes.

# Acknowledgements

First and foremost, I would like to thank my supervisors: Bob Luth and Jeremy Richards for helping in every aspect of my research while giving me enough freedom to pursue this project in my own terms. Their enormous financial, intellectual, and moral support, as well as their patience and tolerance, made this project possible and is greatly appreciated.

Many thanks to my supervisory committee: Tom Chacko, Rob Creaser, Tom Etsell, and Malcolm Rutherford. Their feedback improved this dissertation considerably.

Paul Sylvester and Mike Tubrett from the Department of Earth Sciences at Memorial University of Newfoundland taught me most of what I know about LA-ICP-MS in a very intense and productive week and answered all my questions thereafter. Their assistance with those analyses and everything related to LA-ICP-MS is greatly appreciated.

Diane Caird, Ken Domanik, and Roberta Flemming helped me settle in the C.M. Scarfe Laboratory of Experimental Petrology and created an excellent working environment. Lang Shi and Sergei Matveev provided assistance with everything pertaining to microprobe analyses.

Additional financial support in the form of a Geological Society of America Student Grant and scholarships from the Canadian Association of Petroleum Producers, the Faculty of Graduate Studies and Research, and the Christopher M. Scarfe Memorial Fund made my everyday life easier and fuelled the drive to do the best work I could.

Many thanks to all the people who shared good and bad times with me during my time in Edmonton; special thanks go to Xiomara Cabrera, Suman De, Asuka Forest, Hannah Kim, Carolina Moron, Rajeev Nair, Ana Palmero, Carlos Rivero, Heinz Tesler and the crowd from the Alpine Club of Canada.

Boundless thanks to my parents, Consuelo and Francisco; my sisters, Leonor and Consuelo; my brother Francisco and my brothers-in-law Töennies and Milan; for being the best support team one can dream of.

Last, my deepest thanks to Elisabeth Ronacher, for unlimited inspiration and for keeping me sane, balanced, and exceedingly happy all these years.

# Table of Contents

# List of Tables

# List of Figures

# 1. Introduction

Sulfur is a minor element in the Earth in abundance; however sulfur is associated with metals that are of relevance because of their economic value (e.g., copper, gold, and platinum) or because they provide valuable information about Earth processes (e.g., rhenium and osmium). Because of this, the geochemistry of sulfur in its most common form in igneous rocks, as sulfide, has been widely investigated. The occurrence of sulfur in its oxidized form, as sulfate, was only recognized after anhydrite-bearing ejecta from explosive, sulfur-rich volcanic eruptions in the 1980's and 1990's. Although some studies have addressed the role of oxidation for the generation of anhydrite and high-sulfur volcanic degassing, few have addressed the implications of sulfur oxidation for deep magmatic processes and for the geochemistry of precious and tracer metals. This study is an experimental investigation on the contrasting solubility of sulfur under reduced and oxidized conditions in basaltic melts at pressures and temperatures appropriate for the upper mantle above subduction zones, where evidence of magma generation under oxidized conditions exist. In addition the solubility of Pd, Ir, Pt, and Au in the presence of sulfide and sulfate was also investigated.

## 1.1. Sulfides, highly siderophile elements and mantle processes

The highly siderophile elements (HSE) are those with distribution coefficients between Fe-rich metal and silicate phases that exceed $10^4$, and include Ru, Rh, Pd, Re, Os, Ir, Pt, and Au (O'Neill et al., 1995). Not only are these metals economically important, they are also useful as geochemical tracers. For example, they are critical to understand deep-Earth processes such as core-mantle differentiation and core-mantle chemical exchange (Luguet et al., 2001) and the degree of partial melting of the mantle required to generate primitive melts (Garuti et al., 1997). Because of their siderophile nature, these elements are expected to reside mostly in the Earth's core. They are, however, present in the mantle in concentrations significantly higher than expected from core-mantle equilibria as extrapolated from existent experimental data. The reasons for these observations are

1

still being debated (Rehkamper et al., 1999a, 1999b and references therein). Two contrasting hypotheses exist. The first one, called the "late veneer" model, proposes heterogeneous addition of chondritic material after core-mantle separation (Morgan, 1986). The other model postulates that the Earth accreted homogeneously and that the observed values can be explained by the presence of a deep (800-1000 km) magma ocean in the Earth's early history (Righter and Drake, 1997). The latter model requires a strong pressure dependence of the partition coefficients for the HSE, because low-pressure partition coefficients are too small to account for the observed mantle HSE inventory.

A key point in unraveling much of the HSE behavior resides in understanding their chemical behavior. In the absence of a metallic Fe-rich phase, the HSE behave mostly as chalcophile elements and are thought to be incorporated into sulfide phases (Michael and Keays, 1981; Alard et al., 2002). Measured partition coefficients between sulfide and silicate melts ($D^{sulfide/silicate}$) range from $D_{Os} = (2.3 \pm 0.3) \cdot 10^3$ to $D_{Ir} = (3.1 \pm 0.8) \cdot 10^5$ (Bezmen et al., 1994).

Decades of research on sulfide systems have provided a wealth of information on the behavior of sulfides and associated metals, relevant both for mantle processes and for ore formation. These results are useful to model the behavior of sulfides and the HSE in reducing environments, such as mid ocean ridge basalts (MORB), where sulfides are stable. However, under oxidizing conditions, sulfides are not stable and react to form sulfate. The study of the eruption of the El Chichón volcano in 1982 by Luhr et al. (1984) established that anhydrite could be a primary magmatic mineral. The eruptive products of the 1991 eruption of Mt. Pinatubo in 1991 also contained magmatic anhydrite. This eruption released more than 17 Mt (megatonnes) of $SO_2$ into the atmosphere, highlighting the potential for volcanic degassing to be a significant contributor to climate modification (Gerlach et al., 1996). Baker and Rutherford (1996a) predicted that magmatic anhydrite should be present in plutonic rocks as well. Barth and Dorais (2000) documented this in tonalitic-granodioritic samples from Cajon Pass, California, which contained both magmatic anhydrite and epidote indicating oxidizing conditions and crystallization at mid-crustal depths, respectively. The occurrence and frequency of sulfur-rich and sulfate-

2

saturated eruptions are difficult to evaluate because of the rapid dissolution of anhydrite at Earth-surface conditions (Luhr, 1984; Barth and Dorais, 2000) and additional methods to track cryptic anhydrite saturation have been investigated. For example, Streck and Dilles (1998) used the sulfur concentration in apatite as an indicator of anhydrite saturation in the Yerington batholith, Nevada. They found that the sulfur concentration in apatite changed abruptly from sulfur-rich cores to sulfur-poor rims, and concluded that this late-stage decrease in sulfur concentration was produced by crystallization of anhydrite.

Both Mt. Pinatubo and El Chichón volcanoes are subduction-related volcanoes, and there are other lines of evidence indicating a link between this type of volcanism and oxidizing conditions. Island arc basalts (IAB), generated in the mantle wedge above subduction zones, are typically more oxidized than basalts from other tectonic settings (Ballhaus, 1993; Parkinson and Arculus, 1999). Post-eruptive oxidation (Christie et al., 1986), decompression (Ballhaus and Frost, 1994; Kress and Carmichael, 1991), and other factors affect the evolution of the oxidation state of a magma following separation from its source. However, the consistent differences in oxidation state of magmas produced in different tectonic settings indicate that the oxidation state in the source region of these magmas must be different, with the relatively high oxidation state in IAB possibly resulting from their source being outside the stability field of graphite (Ballhaus, 1993).

Parkinson and Arculus (1999) summarized and evaluated different models for the oxidation state of subduction zones and concluded that oxidation of the source, in the range of 0.5 to 1.7 log units above the oxidation state defined by the fayalite-magnetite-quartz (FMQ) buffer, "must take place before melting of the wedge". This range in oxidation state overlaps the range in which sulfur speciation in basaltic glasses progressively changes from sulfide to sulfate (Nilsson and Peach, 1993; Wallace and Carmichael, 1994; Matthews et al., 1999).

Oxidation of sulfides strongly affects the behavior of the HSE. Richards (1991), McInnes and Cameron (1994) and Sillitoe (1997) suggested that oxidation of sulfides in the mantle

3

wedge releases Au during magma generation and could be a factor in the generation of Au-rich porphyry deposits. Tarkian and Stribrny (1999) showed that Au-rich porphyries in island arcs contain significant concentrations of Pd and Pt, and concluded that the geochemical correlation of Au, Pd, and Pt was evidence of a common origin, likely related to the chemical composition of the upper mantle from which they were derived. Müller et al. (2001) measured the oxidation state of a series of volcanic and plutonic rocks associated with the Ladolam Au-Cu deposit in Lihir Island, Papua New Guinea. From analyses of spinel included in forsteritic olivine ($Fo_{90-91}$) they obtained values of ~FMQ+2.1 (2.1 log units above the FMQ buffer) for olivine basalts. They concluded that lack of sulfide saturation in the parental melts was essential for Au mineralization.

At present, there are no experimental data with which to evaluate the effect of oxidation state on sulfide stability in either peridotitic mineral assemblages or basaltic magmas at mantle conditions. Carroll and Rutherford (1987, 1988) and Luhr (1990) studied the conditions for anhydrite formation and sulfur solubility in felsic to intermediate melts under upper-crustal pressure and temperature conditions, and showed that the solubility of sulfur in the melt increases significantly with increasing oxygen fugacity ($fO_2$) as sulfur speciation changes from dominantly sulfide to sulfate. Carroll and Rutherford (1988) showed that the transition from sulfide- to sulfate-dominated systems occurs between FMQ-2 and FMQ+2 at 1025 °C and 200 MPa for trachyandesite and dacite melts. Luhr (1990) investigated sulfur solubility in intermediate to felsic melts (andesitic and trachyandesitic to rhyolitic) from 800 to 1000 °C and 100 to 400 MPa. He showed that for oxidized, anhydrite-saturated systems (FMQ$\geq$+1) sulfur solubility in the melt increases significantly with increasing pressure and temperature. Based on extrapolation of the pressure and temperature dependencies defined by his data, Luhr (1990, p. 1109) suggested that "vapor-saturated basaltic melt at Benioff zone conditions (T = 1200 °C and P = 30 kbar) could contain 1.5 wt.% $SO_3$, and perhaps as much as 2.5 wt.% $SO_3$".

The effects of oxidation state are not limited to the stability of sulfides and changes in sulfur solubility. Borisov and Palme (2000) showed that changes in oxidation state also have a strong effect on the solubility of HSE in Fe-free melts and possibly in Fe-bearing

4

basaltic melts. Capobianco et al. (1994) showed that, in the absence of sulfides, Pd becomes incompatible whereas Ru and Rh are incorporated in oxide phases. Tredoux et al. (1995) suggested that the HSE are not present in sulfides as solid solution, but rather that they are present as metallic clusters (each cluster composed of 50-100 atoms) enclosed by sulfide melts. Supporting evidence for this model is provided by Ballhaus and Sylvester (2000) who found inclusions of Os-Ir-Pt alloy in sulfides from the Merensky Reef of the Bushveld Complex. They concluded that the alloys could not be formed by exsolution because they also occurred in phases that do not contain HSE in solid solution (e.g., olivine). In oxidized, sulfide-free melts, partitioning of HSE would be controlled by alloy-melt equilibria, not by sulfide-melt equilibria. In this case, the central assumption of sulfide hosting HSE that has been used to model the behavior of HSE ore formation, and as tracers of mantle processes, would need to be revised.

## 1.2. Objectives

The goals of this project are to determine how changes in oxidation state and the transition from sulfide to sulfate dominance affect sulfur solubility of a basaltic melt at upper mantle conditions, and the implications that this transition can have for the behavior of HSE, both as tracers of mantle processes and in the formation of ore deposits associated with magmatism. Several models to explain the behavior of HSE during partial melting are based solely on the assumption that dissolution-precipitation of sulfides is the main controlling factor affecting the concentration of these elements (e.g., Peach et al., 1990; Solomon, 1990; Keays, 1995; Wyborn and Sun, 1994). Keays (1995), for example, estimated that 25% of partial melting would be needed to dissolve the sulfides present in the mantle source and that only after sulfides are eliminated by dissolution would a silicate melt become enriched with HSE relative to a melt formed under sulfide-saturated conditions. An alternative model, in which sulfides in the mantle wedge are eliminated by oxidation (e.g., Richards et al., 1991, 1995; Sillitoe, 1997; Keith et al., 1998; Hattori et al., 2002; Mungall, 2002) is compatible with estimations of the oxidation state in arc magmas (Ballhaus, 1993). This model has not been tested experimentally, and is the main subject of this project.

5

Within the broad goals outlined above, three objectives were defined at the initial stages of this project as the focus for research:

1. To constrain the critical degree of partial melting at which sulfides are dissolved and a primitive melt is at sulfur saturation.
2. To investigate the effects of water on the redox state of the system and the stability of the sulfides.
3. To constrain the conditions that favor Cu, Au, and platinum group elements (PGE) release from sulfide phases into a primitive melt.

During the course of the investigations, technical problems associated with the use of water in sulfur-bearing experiments could not be solved and thus the second objective had to be abandoned. The other two objectives, both related to the stability of sulfides, were treated in relation to changes in oxidation state that would oxidize sulfides relative to sulfate. For the completion of this project, I:

1. Devised an experimental protocol to produce experimental runs of basaltic composition saturated in a sulfate-phase at pressures and temperatures appropriate for the upper mantle.
2. Obtained the first available data on the solubility of sulfur in basaltic melts at sulfate saturation.
3. Derived a relation for sulfur speciation as a function of oxidation state for basaltic magmas.
4. Produced three models to help constrain the changes in sulfur solubility in a basaltic melt as a function of oxidation state.
5. Produced three models to help constrain the degree of partial melting that would be needed to generate sulfur-undersaturated (relative to either sulfide or sulfate) basaltic melts as a function of oxidation state.
6. Determined the solubility of Pd, Ir, Pt, and Au in sulfide-saturated and oxidized, sulfide-free basaltic melts, and investigated their contrasting chalcophile and siderophile affinities.

6

# 2. Experimental and analytical methods

## 2.1. Starting materials

The experiments in this study are intended to simulate conditions of partial melting of a fertile mantle under pressures and temperatures appropriate for the upper mantle above subduction zones. Thus, the selection and preparation of starting materials that would yield a basaltic melt coexisting with a lherzolitic residue was the first requirement. The second requirement was that the silicate melts be saturated in a sulfur-bearing phase. Sulfur saturation was investigated for sulfide- and sulfate-saturated systems; therefore, both sulfides and sulfates were used as starting material. To investigate the effects of sulfur speciation and solubility on the HSE, Pd, Ir, Pt, and Au were added to most experiments. Additional phases (olivine, water, brucite, and hematite) were added to some experiments to modify bulk composition, stabilize olivine, or promote oxidation of sulfides.

Another requirement was that the melt pockets and the mineral phases produced in the runs be large enough for chemical analyses. This was typically not a problem for mineral phases, which can be analyzed to diameters as small as a few micrometers for major elements by electron probe microanalysis (EPMA). Melt pockets needed to be much larger to allow trace-element chemical analyses by laser ablation inductively coupled plasma mass spectrometry (LA-ICP-MS), which uses a larger beam size ($\sim 50 \ \mu$m) than EPMA. Thus, experimental conditions that would produce large amounts of melt coexisting with a lherzolitic assemblage and a sulfur-bearing phase were explored.

During the course of this work, results from accumulated experiments were used continuously as feedback to modify the conditions of successive experiments. The following subsections reflect this process.

7

## 2.1.1. Glasses

Possible starting compositions were selected from experimental studies of partial melting (e.g., Jaques and Green, 1980; Robinson et al., 1998; Gaetani and Grove, 1998). Compositions similar to those documented by Gaetani and Grove (1998) were chosen because they were shown to produce experiments "consisting of silicate melt saturated with a mantle peridotite mineral assemblage (Ol + Opx ± Cpx ± Sp ± Grt)" with "large areas (~100-700 $\mu$m) of pristine glass in each experimental charge" (Gaetani and Grove, 1998, p. 324).

Four synthetic glasses were prepared for this study, and their compositions are shown in Table 2.1. One glass (B302) was prepared to match the composition of the glass produced in run B302 of Gaetani and Grove (1998), simplified by eliminating Mn, K, and P, which are minor and trace elements and do not affect the equilibria studied here. This composition was selected because it coexisted with an assemblage of olivine, clinopyroxene, orthopyroxene, and spinel at upper mantle pressure and temperature (1.6 GPa and 1350 °C) under anhydrous conditions and had the highest proportion of spinel from all the experiments documented in Gaetani and Grove (1998). Stability of olivine and spinel was of interest because these two phases can be used to estimate the oxidation state of the experiments as discussed in section 2.4.1.

To test for equilibrium (as explained in section 2.4) two other glasses were prepared. One of the glasses (low-Ca-glass) was prepared to have less CaO and the other (low-Fe-glass) to have less FeO than a target (reference) composition. The purpose is to be able to produce identical bulk compositions, including 5 wt.% $SO_3$ (2 wt.% S), when the requisite amounts of $CaSO_4$ or $FeSO_4$ were added. Thus, a 10.76:1 mixture (by wt.) of low-Ca-glass + $CaSO_4$ can be prepared to have identical bulk composition to a 9.54:1 mixture (by wt) of low-Fe-glass + $FeSO_4$. The starting material for run B302 in Gaetani and Grove (1998) (analogous to a 70:30 wt basalt:peridotite mixture, and simplified by eliminating Mn, K, and P) was used as the reference composition.

8

Table 2.1. Composition of glasses and olivine (KR-37)
used as starting materials.

| | KR-37 | B302 | low-Ca-glass | low-Fe-glass | high-Cr-low-Fe-glass |
|---|---|---|---|---|---|
| $SiO_2$ | 40.4(2) | 46.9(4)[a] | 48.9(3) | 49.2(3) | 48.8(3) |
| $TiO_2$ | | 0.67(4) | 0.49(3) | 0.50(4) | 0.50(2) |
| $Al_2O_3$ | | 17.6(1) | 15.28(9) | 15.6(1) | 15.50(8) |
| $Cr_2O_3$ | | 0.10(2) | 0.15(2) | 0.24(3) | 0.50(1) |
| FeO | 9.1(2) | 9.0(1) | 8.2(1) | 3.37(6) | 3.35(4) |
| MgO | 50.0(3) | 12.8(2) | 19.7(3) | 19.8(3) | 19.6(1) |
| CaO | 0.04(2) | 10.8(1) | 5.95(7) | 9.7(1) | 9.60(7) |
| $Na_2O$ | | 2.1(2) | 1.6(1) | 1.7(3) | 1.91(4) |
| | | | | | |
| Total | 99.5 | 99.9 | 100.3 | 100.2 | 99.8 |
| Mg# | 0.907 | | | | |
| n[b] | 15 | 87[c] | 30[c] | 27[c] | 10 |

Notes: [a] units in parenthesis are the 1σ-uncertainties associated with the last significant figure.
[b] n refers to number of spot analysis on each sample.
[c] used in several EPMA sessions as internal standard to test calibration for glass analyses.

A fourth glass, labeled "high-Cr-low-Fe-glass" was prepared and used to promote spinel saturation and growth. Its composition is similar to the low-Fe-glass but with 0.5 wt.% $Cr_2O_3$. This glass was prepared because in some cases the other glasses used as starting material failed to saturate in spinel or grew spinels that were too small (less than 1-2 $\mu$m) for microprobe analysis. Glass B302 and glasses low-Ca-glass and low-Fe-glass were combined in some experiments to try to control the melt fraction in the run products (because glass B302 is less refractory, it should help to produce larger melt pockets).

All glasses were prepared from high purity oxides and carbonates. Oxides were sintered at 1000 °C for 24 h at 1 atm before use. Weighed oxides and carbonates were mixed thoroughly by grinding in an agate mortar under ethanol for one hour, then heated at 350 °C for 4 h to decarbonate the mixture. The mixture was then fused in a Pt crucible at 1400 °C and 1 atm (in air) for 30 minutes, and quenched by dipping the crucible in water. Randomly selected pieces of quenched glasses were inspected on a petrographic microscope at 200x for the presence of crystals. Partially crystalline glasses were reground and reheated at higher temperatures, the choice of temperature increase

9

depending on the degree of crystallization observed, and typically in multiples of 25 °C. The procedure was repeated until quenched glasses were optically homogeneous and free of crystals. Cr-rich mixtures were the most refractory and required 1550 °C for complete melting. All other glasses were homogeneous and crystal free after melting at 1420 to 1450 °C. Fusion times were kept at 30 minutes to minimize possible loss of Na. Quenched homogeneous glasses were ground under ethanol a second time and re-melted at the established melting temperatures. Random pieces of the resulting glass were mounted for electron probe microanalysis (EPMA) to test for chemical homogeneity and composition. The rest of the glass was ground, transferred to glass vials and stored in a dessicator.

### 2.1.2. Sulfur

Sulfur was added in three different forms (all synthetic): as FeS, as $CaSO_4$, or as $FeSO_4 \cdot H_2O$ (ferrosulfate monohydrate). The ferrosulfate monohydrate was prepared by dehydrating ferrosulfate heptahydrate ($FeSO_4 \cdot 7H_2O$) at 120 °C (it loses $6H_2O$ at 64 °C). In experiments containing $FeSO_4$ an amount of ferrosulfate monohydrate equivalent to the desired amount of anhydrous Fe-sulfate was loaded into the capsules, which were then heated at 350 °C for 30-60 minutes before welding to remove the remaining $H_2O$ from the charge.

### 2.1.3. Highly siderophile elements

Some HSE were included in most runs. Four HSE elements were used: Au, Pd, Pt, and Ir. Gold and palladium are convenient because they constitute one of the capsule materials used, but gold was used specifically because one of the goals of this project was to understand the behavior of Au in supra-subduction zone settings. Iridium was selected because it complements Pd as representatives of the "I-PGE" and "P-PGE" groups, respectively (Barnes et al., 1985). According to this classification the IPGE group (Ru, Os, Ir) and the PPGE (Rh, Pt, Pd, and Au) are fractionated because of the more refractory

nature of the IPGE, which are assumed to behave as residual during partial melting. Therefore, the Pd/Ir ratio has been used as an indicator of the degree of partial melting (e.g., Garuti et al., 1997). Platinum was selected because, along with Pd, it has been found in association with Au in porphyry deposits associated with island arcs (Tarkian and Stribrny, 1999).

In some experiments, the capsule material ($Au_{75}Pd_{25}$ or $Au_{80}Pd_{20}$ by weight) acts both as container and as the source of gold and palladium. In experiments using graphite capsules, small strips of $Au_{80}Pd_{20}$ foil (fabricated from capsule tubing material) were used as the source for these two metals. Platinum and iridium were added either as powder (pure Ir, pure Pt) or small pieces of wire ($Pt_{80}Ir_{20}$ by weight, 0.2 mm diameter). More details on the type and choice of capsule material are given in section 2.2.

### 2.1.4. Other phases

Initial experiments did not saturate in olivine, which is needed to estimate $fO_2$ as outlined in section 2.4.1, and also required to demonstrate equilibrium with a lherzolitic source. To promote crystallization of olivine, some runs were seeded with small amounts of handpicked olivine crystals ($Fo_{91}$), finely crushed to <325 mesh, which makes the bulk composition slightly more mafic and refractory. The olivine used was from West Kettle River, British Columbia (sample KR-37; Canil et al., 1990). Its composition is shown in Table 2.1.

For some experiments, $Mg(OH)_2$, $Cr_2O_3$, and $Fe_2O_3$ were added, alone or in combination. $Mg(OH)_2$ was added in one run to produce a hydrous melt without saturating a volatile phases, $Cr_2O_3$ was added to promote spinel crystallization and $Fe_2O_3$ was used to oxidize the system from sulfide-dominant to sulfate-dominant.

In a few experiments contained in AuPd capsules, graphite was added to reduce the oxygen fugacity, based on the results of Holloway et al. (1992) who showed that the presence of graphite reduces the system by converting $Fe_2O_3$ to FeO.

11

Tables 2.2 and 2.3 show the starting compositions of the selected runs in terms of phases added, and also contain information about pressure, temperature, and duration of the experiments. Table 2.4 shows the bulk composition of these runs in terms of oxides, HSE and graphite, to facilitate comparison between experiments.

Table 2.2. Composition and run conditions for the first set of experiments.
Only B302-glass and FeS were used as starting materials.

| Run#[a] | 2 | 3 | 4 | 5 | 7 | 10 | 11 | 12 |
|---|---|---|---|---|---|---|---|---|
| Time (h) | 24 | 24 | 24 | 24 | 48 | 1 | 8 | 4 |
| B302-glass[b] | 49.94 | 49.79 | 53.00 | 33.80 | 35.00 | 41.88 | 41.78 | 41.73 |
| FeS | 9.97 | 10.27 | 10.60 | 6.70 | 7.00 | 8.37 | 8.38 | 8.35 |

Notes: [a]All experiments run in graphite capsules enclosed within sealed platinum capsules.
Run conditions were 1355 °C and 1.6 GPa.
[b]All masses in mg

Table 2.3. Composition and run conditions of runs from the
second set of experiments.

| Run # | 26 | 27C | 28C | 30Ca | 30Fe | 34C | 35C | 35 |
|---|---|---|---|---|---|---|---|---|
| | | | | **Paired run** | | | **Paired run** | |
| **Run conditions** | | | | | | | | |
| P (GPa) | 1.1 | 1.1 | 1.1 | 1.2 | 1.2 | 1.2 | 1.2 | 1.2 |
| T (°C) | 1315 | 1315 | 1315 | 1315 | 1315 | 1315 | 1315 | 1315 |
| Time (h) | 4 | 10 | 22 | 6 | 6 | 4 | 2 | 2 |
| Capsule type[a] | AuPd | C-Pt | C-Pt | AuPd | AuPd | AuPd | C-Pt | AuPd |
| | | | | | | | | |
| **Glass type** | | | | | | | | |
| Low-Ca-glass[b] | | 6.70 | 5.46 | 44.80 | | 30.66 | 14.07 | 30.91 |
| Low-Fe-glass | | | | | 41.26 | | | |
| h-Cr-l-Fe-glass[c] | | | | | | | | |
| B302-glass | 49.23 | | | | | 8.39 | | |
| | | | | | | | | |
| **S-bearing phase** | | | | | | | | |
| $CaSO_4$ | 5.29 | 0.58 | 0.58 | 4.17 | | 2.83 | 1.32 | 2.91 |
| $FeSO_4 \cdot H_2O$ | | | | | 5.23 | | | |
| FeS | | | | | | | | |
| | | | | | | | | |
| **Other phases** | | | | | | | | |
| Olivine KR-37 | 2.94 | | | | | | | |
| Ir-powder | 1.33 | 0.12 | 0.06 | 1.13 | 1.41 | 0.52 | 0.65 | 1.43 |
| Pt-powder | | | 0.10 | | | 0.60 | 0.75 | 1.65 |
| $Pt_{80}Ir_{20}$ | | | | | | | | |
| $Au_{80}Pd_{20}$ | | | 2.20 | | | | 1.23 | |
| Graphite | | | | | | 0.49 | | |
| $Cr_2O_3$ | | | | | | | | |
| $Fe_2O_3$ | | | | | | | | |
| $Mg(OH)_2$ | | | | | | | | |

Notes:  [a] AuPd: gold-palladium capsules, C-Pt = graphite capsules enclosed in sealed platinum.
[b] all masses in mg
[c] high-Cr-low-Fe-glass

13

Table 2.3. Composition and run conditions of runs from the
second set of experiments (continued).

| Run # | 50 | 52 | 53 | 54 | 55 | 56 | 57 | 58 | 59 |
|---|---|---|---|---|---|---|---|---|---|
| | | **Paired run** | | **Paired run** | | **Paired run** | | | |
| **Run conditions** | | | | | | | | | |
| P (GPa) | 1.0 | 1.1 | 1.1 | 1.0 | 1.0 | 1.0 | 1.0 | 1.0 | 1.0 |
| T (°C) | 1325 | 1300 | 1300 | 1300 | 1300 | 1300 | 1300 | 1300 | 1300 |
| Time (h) | 4 | 4 | 4 | 4 | 4 | 4 | 4 | 6 | 6 |
| Capsule type[a] | AuPd | AuPd | C-Pt | AuPd | AuPd | AuPd | AuPd | AuPd | C-Pt |
| **Glass type** | | | | | | | | | |
| low-Ca-glass[b] | | | | 35.00 | | 34.75 | | | |
| low-Fe-glass | | | | | 33.08 | | 33.90 | | |
| h-Cr-Fe-glass[c] | | | | | | | | 19.26 | 13.53 |
| B302-glass | 50.33 | 49.14 | 16.40 | 38.45 | 37.09 | 36.13 | 35.96 | 32.18 | 22.60 |
| **S-bearing phase** | | | | | | | | | |
| $CaSO_4$ | 5.03 | | | 3.38 | | 3.20 | | | |
| $FeSO_4 \cdot H_2O$ | | 4.95 | 1.65 | | 3.89 | | 4.23 | | |
| FeS | | | | | | | | 1.09 | 0.76 |
| **Other phases** | | | | | | | | | |
| Olivine KR-37 | 5.04 | 4.92 | 1.64 | 1.99 | 1.85 | 1.81 | 1.81 | 2.31 | 1.62 |
| Ir-powder | | | | | | | | | |
| Pt-powder | | | | | | | | | |
| $Pt_{80}Ir_{20}$ | 1.12 | 1.14 | 0.52 | 1.28 | 1.02 | 0.94 | 0.90 | 0.85 | 0.94 |
| $Au_{80}Pd_{20}$ | | | 0.51 | | | | | | 0.77 |
| Graphite | | | | 0.84 | 0.77 | | | | |
| $Cr_2O_3$ | | | | 0.44 | 0.39 | 0.11 | 0.11 | | |
| $Fe_2O_3$ | | | | | | | | 2.17 | 1.52 |
| $Mg(OH)_2$ | | | | | | | | 2.18 | 1.53 |

Notes:   [a] AuPd: gold-palladium capsules, C-Pt = graphite capsules enclosed in sealed platinum.
     [b] all masses in mg
     [c] high-Cr-low-Fe-glass

14

Table 2.4. Bulk composition (in wt.%) of runs in Table 2.3 in terms of major oxides, HSE, sulfur, and graphite.

| Run# | 26 | 27C | 28C | 30Ca | 30Fe | 34C | 35C | 35 |
|---|---|---|---|---|---|---|---|---|
| $SiO_2$ | 42.3 | 44.9 | 44.1 | 44.6 | 44.1 | 45.1 | 44.6 | 44.6 |
| $TiO_2$ | 0.57 | 0.45 | 0.44 | 0.45 | 0.45 | 0.49 | 0.45 | 0.45 |
| $Al_2O_3$ | 15.1 | 14.0 | 13.8 | 13.9 | 14.0 | 14.7 | 13.9 | 13.9 |
| $Cr_2O_3$ | 0.09 | 0.14 | 0.14 | 0.14 | 0.22 | 0.13 | 0.14 | 0.14 |
| FeO | 8.2 | 7.5 | 7.4 | 7.5 | 7.8 | 7.8 | 7.5 | 7.5 |
| MgO | 13.5 | 18.1 | 17.8 | 18.0 | 17.8 | 16.9 | 18.0 | 18.0 |
| CaO | 13.1 | 8.7 | 9.3 | 8.9 | 8.7 | 9.3 | 9.0 | 9.0 |
| $Na_2O$ | 1.80 | 1.47 | 1.44 | 1.46 | 1.53 | 1.59 | 1.46 | 1.46 |
| $SO_3$ | 5.41 | 4.69 | 5.65 | 5.01 | 5.37 | 3.97 | 5.04 | 5.06 |
| **Total[a]:** | 100.0 | 100.0 | 100.0 | 100.0 | 100.0 | 100.0 | 100.0 | 100.0 |
| % | 97.7 | 98.4 | 71.9 | 97.7 | 97.1 | 96.3 | 85.4 | 91.7 |
| $SiO_2$ | 41.3 | 44.2 | 31.7 | 43.6 | 42.8 | 43.4 | 38.1 | 40.9 |
| $TiO_2$ | 0.56 | 0.44 | 0.32 | 0.44 | 0.44 | 0.47 | 0.38 | 0.41 |
| $Al_2O_3$ | 14.7 | 13.8 | 9.9 | 13.6 | 13.6 | 14.1 | 11.9 | 12.8 |
| $Cr_2O_3$ | 0.08 | 0.14 | 0.10 | 0.13 | 0.21 | 0.12 | 0.12 | 0.13 |
| FeO | 8.0 | 7.4 | 5.3 | 7.3 | 7.6 | 7.5 | 6.4 | 6.9 |
| MgO | 13.2 | 17.8 | 12.8 | 17.6 | 17.2 | 16.3 | 15.3 | 16.5 |
| CaO | 12.8 | 8.6 | 6.7 | 8.7 | 8.4 | 8.9 | 7.7 | 8.2 |
| $Na_2O$ | 1.76 | 1.44 | 1.04 | 1.43 | 1.48 | 1.53 | 1.25 | 1.34 |
| $SO_3$ | 5.29 | 4.61 | 4.06 | 4.89 | 5.21 | 3.83 | 4.31 | 4.64 |
| Ir | 2.26 | 1.62 | 0.71 | 2.26 | 2.94 | 1.20 | 3.61 | 3.88 |
| Pt | | | 1.19 | | | 1.38 | 4.16 | 4.47 |
| Au | | | 20.95 | | | | 5.46 | |
| Pd | | | 5.24 | | | | 1.37 | |
| C | | | | | | 1.13 | | |
| **Total[b]:** | 100.0 | 100.0 | 100.0 | 100.0 | 100.0 | 100.0 | 100.0 | 100.0 |
| **Total S[c]:** | 2.12 | 1.84 | 1.62 | 1.96 | 2.08 | 1.53 | 1.72 | 1.86 |

Notes: [a] Top-half of the table: composition of major oxides normalized to 100%
[b] Bottom-half of the table: composition normalized for all components added.
[c] Total sulfur in the charge expressed as elemental sulfur.

15

Table 2.4. Bulk composition (in wt.%) of runs in Table 2.3 in terms of major oxides, HSE, sulfur, and graphite (continued).

| Run# | 50 | 52 | 53 | 54 | 55 | 56 | 57 | 58 | 59 |
|---|---|---|---|---|---|---|---|---|---|
| $SiO_2$ | 42.5 | 42.8 | 42.8 | 45.3 | 45.3 | 45.6 | 45.4 | 44.0 | 44.0 |
| $TiO_2$ | 0.56 | 0.56 | 0.56 | 0.54 | 0.55 | 0.54 | 0.54 | 0.54 | 0.54 |
| $Al_2O_3$ | 14.7 | 14.8 | 14.8 | 15.3 | 15.4 | 15.3 | 15.4 | 15.0 | 15.0 |
| $Cr_2O_3$ | 0.08 | 0.08 | 0.08 | 0.67 | 0.67 | 0.26 | 0.29 | 0.22 | 0.22 |
| FeO | 8.3 | 11.9 | 11.9 | 8.2 | 8.3 | 8.2 | 8.4 | 11.1 | 11.1 |
| MgO | 14.9 | 15.0 | 15.0 | 16.1 | 16.1 | 16.3 | 16.2 | 18.3 | 18.3 |
| CaO | 12.4 | 9.1 | 9.1 | 9.6 | 9.5 | 9.6 | 9.5 | 9.2 | 9.2 |
| $Na_2O$ | 1.75 | 1.76 | 1.77 | 1.72 | 1.77 | 1.73 | 1.76 | 1.80 | 1.80 |
| $SO_3$ | 4.90 | 3.99 | 3.98 | 2.51 | 2.42 | 2.48 | 2.64 | 0.00 | 0.00 |
| **Total[a]:** | 100.0 | 100.0 | 100.0 | 100.0 | 100.0 | 100.0 | 100.0 | 100.0 | 100.0 |
| % | 98.2 | 98.1 | 95.0 | 97.4 | 97.7 | 98.8 | 98.8 | 96.8 | 94.3 |
| $SiO_2$ | 41.7 | 42.0 | 40.7 | 44.1 | 44.3 | 45.0 | 44.8 | 42.4 | 41.3 |
| $TiO_2$ | 0.55 | 0.55 | 0.54 | 0.53 | 0.53 | 0.54 | 0.54 | 0.52 | 0.51 |
| $Al_2O_3$ | 14.4 | 14.5 | 14.1 | 14.9 | 15.0 | 15.1 | 15.2 | 14.4 | 14.1 |
| $Cr_2O_3$ | 0.08 | 0.08 | 0.08 | 0.65 | 0.65 | 0.26 | 0.28 | 0.21 | 0.21 |
| FeO | 8.1 | 11.7 | 11.3 | 8.0 | 8.1 | 8.1 | 8.3 | 12.15 | 11.82 |
| MgO | 14.6 | 14.7 | 14.2 | 15.7 | 15.7 | 16.1 | 16.0 | 17.6 | 17.2 |
| CaO | 12.2 | 8.9 | 8.6 | 9.4 | 9.3 | 9.5 | 9.4 | 8.9 | 8.6 |
| $Na_2O$ | 1.72 | 1.73 | 1.68 | 1.68 | 1.73 | 1.71 | 1.74 | 1.74 | 1.70 |
| $SO_3$ | 4.81 | 3.91 | 3.79 | 2.44 | 2.36 | 2.45 | 2.61 | | |
| Ir | 0.18 | 0.19 | 0.25 | 0.16 | 0.13 | 0.12 | 0.12 | 0.14 | 0.20 |
| Pt | 1.64 | 1.71 | 2.26 | 1.42 | 1.18 | 1.10 | 1.05 | 1.27 | 2.00 |
| Au | | | 1.97 | | | | | | 1.40 |
| Pd | | | 0.49 | | | | | | 0.40 |
| C | | | | 1.03 | 0.99 | | | | |
| **Total[b]:** | 100.0 | 100.0 | 100.0 | 100.0 | 100.0 | 100.0 | 100.0 | 100.0 | 100.0 |
| **Total S[c]:** | 1.92 | 1.57 | 1.51 | 0.98 | 0.94 | 0.98 | 1.04 | 0.66 | 0.64 |

Notes: [a] Top-half of the table: composition of major oxides normalized to 100% (runs 58 and 59 normalized to anhydrous base).
[b] Bottom-half of the table: composition normalized for all components added.
[c] Total sulfur in the charge expressed as elemental sulfur.

16

## 2.2. Capsule materials

The choice of capsule material is critical because it is the major limitation for experiments at oxidizing conditions in sulfur-bearing systems at high temperature. Typical capsule materials for petrological experiments can be grouped into four categories: noble metals and their alloys, graphite, Fe- and Ni-based alloys, and mineral capsules. A general discussion on capsule materials can be found in Luth (1993a). The discussion presented in this section focuses on the factors relevant to S-bearing experiments: reactivity with the charge, melting point, and permeability to $H_2$ and other substances.

With the exception of Au, noble metals (in particular Pt) are inappropriate for Fe- and S-bearing experiments because they react with both Fe and S, resulting in Fe-loss from the charge by formation of Fe-Pt alloy and corrosion of the capsule by formation of PtS. In contrast, Au does not react significantly with Fe or S and was successfully used by Carroll and Rutherford (1987) and Luhr (1990) in sulfur-bearing experiments. However, Au cannot be used for the investigation of basaltic melts because the 1 atm melting point of Au (1064 °C) is significantly lower than liquidus temperatures of basaltic materials (>1200 °C). Gold-palladium capsules constitute an alternative, because alloys with even small quantities of Pd (melting point at 1 atm = 1555 °C) have significantly higher melting points. For example, $Au_{80}Pd_{20}$ alloys (by wt.) melt at 1350 °C and $Au_{75}Pd_{25}$ alloys melt at 1390 °C at 1 atm (Massalski, 1986).

Graphite capsules sealed inside platinum capsules are commonly used in piston cylinder experiments involving Fe-bearing systems. The graphite acts as a liner to prevent or minimize Fe loss to the platinum capsule. However, the disadvantage of using graphite capsules is that they constrain the oxidation state to reducing conditions (Ulmer and Luth, 1991; Holloway et al., 1992) and, therefore, are only usable in studies of reduced systems.

17

Iron based alloys (e.g., Grove, 1981; van der Laan and van Groos, 1991; Righter and Drake, 1999; Mavrogenes and O'Neill, 1999) can be used to control the imposed oxidation state by altering the Fe concentration of the alloy. The range of oxidation state imposed by these alloys, however, is still relatively reducing, such that sulfides would still be the stable form of sulfur.

Mineral capsules are another option, and capsules made of olivine enclosed in platinum have been used (e.g., Takahashi, 1980; Brey et al., 1990). In principle they are used to provide a liner between the charge and the platinum capsule to avoid iron loss. Takahashi (1980) documents a continuous increase of the oxidation state of the charge due to iron loss from the olivine capsule into the platinum capsule. Brey et al. (1990) used thicker olivine capsules and showed that, for the duration of their experiments, iron loss affected only the outermost section of the olivine capsule and not the bores where the charges sit. The disadvantage of olivine capsules is that they are reactive with the charge, which is forced to equilibrate with the olivine. This is a potential problem if, as in this case, the composition of the olivine is to be used for the estimation of the oxidation state in the experiments.

For this research, graphite capsules enclosed in platinum capsules were used for experiments under reducing conditions, and Au-Pd alloy capsules ($Au_{80}Pd_{20}$ and $Au_{75}Pd_{25}$) were used for experiments under oxidizing conditions. Details of the experimental setup for reduced versus oxidized conditions are given in section 2.4.

## 2.3. Experimental methods

An end-loaded solid-media piston-cylinder apparatus (Boyd and England, 1960; Dunn, 1993) was used for the experimental runs. The "hot-piston out" technique was used. Runs were over-pressurized to 1.5 times the desired final pressure before heating. Upon heating, pressure typically drops from 1.5 times to around 0.9 to 1.1 times the desired pressure. Final pressure adjustments are done by increasing pressure with a hand pump or by carefully releasing excess pressure from the pressure line. Pressure was continuously

18

monitored and small variations corrected. Run pressures range from 1.0 to 1.6 GPa. A calibration of the friction correction (see appendix A) demonstrates that the friction correction decreases as temperature increases and that at temperatures higher than 1275 °C the friction correction is negligible. A Bourdon-tube Heise gauge with PSI graduations (0 to 10,000 P.S.I range, 10 P.S.I. graduations; or nominally 0-6 GPa and 0.006 GPa graduations) was used to monitor line pressure. The run pressure was kept within ± 20 P.S.I. of the desired pressure in all runs, which is equivalent to an uncertainty of ± 0.012 GPa nominal pressure.

Sample assemblies of the Kushiro (1976) design, with a diameter of 1.90 cm (0.75 inches) were used in the experiments (Figure 2.1). The sample assemblies consist of an outer talc sleeve surrounding a Pyrex sleeve that jacketed a tapered graphite furnace. The sample volume is centered inside the graphite furnace by top and bottom Alsimag (an $Al_2O_3$-$SiO_2$-$MgO$ ceramic material) plugs and separated from the furnace by an Alsimag sleeve. The sample volume can accommodate one 5 mm OD (outer diameter) capsule up to 16 mm in length, two 3 mm OD capsules side by side or two 5 mm OD capsules (and ~ 8 mm length) on top of each other. Paired experiments consisted of runs with different initial sulfur phases or different capsule material and were meant to test for equilibrium or contrasting oxidation states, respectively. Excess space in the sample volume after loading the capsules was filled with crushed alumina powder. The use of alumina as filler works well for Pt-lined capsules but AuPd capsules are more brittle and tended to break easily when removed from the assembly. Crushed Pyrex was tried without success as AuPd capsules cracked upon quenching with molten Pyrex partially mixing with the run products (those experiments were discarded). The best results were obtained using sintered hematite as filler. Hematite did not attach as much as alumina to the AuPd capsules and eliminated fracturing of the capsules upon quenching.

Run temperatures ranged from 1300 to 1355 °C. Graphite capsules were used over the entire temperature range but Au-Pd capsules were used only below 1325 °C to provide a safety margin in temperature between the run conditions and the melting point of the alloy.

19
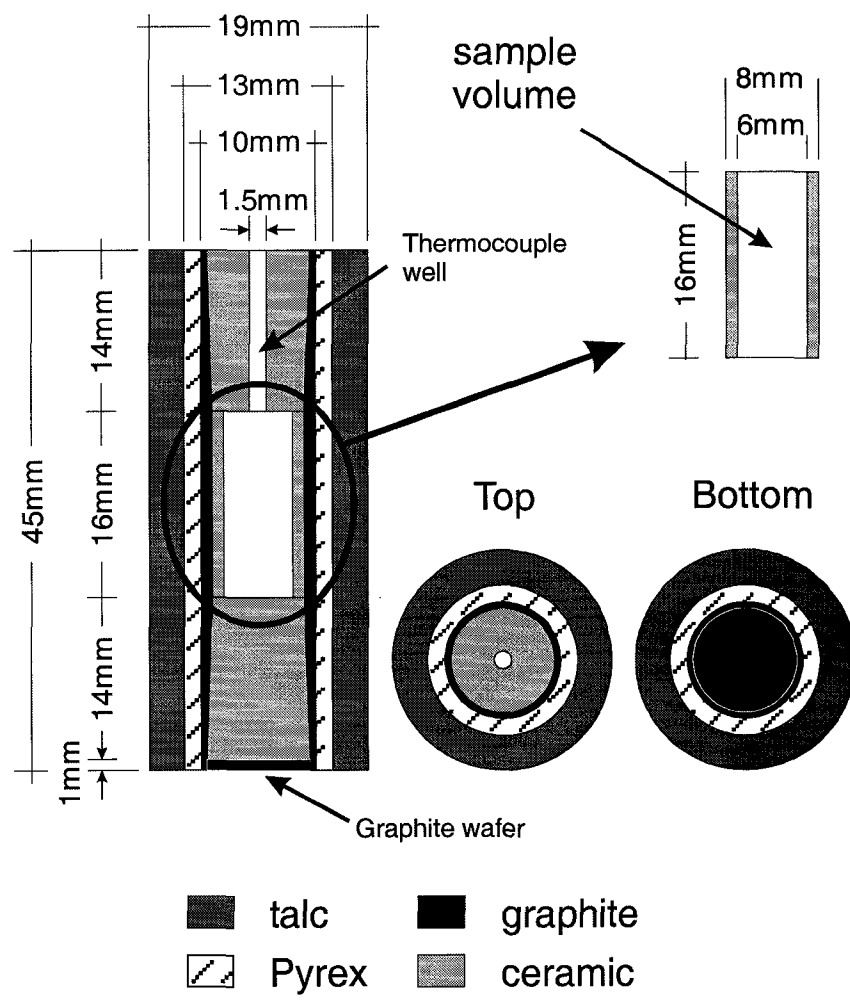
Figure 2.1. Diagram of the solid media assembly used in this study.

Type-C thermocouples constructed from factory-calibrated $W_5Re_{95}$ and $W_{26}Re_{74}$ wires (Omega Corp.) were used to measure run temperatures. The factory calibration was used to calculate the emf (electromotive force) generated by the thermocouples at the desired run temperature and these values were used to set, and monitor, the temperature controller. The thermocouple wires were inserted into a 4-bore (rod = 1.57 mm Ø, bore = 0.41mm Ø) high purity $Al_2O_3$ rod insulator (McDanel Corp.). The ends of the wires were bent over and inserted into the opposite hole in the ceramic, forming a cross pattern such that the thermocouple junction was at the point of overlap of the two wires. Welding of the thermocouple wires was avoided to eliminate problems of oxidation of the wires. Walter and Presnall (1994) documented oxidation of the thermocouples during experiments at pressures lower than 1.1 GPa by ingress of air down the openings in the alumina rod. Thermocouple oxidation, which should result in anomalous emf values, was not observed in the experiments presented here, which can be partially attributed to the shorter duration of this experiments compared to those in Walter and Presnall (1994) which were typically run between 48 and 120 hours.

Temperature uncertainties for type C thermocouples are ~0.1% of temperature in Kelvin or ± 15 °C at 1300 °C (Dunn, 1993). This level of uncertainty is similar to the temperature gradient across the capsule space in pressure assemblies with tapered graphite furnaces like the ones used for these experiments (Kushiro, 1976). Thus, a precision of ± 15 °C is assumed for temperature in all the runs. No correction was attempted for the effects of pressure or pressure gradients on the thermocouple emf.

## 2.4. Control and estimation of oxidation state

The oxidation state of the system in these experiments was estimated relative to that of the fayalite-magnetite-quartz buffer using the olivine and spinel compositions, and the empirical calibration of the olivine-orthopyroxene-spinel equilibria (Ballhaus et al., 1990, 1991). For the discussion that follows, "reducing conditions" refer to those in which only sulfide phases are stable and "oxidizing conditions" to those in which only sulfate phases

21

are stable. The conditions at which both sulfide and sulfate are expected to coexist are referred as "intermediate" conditions.

### 2.4.1. Estimation of the oxidation state

The use of external oxygen buffers to impose an oxidation state on the experiments was not possible for several reasons. External buffers require the presence of a hydrous fluid phase because they are based on the osmotic equilibration of $H_2$ through a permeable membrane (Chou, 1987). Also, the composition of the fluid inside and outside the capsule needs to be as similar as possible because the resulting oxygen fugacity in the charge depends not only on the imposed hydrogen fugacity but also on the partial pressure of other gas species (Luth, 1989, 1993b). Carroll and Rutherford (1985, 1987) and Luhr (1990) used external buffers to control the oxidation state in their vapor-saturated experiments, but this technique could not be used in this project for two reasons. First, preliminary water-saturated experiments invariably quenched to a felt-like mixture of amphibole crystals, such that melt composition could not be inferred. Second, preliminary experiments established that AuPd capsules were not stable in experiments containing sulfate and excess water, probably because this combination resulted in the formation of sulfuric acid, which leached Pd from the capsules, decreasing the melting point of the alloy and producing capsule failure. Therefore, with the exception of two experiments (runs 58 and 59), which were water undersaturated, all the experiments were anhydrous.

To constrain the oxidation state in the experiments, a combination of starting material and capsule material was used. Graphite capsules impose reducing conditions and were used in combination with sulfide- and sulfate-bearing starting materials to produce reduced, sulfide-bearing assemblages. For sulfate-bearing experiments, oxidized starting materials (sulfate-bearing and with glasses fused under air) were enclosed in AuPd capsules. The AuPd capsules do not affect the oxidation state of the system and because the experiments are anhydrous and the packing material acts as a $H_2$ sink (hence, minimizing hydrogen influx to the change) the charge remained oxidized allowing sulfate saturation.

22

The oxidation state of the experiments was estimated using the olivine-orthopyroxene-spinel (ol-opx-spl) oxybarometer calibration of Ballhaus et al. (1990, 1991). This empirical calibration was used because it was shown to be more accurate over a wider range of oxidation states than other available calibrations (Ballhaus et al., 1990) and because it does not require the chemical composition of the orthopyroxene as an input parameter. Although the presence of orthopyroxene is necessary for the application of the ol-opx-spl oxybarometer, Ballhaus et al. (1991) estimated that the correction required for orthopyroxene-undersaturated ultramafic rocks would rarely exceed 0.2 log $fO_2$ units.

Olivine and spinel were analyzed by EPMA. The resulting compositions were converted to mole fractions and the $Fe^{3+}$ content of spinel was calculated using the method of Droop (1987), assuming stoichiometry in the spinels. Estimation of oxidation states from EPMA of spinel has been regarded as inaccurate because of the associated error associated with estimation of $Fe_2O_3$ (Wood and Virgo, 1989; Canil et al., 1990). However, Ballhaus et al. (1991) and Parkinson and Arculus (1999) have shown that the uncertainty decreases as the oxidation state increases because the magnetite component, and hence the amount of total Fe in the spinels, increases. In order to provide an external check on the effect of accuracy of EPMA of spinel on the estimations of oxidation state, two spinel samples (KR-35 and KR-37) with $Fe^{3+}/\Sigma Fe$ previously calibrated by Mössbauer spectroscopy (Canil et al., 1990) were routinely analyzed in every session. The results (discussed in section 4.3) indicate that the oxidation state calculated from $Fe^{3+}$ in spinel estimated from stoichiometry of EPMA for these two samples are consistent with the oxidation state calculated from $Fe^{3+}$ measured by Mössbauer spectrometry.

### 2.4.2. Sulfide-saturated experiments, reducing conditions

Three methods were used to produce sulfide-saturated experiments. In most cases sulfur was added as sulfide and graphite capsules were used as containers. The two other methods produced sulfide-bearing runs from sulfate-bearing starting materials. They are based on the work of Ulmer and Luth (1991) and Holloway et al. (1992) who showed that although graphite capsules do not limit the minimum oxidation state of the experiments,

23

they limit the maximum possible oxidation state to well below the FMQ buffer at the experimental conditions used here. One method was to add sulfur as sulfate and to use graphite as the capsule material; the other was to use sulfate as starting material, AuPd capsules as the container, and add powdered graphite as a reducing agent. This last method was used to estimate how much graphite was needed to reduce the system and also to try to modify the oxidation state of the runs to conditions in which both sulfide and sulfate species are expected to be stable.

Graphite capsules and lids were machined from graphite rods, and polished to the desired dimensions. The outside diameter (OD) of the capsules was designed to fit snugly inside platinum capsules of 3 and 5 mm OD and 0.1 mm wall thickness. The graphite capsules had wall thickness of 0.5 mm, and lids of 1 mm thickness. Capsules with thinner walls, or with outer diameters significantly smaller than the bore of the platinum capsule were unusable because they cracked or deformed easily, resulting in Fe loss to the Pt capsule.

### 2.4.3. Sulfate-saturated experiments, oxidized conditions

Experiments in which AuPd capsules were used and sulfur was added as sulfate were successful in producing sulfate-saturated run products. The addition of sulfur as sulfate and the expected presence of significant amounts of Fe as $Fe^{3+}$ in the starting glasses (fused in air and prepared from $Fe_2O_3$ oxides) coupled with the relatively inert behavior of the AuPd capsules, ensured that the oxidation state imposed by the bulk composition prevailed during the runs.

Several attempts to oxidize sulfides to produce sulfate-saturated assemblages were made throughout this work. Previous experiments (Carroll and Rutherford, 1985, 1987) used excess water coupled with external buffers as an oxidizing agent to produce anhydrite from pyrrhotite. To test this approach, one experiment (run 29) using glass B302, FeS, and excess water, contained in a AuPd capsule was placed in a larger Pt capsule filled with hematite. The hematite acted as a hydrogen sink, producing magnetite at the end of the experiment. The run product did not contain sulfides showing that the approach was

24

effective in oxidizing the sulfides, but the rest of the assemblage consisted only of amphibole needles. Because water saturated-experiments did not quench to glass, other means to oxidize sulfur were used. For example, one experiment (run 58) was performed using a AuPd capsule containing a mixture of glass B302, high-Cr-low-Fe-glass (to promote spinel saturation), FeS, $Fe_2O_3$ (as the main oxidizing agent) and $Mg(OH)_2$ (as source of water and oxidizing agent). This approach effectively consumed the sulfide phase but did not produce saturation of a sulfate phase. Thus, only anhydrous experiments in which sulfur is added as sulfate were successful in saturating a sulfate phase.

### 2.4.4. Sulfate-sulfide bearing experiments, intermediate conditions

Several attempts were made to produce assemblages with coexisting sulfides and sulfate phases. One approach was to mix sulfides and sulfates in identical molar proportions; another was to use sulfates as starting material and use small amounts of graphite as reducing agent. All the experiments used AuPd capsules. None of these approaches succeeded. In some cases sulfides apparently leached Pd from the capsule resulting in capsule failure, whereas in others the amount of graphite added reduced all sulfate to sulfide.

### 2.5. Criteria for estimation of equilibrium

Phase equilibria experiments can use "reversals" as demonstration of equilibrium because deviation from equilibrium, which can be readily achieved by varying P or T, would favor saturation of either reactants or products. For example, to find the equilibration temperature, at a fixed pressure, for the hypothetical reaction:

$$A + B = C + D$$
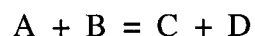
experiments containing only a mixture of A + B would be performed at different temperatures and examined for the appearance of C + D in the run products. If C + D are the high temperature assemblage, the lowest temperature at which C + D can be obtained

in the experiments indicates the temperature of equilibrium. This equilibrium can be demonstrated if phases A + B can be produced from experiments containing C + D (i.e., the "reversal" experiments) at a temperature just below that obtained by the "forward" experiments.

An analogous approach cannot be used in solubility experiments because changes are continuous and cannot be measured by appearance of discrete phases as in the previous example. Two other approaches can be used to suggest attainment of equilibrium in these type of experiments: "time invariance" and approach to the same results from different compositional "directions" by using different starting materials.

Time invariance assumes that after saturation is reached no more changes would occur and hence experiments of different duration (longer than the time required for equilibrium) would show the same result, demonstrating that the charge has reached equilibrium. This approach was used for the first group of experiments, run in graphite capsules and containing FeS, but could not be used for experiments in AuPd capsules because these capsules are not truly inert to the charge. Experiments longer than 6 hours failed repeatedly. EPMA of the capsules revealed that Pd was leached from the capsules, in extreme cases decreasing the melting point such that the alloy melted and in other cases producing areas of weakness that resulted in cracks in the capsule wall and contamination with the packing material.

To test for equilibration in experiments using AuPd capsules, the low-Ca-glass and low-Fe glass starting material described in section 2.1.1 were prepared. The use of these glasses in combination with Ca and Fe sulfates as starting materials allowed monitoring of equilibration from two compositional directions. Assuming that $CaSO_4$ is the stable sulfate phase in the experiments, addition of $CaSO_4$ to the low-Ca-glass should produce a basaltic melt saturated in sulfur and compensated in CaO by the reaction:

$$CaSO_{4\,(anh)} = CaO_{(melt)} + SO_{3(melt)}$$
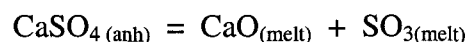
whereas experiments consisting of $FeSO_4$ and low-Fe-glass should produce the same results but following the reaction:

26

$$FeSO_4 + CaO_{(melt)} = FeO_{(melt)} + CaSO_{4 \ (anh)}$$
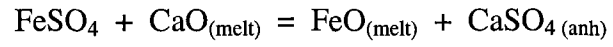
If equilibrium is attained, the CaO and FeO concentration in the silicate melt and the composition of the sulfate phase in the run products should coincide.

27

# 3. Analytical techniques

Two analytical techniques were used in this study. Electron probe microanalysis (EPMA) was used to determine concentrations of major elements in all phases and the concentration and speciation of sulfur in experimental glasses. Concentrations of highly siderophile elements in the experimental glasses were measured by laser ablation inductively coupled plasma mass spectrometry (LA-ICP-MS).

## 3.1. Chemical composition by electron probe microanalysis (EPMA)

Capsules were sliced, in most cases longitudinally and in some cases radially, with a diamond-wafering blade in a low speed saw. They were then mounted in epoxy, polished and carbon coated for EPMA. Major elements in most phases and sulfur in quenched glasses were analyzed by wavelength dispersive spectrometry (WDS) with a JEOL JXA-8900 electron probe microanalyzer at the University of Alberta using mineral, glass and metal standards.

All phases (glasses, silicates, sulfides, oxides, and alloys) were typically analyzed at 15 kV accelerating voltage and 15 nA probe current using the ZAF correction method. Glasses were analyzed with defocused beams of 10 $\mu$m diameter where possible, although in some runs (30Fe and 30Ca) the melt pockets were too small and required reduction of the beam size to 5 $\mu$m diameter. Indian Ocean Basalt (a glass standard) was used as standard for measurements of Si, Ti, Al, Fe, Mg, Ca, and Na; chromite was used for Cr. Both barite and sphalerite were used as standards for sulfur but only barite was used for sulfate-bearing runs. No significant difference was detected in the use of sphalerite or barite in sulfide-bearing runs or when analyzing the Indian Ocean Basalt standard as an unknown ($SO_3$ = 0.30 wt.%). Sodium was analyzed first and at lower counting times to minimize errors caused by Na migration under the electron beam. Typical conditions of analysis (spectrometer and crystal used, counting time at peak and background) are summarized in Table 3.1 for each element.

Table 3.1. Typical measurement conditions for glass analyses, indicating spectrometer, analyzing crystal, and counting times used for each element.

| CH-1 (PET) | | | CH-2 (TAP) | | | CH-4 (PET) | | | CH-5 (LiFH) | | |
|---|---|---|---|---|---|---|---|---|---|---|---|
| elem | pk | bkg | elem | pk | bkg | elem | pk | bkg | elem | pk | bkg |
| Ca | 20 | 10 | Na | 15 | 7.5 | S | 60 | 30 | Fe | 20 | 10 |
| Ti | 40 | 20 | Mg | 15 | 7.5 | | | | Cr | 40 | 20 |
| | | | Al | 15 | 7.5 | | | | | | |
| | | | Si | 15 | 7.5 | | | | | | |

Note: elem. = element, pk = counting time on peak (in s), bkg = counting time on background (in s)

Olivines were typically analyzed with a 3 $\mu$m beam diameter. A $Fo_{93}$ olivine standard was used for Si, Fe, and Mg, diopside for Ca, augite for Al, and hypersthene for Cr. Aluminum was used as a monitor for the presence of spinel inclusions within the activation volume. Typical conditions for olivine analyses are shown in Table 3.2.

Table 3.2. Typical measurement conditions for olivine analyses, indicating spectrometer, analyzing crystal, and counting times used for each element.

| CH-1 (TAP) | | | CH-2 (TAP) | | | CH-4 (PET) | | | CH-5 (LiFH) | | |
|---|---|---|---|---|---|---|---|---|---|---|---|
| elem | pk | bkg | Elem | pk | bkg | elem | pk | bkg | elem | pk | bkg |
| Mg | 20 | 10 | Si | 20 | 10 | Ca | 20 | 10 | Fe | 20 | 10 |
| | | | Al | 20 | 10 | | | | Cr | 20 | 10 |

Note: elem. = element, pk = counting time on peak (in s), bkg = counting time on background (in s)

Analysis of spinels was difficult because they occurred as very small crystals, with cross-sections rarely larger than 3 $\mu$m. They were always analyzed with a spot focused beam (approximately 1 $\mu$m beam diameter). Chromite was used as the standard for Fe and Cr, periclase was used for Mg, corundum for Al, and ilmenite for Ti. A $Fo_{90}$ standard was used for Si, primarily to monitor for the presence of either glass or olivine within the activation volume. Analyses of spinel crystals larger than 3 $\mu$m diameter showed that

29

they contained less than 1 wt.% $SiO_2$; hence, for samples containing very small spinel crystals, only analyses with less than 1 wt.% $SiO_2$ were considered to be acceptable. Typical conditions for spinel analyses are shown in Table 3.3.

Table 3.3. Typical measurement conditions for spinel analyses, indicating spectrometer, analyzing crystal, and counting times used for each element.

| CH-1 (TAP) | | | CH-2 (LiF) | | | CH-4 (TAP) | | | CH-5 (LiFH) | | |
|---|---|---|---|---|---|---|---|---|---|---|---|
| elem | pk | bkg | Elem | pk | bkg | elem | pk | bkg | elem | pk | bkg |
| Si | 30 | 15 | Fe | 30 | 15 | Mg | 30 | 15 | Ti | 30 | 15 |
| Al | 30 | 15 | | | | | | | Cr | 30 | 15 |

Note: elem. = element, pk = counting time on peak (in s), bkg = counting time on background (in s)

Wood and Virgo (1989) analyzed several spinel samples using EPMA applying different correction methods and concluded that values of $Fe^{3+}$ calculated assuming stoichiometry are precise but inaccurate for oxybarometry. They recommended the use of Mössbauer spectroscopy or the use of Mössbauer-analyzed spinels as secondary microprobe standards. Parkinson and Arculus (1999) showed that the problems with calculated $Fe^{3+}$ values are significant for $Fe^{3+}/\Sigma Fe \leq 0.2$ (corresponding to oxidation states below FMQ-1). For $Fe^{3+}/\Sigma Fe \geq 0.2$ the uncertainty associated with the determination of $Fe^{3+}$ from EPMA and stoichiometry become smaller, being insignificant above $Fe^{3+}/\Sigma Fe \geq 0.4$ (roughly FMQ+1).

Pyroxenes were analyzed with 3 $\mu$m or 1 $\mu$m beam diameters. An olivine ($Fo_{90}$) standard was used for Si, Fe and Mg, augite was used for Ca and Al, kaersutite for Ti and Na, and hypersthene for Cr. Typical conditions for pyroxene analyses are shown in Table 3.4.

30

Table 3.4. Typical measurement conditions for pyroxene analyses, indicating spectrometer, analyzing crystal, and counting times used for each element.

| CH-1 (TAP) | | | CH-2 (TAP) | | | CH-4 (PET) | | | CH-5 (LiFH) | | |
|---|---|---|---|---|---|---|---|---|---|---|---|
| elem | pk | bkg | Elem | pk | bkg | elem | pk | bkg | elem | pk | bkg |
| Na | 20 | 10 | Al | 20 | 10 | Ca | 20 | 10 | Fe | 20 | 10 |
| Mg | 20 | 10 | Si | 20 | 10 | Ti | 20 | 10 | Cr | 20 | 10 |

Note: elem. = element, pk = counting time on peak (in s), bkg = counting time on background (in s)

Sulfides and alloys were analyzed at 20 kV and 20 nA using a 1 $\mu$m beam diameter. The narrow beam was used to avoid exsolution lamellae typically found in the quenched sulfides. Pure metals were used as standards for Au, Ir, Pd, and Pd. For these elements the L$\alpha$ X-rays were measured. Pyrite was used as standard for Fe and S. Typical conditions for sulfide and alloy analyses are shown in Table 3.5.

Table 3.5. Typical measurement conditions for sulfide and alloy analyses, indicating spectrometer, analyzing crystal, and counting times used for each element.

| CH-1 (PET) | | | CH-2 (LiF) | | | CH-4 (PET) | | | CH-5 (LiFH) | | |
|---|---|---|---|---|---|---|---|---|---|---|---|
| elem | pk | bkg | Elem | pk | bkg | elem | pk | bkg | elem | pk | bkg |
| Pd | 20 | 10 | Au | 20 | 10 | Pt | 20 | 10 | Fe | 20 | 10 |
| S | 20 | 10 | Ir | 20 | 10 | | | | | | |

Note: elem. = element, pk = counting time on peak (in s), bkg = counting time on background (in s)

## 3.2. Sulfur Speciation

Sulfur speciation was measured using a technique similar to that outlined by Carroll and Rutherford (1988). Operating conditions were 15 kV accelerating voltage, 60 nA probe current and 30 $\mu$m probe diameter. One spectrometer using a pentaerythritol (PET) analyzing crystal was used. Samples were scanned from 5.355 Å to 5.384 Å (535.5 pm to 538.4 pm; 1pm = $10^{-12}$ m) to cover peak and background, with a 0.05 pm step size. Sphalerite and barite were used as reference materials to define the wavelength of the S K$\alpha$ radiation for pure sulfide and sulfate, respectively. The standards were analyzed every two or three samples to monitor spectrometer drift during the sessions. The choice of dwell time depended on the S concentration in the samples. Longer dwell times were needed for sulfide-bearing samples in which sulfur concentration was on the order of 1000 ppm. Dwell times were 2 s for the standards, 30 s for sulfate-bearing samples and 60 s for sulfide-bearing samples. Test on several samples corroborated the effect of long counting times on the peak position for the samples as documented in Metrich and Clocchiatti (1996) and attributed to oxidation of the sample by interaction with the beam. To avoid this problem samples were moved under the beam every 12 minutes as suggested by Gurenko and Schmincke (2000).

The resulting peak profiles were smoothed to reduce noise and the peak position was measured at one-half of the maximum peak height relative to the background. The peak shift between sphalerite and barite from 22 replicate analyses on each standard is 0.304 ± 0.010 pm (1$\sigma$), which is similar to the peak shift documented by Carroll and Rutherford (1988), Wallace and Carmichael (1994), Metrich and Clocchiatti (1996), and Gurenko and Schmincke (1998).

### 3.3. Laser-ablation inductively-coupled-plasma mass-spectrometry (LA-ICP-MS)

Concentrations of HSE in the experimental glasses are very low and below the detection limits for EPMA (i.e., $<\sim$100 ppm). Therefore, laser ablation inductively coupled plasma mass spectrometry (LA-ICP-MS), an analytical technique with detection limits as low as a few ppb, was used instead.

Preliminary measurements were done in the fall of 2001 at the Department of Geological Sciences at the University of Saskatchewan, with the collaboration of Dr. R. Kerrich and Dr. Q. Xie. Analyses were done using a CETAC LSX-200 laser ablation system and a Micromass Platform ICP-MS. The Platform system contains a hexapole collision cell placed at an angle between the plasma source and the quadrupole mass analyzer to reduce the intensity of polyatomic ions and to improve background signal.

The laser used was a solid state Nd:YAG (neodymium-doped yttrium aluminum "garnet", $(Y_{3-x}Nd_xAl_5O_{12})$, frequency quadrupled from the Nd:YAG fundamental wavelength of 1064 nm to produce an ultraviolet laser with a wavelength of 266 nm (fourth harmonic). High intensity is obtained by Q-switched operation to obtain laser energy of up to 6.0 mJ/pulse. Operating laser conditions were: 50 $\mu$m beam diameter with 15 $\mu$m defocusing, 20 Hz laser pulse-rate combined with a laser mode of 100 burst-shots (ca. 5 seconds per spot probed), and 100% energy level (6 mJ/pulse). For both samples and the standard, five analyses were made; background was collected for 180 seconds before the first spot and for 60 seconds between spot analyses. Analyses with ablation diameters of 25 $\mu$m failed to produce significant counts in the standards; therefore, 50 $\mu$m ablation diameters were used.

A glass standard reference material (SRM-612) from the National Institute of Standards and Technology (NIST) was used for Pd, Pt, and Au calibration using nominal values of 1, 2.5, and 4 ppm, respectively. Replicate analysis (n = 5) on the standard were Pd = 1.1 $\pm$ 0.1, Au = 2.6 $\pm$ 0.3, and Pt = 4.6 $\pm$ 0.5. No standard for Ir was available, but Pt was used as a proxy to determine rough Ir concentrations.

33

The concentration of an element (analyte) in a sample from the measurement of one of its isotopes is given by the expression:

$$C_{AN}^{sam} = C_{IS}^{sam} \times \left( R_{AN}^{sam} / R_{IS}^{sam} \right) \times \left( C_{AN}^{std} / C_{IS}^{std} \right) \times \left( R_{IS}^{std} / R_{AN}^{std} \right) \tag{3.1}$$

where C refers to concentration of the element (or oxide), R refers to the count rate of the isotope measured, the subscripts AN and IS mean "analyte" and "internal standard", and the superscript **std** and **sam** mean "in the standard" and "in the sample", respectively (Longerich et al, 1996; Košler, 2001).

In this case, calcium was used as the internal standard with CaO concentrations obtained from EPMA on the samples and the values reported for the standards and count rates measured on $^{43}$Ca isotopes. Measured count rates on $^{105}$Pd, $^{193}$Ir, $^{195}$Pt, and $^{197}$Au were used to calculate the total concentration of those elements in the sample using equation (3.1).

Preliminary analyses yielded concentrations of 6.4 ± 0.8 ppm Au, and 14 ± 3 ppm Pd in sulfate-saturated experimental glasses (run 26). Analyses on glasses in sulfide-bearing experiments failed to detect any HSE except when sulfides were hit in which case sharp peaks, with counts orders of magnitude higher than the counts in the standard, were produced. The most important information from these measurements was that the addition of Ir or Pt to the charge in powder form was a problem because its random distribution as particles in the charge precluded spot analyses without Ir or Pt interference. Thus, the experimental setup was modified and in subsequent experiments Pt and Ir were added as discrete pieces (~1 to 2 mm long x 0.2 mm diameter) of $Pt_{80}Ir_{20}$ wire (2 or 3 pieces per capsule, see Table 2.3 for total mass added).

Modified experiments using $Pt_{80}Ir_{20}$ wire (plus strips of $Au_{80}Pd_{20}$ foil if graphite capsules were used) were performed during the spring and summer of 2002 (runs 50 to 59). Detailed LA-ICP-MS analyses of these and some selected previous runs were performed at the Department of Earth Sciences, Memorial University of Newfoundland, with the collaboration of Dr. P. Sylvester and Mr. M. Tubrett. A VG PlasmaQuad2+S ICP-MS

34

coupled with an in-house-built Nd:YAG laser, frequency quadrupled to operate at a wavelength of 266 nm, was used. Operating conditions were: 50 $\mu$m beam diameter, 10 Hz laser pulse-rate, and 0.5 to 1 mJ/pulse energy. The laser system was coupled with a petrographic microscope with camera and monitor connection, allowing precise location of spot analysis. The advantages of analyzing the experiments at Memorial University rather than at the University of Saskatchewan were: the better optics of the optical microscope, which allowed for better location of the selected site for laser ablation; the availability of an Ir standard that has been calibrated by solution ICP-MS; the availability of software (LAMTRACE) for fast processing of large amounts of data; and most importantly, the expertise and experience of Dr. Sylvester and Mr. Tubrett in LA-ICP-MS analysis of HSE in geological materials.

The LA-ICP-MS apparatus at Memorial University is connected to an optical microscope with transmitted and reflected light capabilities, but optical microscopy does not allow for good discrimination of the phases present in the sample. Areas to be analyzed by LA-ICP-MS in each sample were pre-selected using BSE images. Multiple BSE images were taken at various scales to help locate the desired spots using features visible in both BSE and optical microscopy (edges, cracks, holes, arrangement of sulfide blebs). Micro-nuggets as small as 500 nm can be detected in BSE imaging due to the large contrast shown by sulfide and alloy phases relative to the basaltic glass. Pre-selected areas consisted of relatively large zones of glass (~70 $\mu$m diameter or larger) without other detectable phases. Carbon coating was removed using 0.25 $\mu$m diamond powder on a polishing wheel and minimal polishing was done to avoid significant modification of the features that were to be used to relocate the same areas using optical microscopy. This approach resulted in excellent accuracy, allowing avoidance of sulfides and micronuggets seen on BSE images. However, BSE images cannot detect phases that are not exposed on the sample surface and in many cases continuous ablation resulted in intersection of subsurface inclusions, causing spikes in the HSE intensities that exceeded the parameters of the mass spectrometer and caused software failure and loss of the acquired data. For this reason, samples with Ir powder as starting material were not analyzed for that particular element.

Two standards were used. A NIST SRM 612 glass was used for Pd, Pt, and Au. An in-house (Memorial University) standard (Ir-4-70) that has been calibrated by solution ICP-MS and tested by LA-ICP-MS for homogeneity was used for iridium.

The following isotopes were measured: $^{34}$S, $^{44}$Ca, $^{53}$Cr, $^{65}$Cu, $^{66}$Zn, $^{105}$Pd, $^{106}$Pd, $^{108}$Pd, $^{111}$Cd, $^{178}$Hf, $^{181}$Ta, $^{191}$Ir, $^{193}$Ir, $^{194}$Pt, $^{195}$Pt, and $^{197}$Au. To observe potential association of HSE with sulfide or spinel, $^{34}$S and $^{53}$Cr were measured. The copper and zinc isotopes were measured to monitor potential polyatomic interference on Pd (e.g., $^{65}$Cu$^{40}$Ar interference on $^{105}$Pd). Hafnium and tantalum were used in a similar fashion to monitor interferences on Pt, Ir, and Au. Cadmium was used to monitor for potential interference of $^{106}$Cd and $^{108}$Cd on $^{106}$Pd and $^{108}$Pd. Cadmium and copper were typically below detection limit in the samples, and hafnium concentration was less than 1 ppm. Zinc was the only potential cause of polyatomic interference in the samples with concentrations on the order of 30 ppm in the experimental glasses (similar to the Zn concentration in SRM 612). Because zinc concentrations in the samples and the standards are similar, the effect of zinc on the measured concentrations is negligible. However, the Cd concentration in glass SRM 612 used is nominally 28.32 ppm and interference on $^{106}$Pd and $^{108}$Pd from $^{106}$Cd and $^{108}$Cd is significant. For this reason, $^{105}$Pd was used to calculate Pd concentration in the samples. For the other HSE analyzed $^{193}$Ir, $^{195}$Pt, and $^{197}$Au were used.

The data were acquired using a procedure similar to the one described in Longerich et al. (1996). Data were collected in time-resolved mode with background collected for 30-40 s and sample signal collected for ~ 60 s. Analyses were performed in batches of up to 20 spot analyses, including two analyses of each standard at the beginning and at the end of each batch, providing a maximum of 12 unknown analyses per batch when two standards were used. The mass spectrometer used peak-hopping mode and dwell times of 8.33 ms to maximize counting statistics for the selected elements. The data were processed off-line using the spreadsheet programs CONVERT and LAMTRACE written by S. Jackson. The CONVERT program converts the acquired data to a simplified spreadsheet format and reduces noise by integrating and averaging all the sweeps in groups of three (a

36

"sweep" is single scan of all the selected masses). The LAMTRACE program allows for selection of the integration interval in the time resolved signal and calculates the concentration of the desired elements in the analyzed samples. The program uses the analyses of the standards at the beginning and at the end of each batch to correct for drift in sensitivity during the analyses of the samples in each batch.

Multiple spot analyses were performed on each sample. The HSE concentrations were estimated by integrating only the plateaus on time-resolved signals to minimize the effect of nano-scale nuggets. Analyzed samples were then cleaned, repolished with 0.25 $\mu$m diamond paste, carbon coated, and inspected using BSE imaging to document the location of the ablated sites relative to the capsule and other phases in the charge.

# 4. Experimental Results

Twenty-four successful experiments are presented in detail in this section. Table 4.1 lists the run products found in each experiment. The experiments can be split in three groups. The first group consists of nine sulfide-saturated experiments that were run in graphite capsules and used sulfide-bearing starting materials. These runs reproduced previous experiments that measured sulfur solubility in sulfide-saturated melts and provided a reference for subsequent work. The second group consists of nine sulfate-saturated experiments. The third group consists of five sulfide-saturated experiments produced by reduction of sulfate-bearing starting materials. An oxidized but sulfate-undersaturated run produced by oxidation of sulfides (run 58) is also included. Results from two additional experiments (runs 39 and 40) are also presented. These experiments clearly show disequilibrium, but they record and illustrate some of the processes that are associated with the changes in oxidation state and how it affects sulfur speciation and solubility.

## 4.1. Description and chemical composition of run products

### 4.1.1. Glasses

Silicate melts produced during the experiments quenched to homogeneous glasses. Settling of crystals was common, especially in runs from the first group of experiments, producing large areas of glass towards the top of the capsule (Figure 4.1 A). In all other cases quenched glasses and all other phases were evenly distributed (Figure 4.1 B). In the latter cases the melt fraction varies slightly among experiments and melt pockets are usually interconnected and relatively large (>50 $\mu$m diameter). The only exceptions to this are runs 30Fe and 30Ca, which quenched to an aggregate of crystals and produced only small pockets (<10 $\mu$m diameter) of glass.

38

Table 4.1. Summary of the run products obtained in the 24 experiments selected for detailed analyses.

| Run# | Run products | P (GPa) | T (°C) | t (hours) |
|---|---|---|---|---|
| | **Sulfide-saturated** | | | |
| 2 | Gl, sulfide, opx, cpx | 1.6 | 1355 | 24 |
| 3 | Gl, sulfide, opx, cpx | 1.6 | 1355 | 24 |
| 4 | Gl, sulfide, spl, opx, cpx | 1.6 | 1355 | 24 |
| 5 | Gl, sulfide, opx, cpx | 1.6 | 1355 | 24 |
| 7 | Gl, sulfide, spl, opx, cpx | 1.6 | 1355 | 48 |
| 10 | Gl, sulfide | 1.6 | 1355 | 1 |
| 11 | Gl, sulfide, opx | 1.6 | 1355 | 8 |
| 12 | Gl, sulfide, opx, cpx | 1.6 | 1355 | 4 |
| 59 | Gl, sulfide, ol, spl | 1.0 | 1300 | 6 |
| | **Sulfate-saturated** | | | |
| 26 | Gl, sulfate, ol, spl, opx, cpx | 1.1 | 1315 | 4 |
| 30Ca | Gl, sulfate, spl, opx, cpx | 1.1 | 1315 | 6 |
| 30Fe | Gl, sulfate, ol, spl, opx, cpx | 1.2 | 1315 | 6 |
| 34C | Gl, sulfate, ol, spl, opx, cpx | 1.2 | 1315 | 4 |
| 35 | Gl, sulfate, ol, spl, opx | 1.2 | 1315 | 2 |
| 50 | Gl, sulfate, ol, spl | 1.0 | 1325 | 4 |
| 52 | Gl, sulfate, ol, spl | 1.0 | 1300 | 4 |
| 56 | Gl, sulfate, ol, spl | 1.0 | 1300 | 4 |
| 57 | Gl, sulfate, ol, spl | 1.0 | 1300 | 4 |
| | **Sulfate-reduction** | | | |
| 27C | Gl, sulfide, ol, spl, opx, cpx | 1.1 | 1315 | 10 |
| 35C | Gl, sulfide, ol, spl, opx, cpx | 1.2 | 1315 | 2 |
| 53 | Gl, sulfide, ol, spl | 1.0 | 1300 | 4 |
| 54 | Gl, sulfide, ol, spl | 1.0 | 1300 | 4 |
| 55 | Gl, sulfide, ol, spl | 1.0 | 1300 | 4 |
| | **Oxidized-undersaturated** | | | |
| 58 | Gl, ol, spl | 1.0 | 1300 | 6 |

Gl = glass     Cpx = clinopyroxene     Opx = orthopyroxene
Ol = olivine     Spl = spinel

39
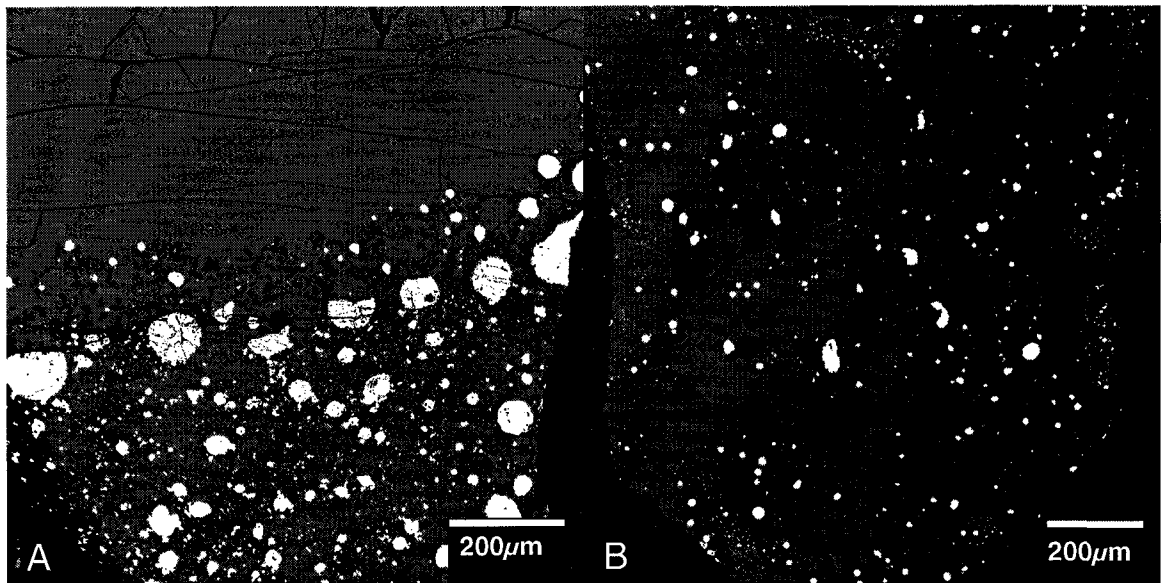
Figure 4.1. BSE images of sulfide-bearing runs in graphite capsules. Black: capsule walls, cracks and holes; light grey: quenched glass; medium to dark grey: crystalline phases; bright white: sulfide blebs. The top direction of capsules coincides with top of the page.

A: run #4; obtained from FeS and glass B302 as starting material. Note crystal settling and wetting of sulfides against capsule walls. The darker crystals defining a band towards the center of the capsule are orthopyroxene. Clinopyroxene forms a large proportion of the cumulate crystals but is hard to distinguish in this picture because of its similarity in grayscale to the glass.

B: run 27C; sulfides in this run were produced by reduction of sulfate starting material. Note the large crystals of olivine (mid grey) produced by seeding the experiments with olivine. Smaller crystals (mid grey) concentrated towards the margins are orthopyroxene.

40

The major-element chemical compositions of the glasses are summarized in Table 4.2. Because the experiments are potassium-free, a $Na_2O$ against $SiO_2$ diagram (Figure 4.2) was used to classify the quenched glasses according to the IUGS scheme (Le Maitre, 2002). Most of the experiments produced glasses that are basaltic in composition, except for the glasses obtained in runs 30Fe, 50 and 52 which have $SiO_2 < 45$ wt.% and are therefore picrobasaltic. Figure 4.2 also illustrates the first geochemical difference between reduced assemblages (sulfide-bearing) and oxidized assemblages (sulfate-bearing, with the exception of run 58). Glasses from oxidized experiments are slightly, but consistently, more mafic and have $SiO_2 < \sim 47$ wt.% whereas reduced experiments have $SiO_2 > \sim 47$ wt.%.

The contrast in sulfur solubility between sulfide-saturated and sulfate-saturated basaltic melts is illustrated in Figure 4.3. Sulfur concentrations in sulfate-saturated glasses range from 1.0 to 1.8 wt.% whereas sulfur concentration is sulfide saturated melts ranges from 0.11 to 0.19 wt.%, a difference in sulfur solubility of one order of magnitude.

Concentrations of the HSE as measured by LA-ICP-MS are presented in section 4.5.1.

Table 4.2. Composition of quenched glasses (in wt.%).

| Run # | SiO$_2$ | TiO$_2$ | Al$_2$O$_3$ | Cr$_2$O$_3$ | FeO | MgO | CaO | Na$_2$O | S | Total[b] |
|---|---|---|---|---|---|---|---|---|---|---|
| 2 | 47.4 (2)[a] | 0.73 (5) | 18.1 (1) | 0.03 (1) | 8.6 (1) | 11.2 (1) | 11.0 (1) | 2.4 (1) | 0.14 (2) | 99.8 |
| 3 | 47.9 (3) | 0.68 (5) | 18.2 (1) | 0.05 (2) | 7.0 (1) | 12.1 (1) | 11.4 (1) | 2.3 (1) | 0.13 (2) | 100.0 |
| 4 | 47.7 (2) | 0.72 (3) | 18.2 (1) | 0.04 (2) | 8.2 (1) | 11.4 (2) | 11.1 (1) | 2.4 (1) | 0.14 (2) | 100.1 |
| 5 | 47.9 (3) | 0.74 (4) | 18.3 (1) | 0.05 (1) | 7.9 (1) | 11.5 (1) | 11.4 (1) | 2.4 (1) | 0.14 (1) | 100.5 |
| 7 | 47.5 (4) | 0.72 (4) | 18.0 (1) | 0.04 (2) | 8.3 (1) | 11.5 (1) | 10.9 (1) | 2.4 (1) | 0.15 (1) | 99.7 |
| 10 | 47.1 (3) | 0.68 (2) | 17.8 (1) | 0.08 (3) | 8.2 (1) | 12.6 (1) | 10.7 (1) | 2.1 (1) | 0.18 (1) | 99.7 |
| 11 | 47.6 (3) | 0.69 (4) | 17.9 (1) | 0.06 (2) | 7.8 (1) | 12.6 (1) | 11.0 (1) | 2.2 (1) | 0.16 (2) | 100.3 |
| 12 | 47.7 (3) | 0.72 (4) | 18.5 (2) | 0.02 (1) | 8.2 (1) | 10.9 (3) | 11.3 (2) | 2.5 (1) | 0.14 (1) | 100.2 |
| 27C | 49.0 (7) | 0.67 (3) | 18.3 (3) | 0.06 (2) | 4.9 (1) | 11.9 (7) | 12.1 (2) | 2.6 (1) | 0.11 (1) | 99.8 |
| 35C | 48.0 (7) | 0.61 (3) | 18.4 (5) | 0.09 (4) | 5.1 (6) | 12.6 (7) | 11.5 (1) | 1.78 (9) | 0.15 (8) | 98.5 |
| 53 | 47.1 (6) | 0.70 (4) | 17.7 (2) | 0.07 (2) | 8.7 (2) | 11.9 (4) | 10.8 (2) | 2.21 (9) | 0.16 (1) | 99.6 |
| 54 | 50.1 (2) | 0.71 (2) | 17.4 (1) | 0.11 (1) | 5.2 (3) | 11.6 (1) | 11.9 (2) | 2.6 (2) | 0.11 (2) | 99.9 |
| 55 | 50.1 (2) | 0.73 (4) | 18.0 (2) | 0.12 (1) | 5.3 (2) | 11.1 (2) | 11.6 (1) | 2.52 (7) | 0.11 (2) | 99.7 |
| 59 | 46.2 (4) | 0.67 (2) | 17.7 (4) | 0.06 (1) | 9.1 (2) | 10.7 (3) | 11.2 (3) | 2.39 (4) | 0.19 (2) | 98.5 |
| 26 | 45.6 (3) | 0.61 (4) | 15.5 (1) | 0.02 (1) | 8.2 (1) | 12.8 (2) | 12.6 (2) | 1.76 (7) | 1.28 (9) | 100.3 |
| 30Ca | 46.3 (5) | 0.58 (5) | 17.0 (1) | 0.02 (1) | 7.5 (3) | 11.9 (1) | 10.4 (5) | 3.1 (3) | 1.34 (7) | 100.2 |
| 30Fe | 45.2 (3) | 0.60 (4) | 16.5 (2) | 0.01 (1) | 8.1 (2) | 12.0 (2) | 10.6 (3) | 3.0 (6) | 1.52 (3) | 99.8 |
| 34C | 46.3 (7) | 0.59 (3) | 16.2 (4) | 0.04 (2) | 7.9 (3) | 12.9 (2) | 11.3 (4) | 2.1 (4) | 1.0 (2) | 99.8 |
| 35 | 46.5 (3) | 0.53 (3) | 15.3 (2) | 0.07 (1) | 7.5 (2) | 14.8 (2) | 9.6 (2) | 1.84 (8) | 1.6 (2) | 100.1 |
| 50 | 44.1 (5) | 0.59 (3) | 15.5 (2) | 0.03 (1) | 8.0 (3) | 13.2 (3) | 12.5 (1) | 1.81 (8) | 1.62 (4) | 99.8 |
| 52 | 43.5 (3) | 0.58 (1) | 14.7 (2) | 0.02 (1) | 11.4 (2) | 13.8 (3) | 9.2 (1) | 1.91 (5) | 1.80 (3) | 99.6 |
| 56 | 46.2 (3) | 0.57 (3) | 15.2 (1) | 0.08 (1) | 7.9 (1) | 15.6 (1) | 9.7 (1) | 2.05 (6) | 1.15 (8) | 100.2 |
| 57 | 45.8 (2) | 0.56 (2) | 15.0 (1) | 0.09 (2) | 7.9 (1) | 15.9 (2) | 9.6 (1) | 2.00 (6) | 1.26 (6) | 100.0 |
| 58 | 45.0 (2) | 0.61 (3) | 15.8 (2) | 0.03 (1) | 10.8 (1) | 13.5 (1) | 10.1 (1) | 2.17 (9) | 0.37 (6) | 98.9 |

Notes: [a]numbers in parenthesis are standard deviations (1$\sigma$) on the last significant figure
[b]totals are calculated with S as SO$_3$

42
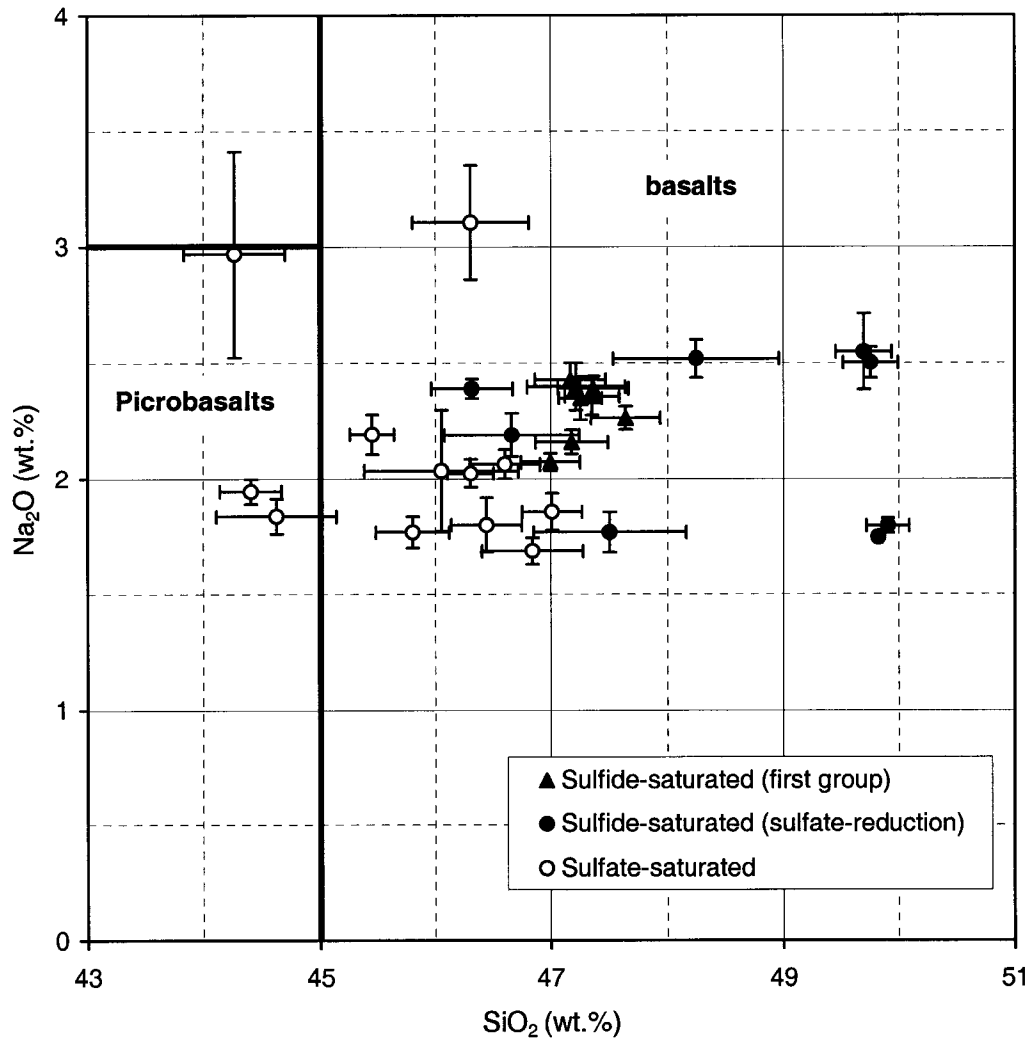
Figure 4.2. Harker diagram of Na₂O against SiO₂ for the quenched glasses in this study. Because the experiments are potassium-free this diagram is equivalent to the total alkali-silica diagram of the IUGS classification of volcanic rocks. The boundary between the picrobasalt and basalt fields at $SiO_2 = 45$ is shown as a thicker line for clarity. Most glasses are basaltic. Three runs (30Fe, 50, and 52) have $SiO_2 < 45\%$ and are therefore of picrobasaltic composition. Note that quenched glasses from sulfate-saturated experiments contain less silica than glasses coexisting with sulfides.

43
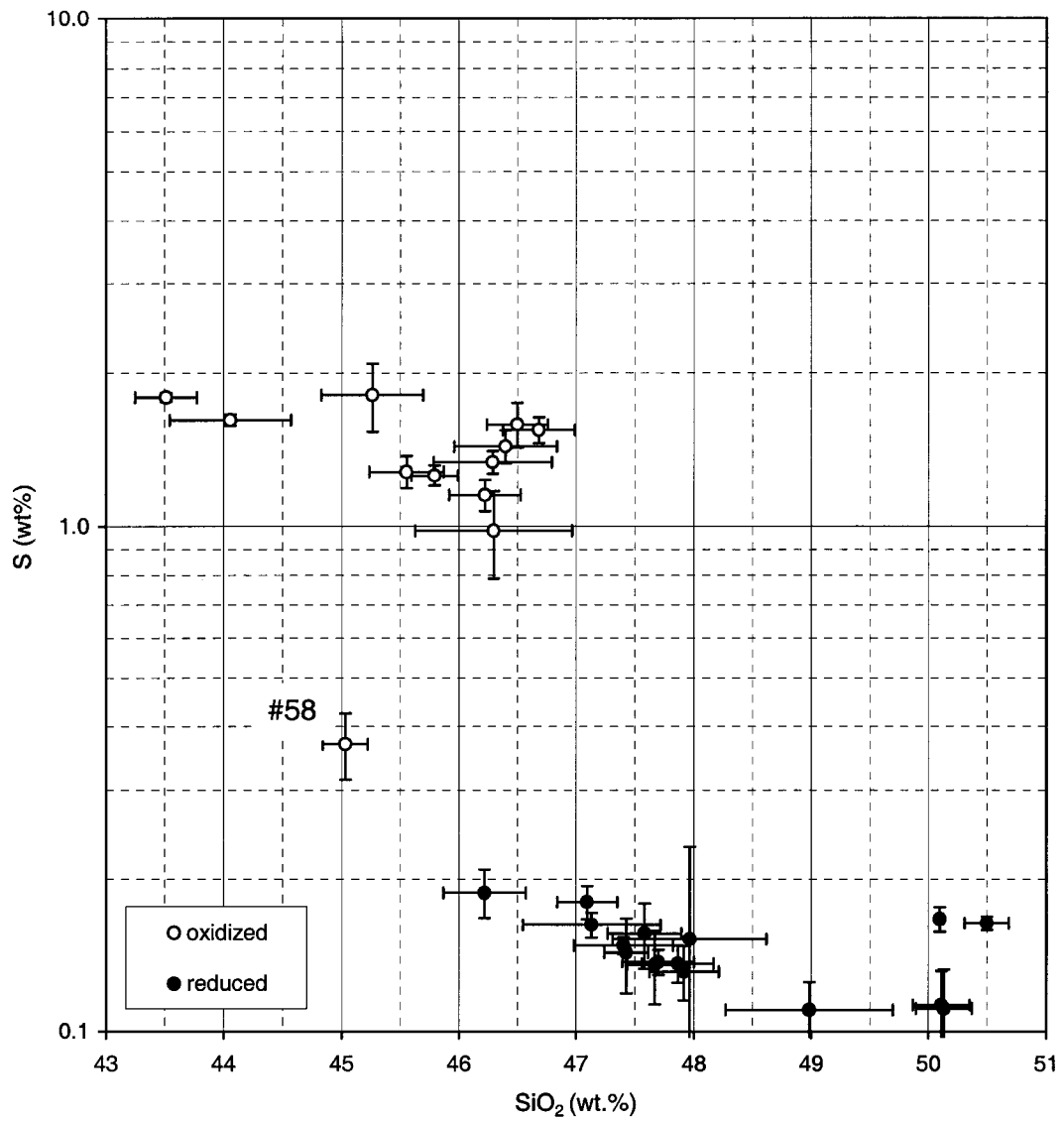
Figure 4.3. Sulfur concentration against $SiO_2$ for the quenched glasses in this study. All samples labeled "reduced" are sulfide saturated. With the exception of one sample (58), samples labeled "oxidized" are sulfate saturated. Sulfate-bearing glasses can dissolve roughly ten times more sulfur than sulfide-bearing glasses.

44

## 4.1.2. Sulfides

Fourteen experiments contained sulfides as a run product. Nine experiments produced sulfides from sulfide-bearing starting material (runs 2 to 12, and run 59). Five experiments produced sulfides from sulfate-bearing starting material, either by the use of graphite capsules (runs 27C, 35C, and 53) or by addition of graphite powder to the starting material in experiments using AuPd capsules (runs 54 and 55).

The spherical shapes of the sulfides, inferred from their rounded sections in the polished samples (Figure 4.1), are consistent with the sulfides being present as immiscible liquids at the experimental conditions. Because copper or nickel are not present in the experiments, the sulfides produced upon quenching consisted of pyrrhotite with an average composition of 36.9 ± 0.9 wt.% S and 60.2 ± 1.2 wt.% Fe (Table 4.3). Oxygen was not analyzed in the sulfides, the difference to 100 % in the totals (~ 3 wt. %) is assumed to be the approximate oxygen content in the sulfides

Table 4.3. Compositions of sulfide run products (in wt.%)

| run # | S | Fe | Total | n |
|---|---|---|---|---|
| 2 | 36.3 | 61.2 | 97.5 | 8 |
| 3 | 37.3 | 59.8 | 97.1 | 4 |
| 4 | 36.8 | 61.0 | 97.8 | 8 |
| 5 | 37.1 | 61.1 | 98.2 | 4 |
| 7 | 36.0 | 60.8 | 96.8 | 8 |
| 10 | 37.2 | 60.9 | 98.1 | 5 |
| 11 | 37.3 | 60.5 | 97.8 | 5 |
| 12 | 36.5 | 61.0 | 97.4 | 6 |
| 53 | 36.5 | 61.0 | 97.6 | 10 |
| 54 | 39.2 | 57.7 | 96.9 | 7 |
| 55 | 35.6 | 57.7 | 93.3 | 5 |
| 59 | 37.2 | 59.9 | 97.2 | 11 |
| | | | | |
| Mean | 36.9 | 60.2 | 97.1 | |
| 1σ | 0.9 | 1.2 | 1.2 | |

45

Some experiments in graphite-lined Pt capsules (e.g., run 12) produced sulfides containing platinum (Figure 4.4, A and B). These sulfides quenched to produce small (<1 $\mu$m), discrete Pt-rich domains that are consistent with platinum being dissolved in the sulfide melt at run conditions and segregating upon quenching. The occurrence of platinum in the sulfides indicates that in some cases the graphite capsules were not perfect barriers between the charge and the platinum capsule. In extreme cases (e.g., cracked graphite capsule) Pt-Fe exchange between the Pt-capsule and the charge resulted in significant loss of Fe (total FeO in the quenched glasses < 5 wt.%). Those experiments were discarded.

Experiments in which Pt and Ir were added as powder (runs 27C and 35C) produced sulfide blebs that completely enclosed the Pt and Ir particles (Figure 4.4 C and D). Analyses of sulfides in these runs (Table 4.4) show large compositional variations in the sulfides, which include variable amounts of Pt and Ir in sulfides that otherwise appeared homogeneous in BSE imaging. Analyses of the enclosed phases (which had a marked contrast in BSE imaging relative to the sulfide hosts) show that these are metallic alloys with little or negligible sulfur content, and different compositions from the added metal phases (pure Ir or pure Pt).

Table 4.4. Example of variability of Pt and Ir concentration in sulfides and enclosed metallic inclusions from runs 27C and 35C (in wt.%).

| S | Fe | Pt | Ir | Total | run#, Comment |
|------|------|------|------|-------|----------------------------------|
| 5.3 | 11.0 | 30.7 | 55.1 | 102.1 | 27C, rhombohedral inclusion[a] |
| 35.9 | 49.6 | 7.7 | 12.4 | 105.6 | 27C, sulfide |
| 36.9 | 52.4 | 5.0 | 8.0 | 102.3 | 27C, sulfide |
| 0.1 | 10.7 | 86.9 | 0.1 | 102.1 | 35, inclusion |
| 35.9 | 46.4 | 9.5 | 14.4 | 106.2 | 35, sulfide 2 |
| 36.5 | 49.7 | 7.5 | 10.3 | 105.0 | 35, sulfide 3 |

[a] this analysis corresponds to the inclusion shown in picture 4.4 D.

46
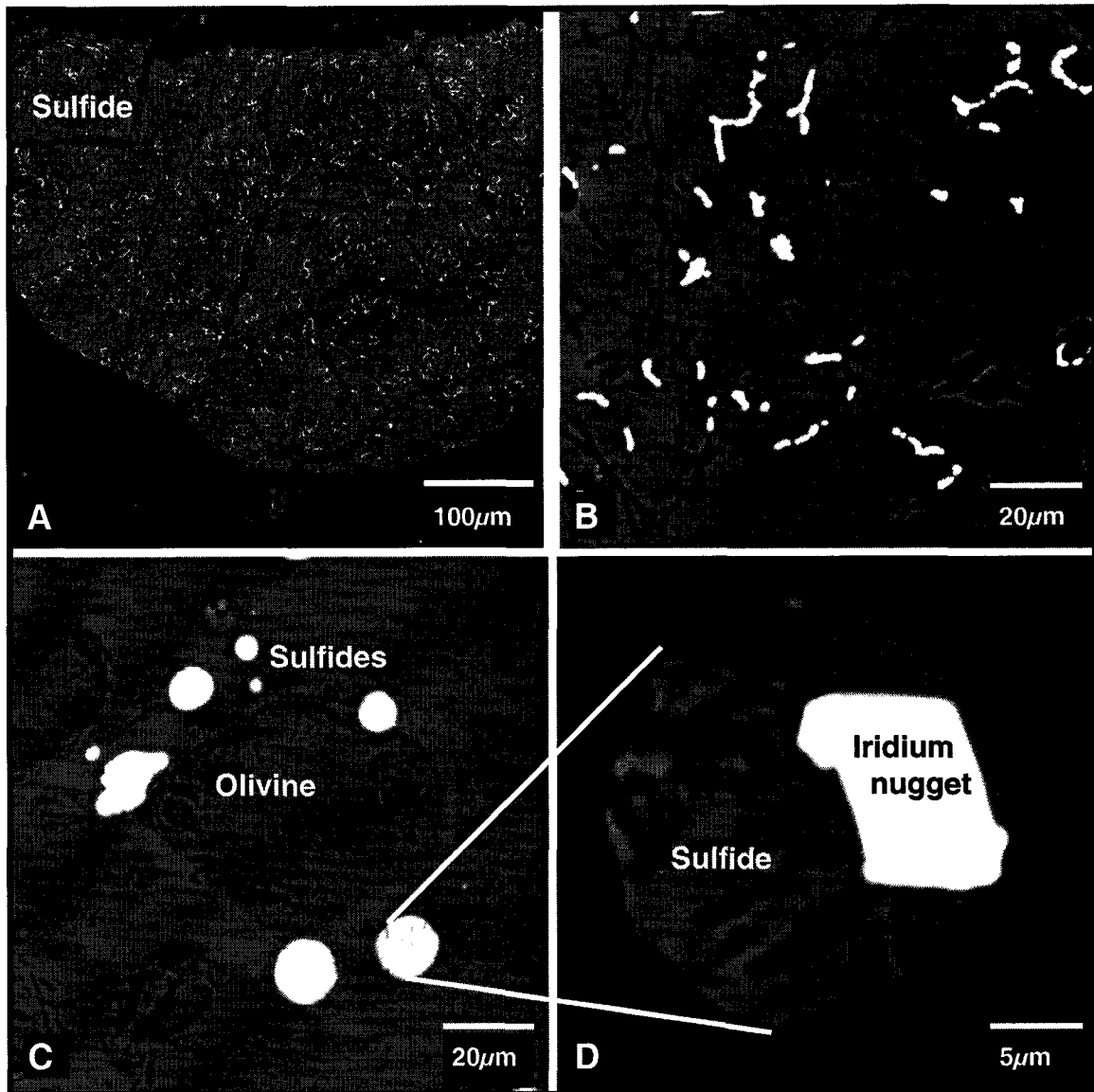
Figure 4.4. BSE images of sulfides in sulfide-bearing runs.

**A:** large sulfide bleb from run 12.

**B:** detail of picture A, note exsolution textures in the sulfides. The bright areas are Pt-rich presumably leached from the Pt capsule through the graphite walls.

**C:** sulfides and olivine from run 27C in which sulfides are produced by reduction of sulfate. Iridium was added as Ir powder in this run.

**D:** Detail of sulfide droplet in run 27C showing how sulfide surrounds and encloses the iridium nugget.

### 4.1.3. Sulfates

Nine experiments contained sulfates as run products. Examples of the sulfates are shown in Figures 4.5 and 4.6. Their shapes are similar to those of the sulfides, as rounded blebs that are consistent with the sulfates being present as immiscible liquids. Therefore, anhydrite or other sulfate crystalline phases are not stable at the experimental conditions. Previous experiments in sulfate-saturated systems (Carroll and Rutherford, 1985, 1987; Luhr, 1990), were conducted at lower temperatures (up to 1025 °C) and thus, contained anhydrite as the sulfate phase. Because the fusion temperature for anhydrite at 1 atm is 1450 °C, the presence of a sulfate immiscible liquid at the run conditions (1300 °C) likely indicates incorporation of other cations into the sulfate with the resulting decrease of its melting point.

Polishing of sulfate-bearing samples using water to remove abraded material between polishing steps resulted in intense dissolution or complete elimination of sulfates. Sulfate blebs were preserved if samples were polished using only oil and cleaned with methanol, but even in those cases irregular, uneven, and plucked surfaces were obtained because of the low hardness of the sulfates relative to the surrounding glass. For this reason, quantitative analysis using WDS were not attempted. Energy dispersive analyses (EDS) showed that the sulfate blebs were Ca- and S-rich with very small amounts of Na and Mg, even in experiments in which sulfur was added as $FeSO_4$.

48
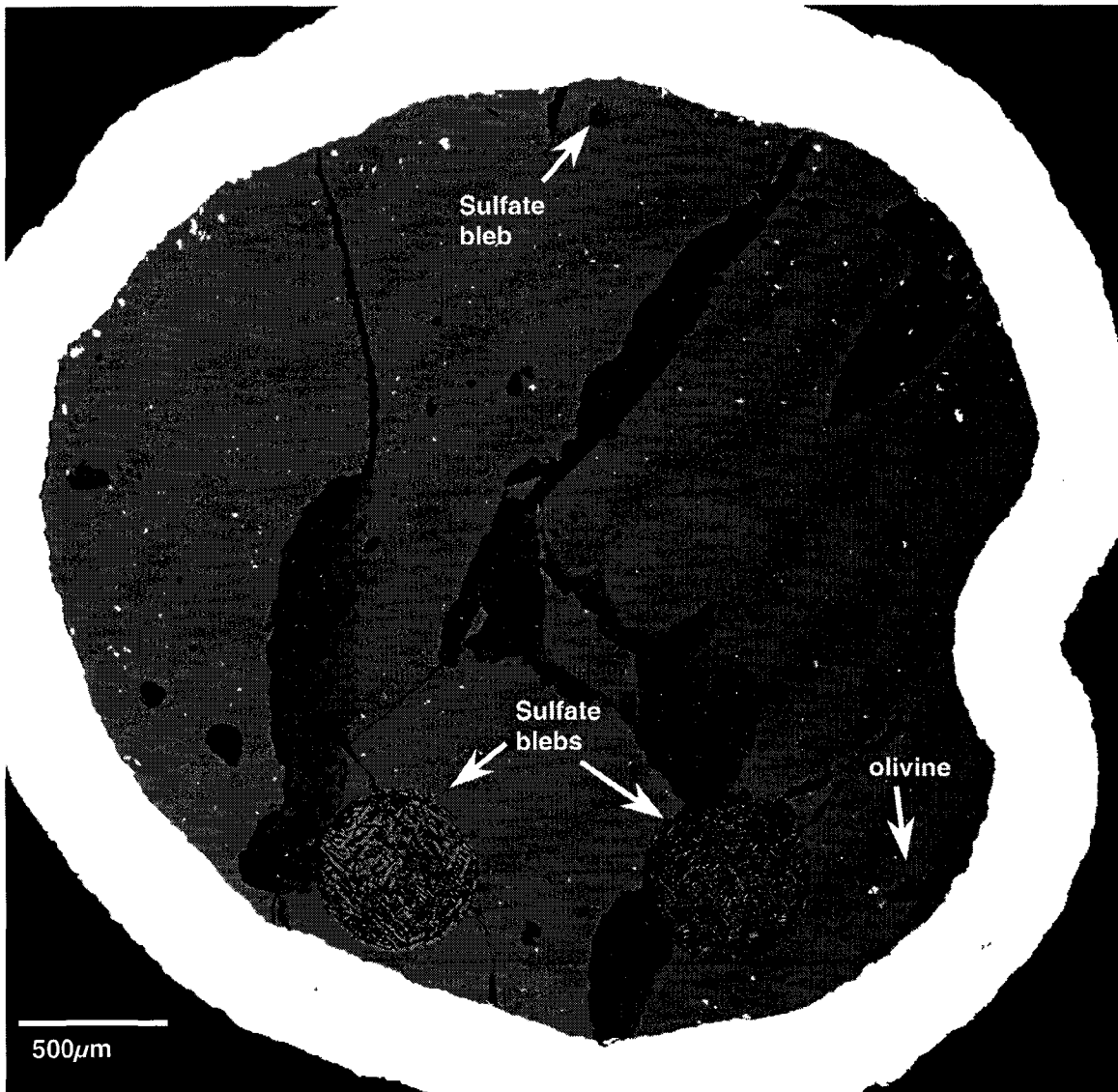
Figure 4.5. BSE image of a cross-sectional view of a sulfate-bearing run (run 26) in AuPd capsule. The illustrated cross-section is near the top of the capsule (capsule is 3mm OD). Sections of two large sulfate blebs can be seen towards the bottom of the picture. A relatively small section of a sulfate bleb is noticeable towards the top of the picture close to the edge of the capsule. The light grey area that makes up most of the content of the section is quenched glass. The dark grey areas are olivine crystals, and the small white areas are small nuggets of Ir added as powder. Spinel crystals are present and dispersed in the glass, but are too small to be seen in this picture.

49
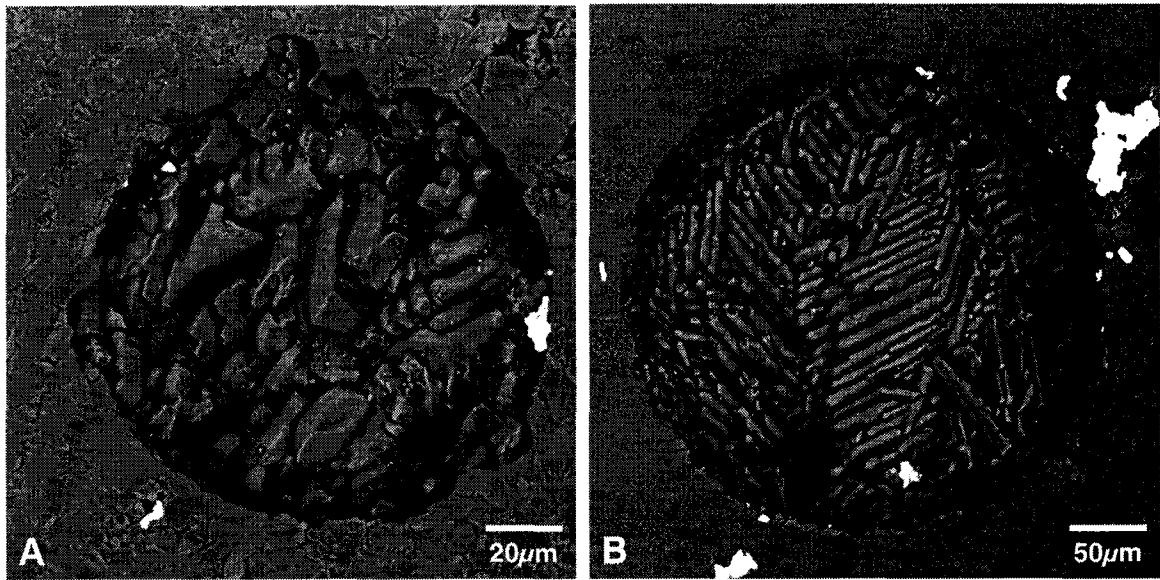
Figure 4.6. BSE detail of sulfate blebs obtained in sulfate-bearing runs.
A: run 30Fe, obtained from $FeSO_4$ and low-Fe-glass starting material.
B: run 30Ca, obtained from $CaSO_4$ and low-Ca-glass starting material.
In both cases, the spherical shape of the blebs indicates that at the pressure and temperature of the experiments the sulfate was present as an immiscible liquid, analogous to FeS liquids in sulfide-saturated experiments. EDS analyses of these sulfates showed that in both cases the sulfate blebs are almost entirely $CaSO_4$, which is further indication that these two experiments, performed with different sulfate starting materials, attained equilibrium. The bright white areas are remnants of the Ir powder added to the runs. In contrast to sulfide bearing runs (Figure 4.4), Ir nuggets are present both as discrete, isolated grains or aggregates (e.g., upper right corner figure B), and rarely as inclusions in the sulfate blebs (as in A).

50

### 4.1.4. Olivine

Olivine was absent as a run product in the experiments that used only glass B302 as silicate starting material. Where present, olivine typically formed relatively large (up to 100 $\mu$m length), homogeneous crystals, that are euhedral to subhedral (Figures 4.1 B, 4.4 C, and 4.7). Olivine compositions are summarized in Table 4.5. As explained in section 2.1.4, olivine was added to subsequent experiments to stabilize this phase. To verify that the olivines equilibrated with the melt, the partitioning of iron and magnesium between the olivine and the quenched glasses ($K_D$, Roeder and Emslie, 1970) was calculated. Ferric iron in the glasses were estimated using the method of Kilinc et al. (1983) and the oxidation state estimated from olivine and spinel compositions (discussed in section 4.3). The average for reduced experiments yields $K_D = 0.31 \pm 0.3$ if all iron is assumed to be present as $Fe^{2+}$, and $K_D = 0.32 \pm 0.4$ if $Fe^{3+}/\Sigma Fe$ is calculated. The results are consistent with the expected $K_D = 0.30 \pm 0.03$ in olivines in equilibrium with a silicate liquid (Roeder and Emslie, 1970). In oxidized experiments, $K_D$ estimates assuming all iron as $Fe^{2+}$ was significantly lower ($K_D = 0.212 \pm 0.004$), which can be explained by the significant amounts of $Fe^{3+}$ in the glasses in these experiments. Estimated glass $Fe^{3+}$ contents using the method of Kilinc et al. (1983) are in the range $0.26 \leq Fe^{3+}/\Sigma Fe \leq 0.49$, the higher value corresponding with run26, which equilibrated at the higher oxidation state (FMQ+3.82). Recalculated values of $K_D$, corrected for $Fe^{3+}$ (Table 4.6), are consistent with olivine-melt equilibration ($K_D = 0.31 \pm 0.01$).
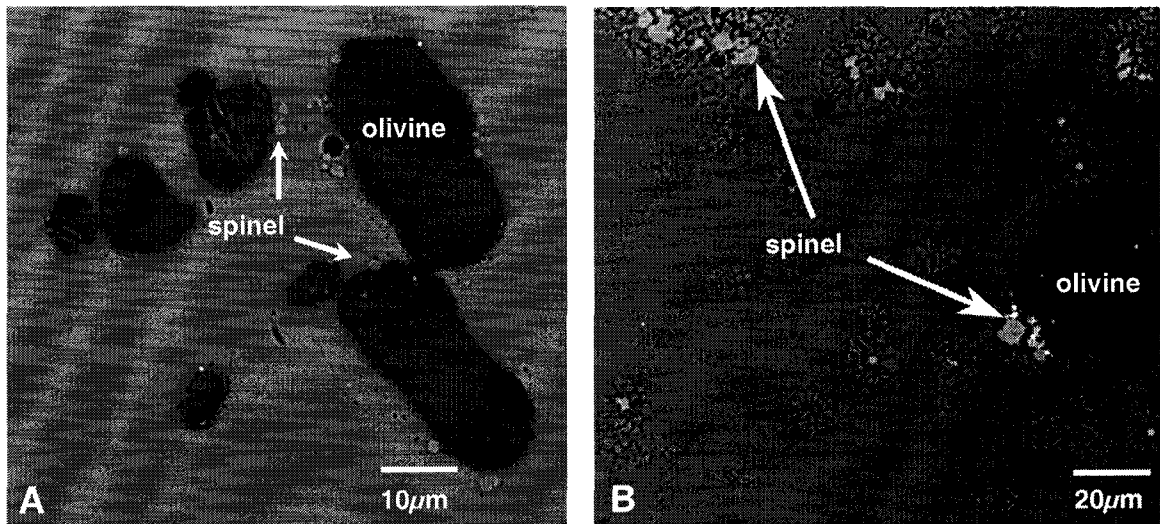
Figure 4.7. BSE images of typical olivine and spinel used for oxybarometry. Light grey background is quenched glass, dark grey areas are olivine.

**A:** run 50; spinels are the light grey, small crystals with equant sections, clustered around and in between olivine crystals; some small crystals of spinel can be seen included in the small olivine crystal at the center of the picture.

**B:** run 52; spinels are the whitish equant crystals. Only one olivine crystal is shown, which is very similar to those seen in figure **A** and also contains very small inclusions of spinel. The small feathery crystals around spinel are too small to be analyzed by WDS, but EDS analysis show that they are also spinel. The vermiform rims are similar to those documented in Roeder et al. (2001).

52

Table 4.5. Compositions of olivines in wt.%, and oxidation states calculated with the olivine-orthopyroxene-spinel oxybarometer of Ballhaus et al. (1991).

| Run# | Reduced experiments | | | | | | Oxidized experiments | | | | | | | | |
|---|---|---|---|---|---|---|---|---|---|---|---|---|---|---|---|
| | 27C | 35C | 53 | 54 | 55 | 59 | 26 | 30Fe | 34C | 35 | 50 | 52 | 56 | 57 | 58 |
| T(°C) | 1315 | 1315 | 1325 | 1325 | 1325 | 1325 | 1315 | 1315 | 1315 | 1315 | 1325 | 1325 | 1325 | 1325 | 1325 |
| P(GPa) | 1.2 | 1.2 | 1.0 | 1.0 | 1.0 | 1.0 | 1.2 | 1.2 | 1.2 | 1.2 | 1.0 | 1.0 | 1.0 | 1.0 | 1.0 |
| $SiO_2$ | 40.7 | 41.2 | 39.7 | 40.4 | 40.4 | 39.7 | 41.0 | 41.1 | 40.7 | 41.6 | 40.2 | 39.9 | 40.8 | 40.5 | 39.9 |
| $Al_2O_3$ | na[a] | na | 0.00 | 0.03 | 0.02 | 0.07 | 0.06 | 0.14 | 0.12 | 0.12 | na | 0.00 | 0.10 | 0.13 | 0.04 |
| $Cr_2O_3$ | na | 0.08 | na | na | na | na | na | 0.04 | 0.03 | 0.04 | na | na | na | na | na |
| FeO | 7.1 | 7.0 | 9.9 | 7.4 | 7.6 | 10.8 | 5.1 | 6.4 | 7.4 | 5.9 | 6.7 | 9.0 | 6.0 | 5.9 | 9.2 |
| MgO | 50.7 | 51.5 | 49.5 | 51.1 | 51.1 | 49.4 | 53.1 | 52.0 | 51.5 | 52.3 | 51.7 | 50.0 | 52.7 | 52.2 | 50.6 |
| CaO | 0.2 | 0.2 | 0.1 | 0.1 | 0.2 | 0.2 | 0.2 | 0.1 | 0.2 | 0.2 | 0.2 | 0.1 | 0.2 | 0.2 | 0.1 |
| Total | 98.8 | 100.0 | 99.2 | 99.0 | 99.2 | 100.2 | 99.4 | 99.9 | 100.0 | 100.2 | 98.9 | 99.1 | 99.7 | 98.9 | 99.8 |
| **Cations** | | | | | | | | | | | | | | | |
| Si | 1.00 | 1.00 | 0.98 | 0.99 | 0.99 | 0.98 | 0.99 | 0.99 | 0.99 | 1.00 | 0.98 | 0.98 | 0.99 | 0.99 | 0.98 |
| Al | 0.00 | 0.00 | 0.00 | 0.00 | 0.00 | 0.00 | 0.00 | 0.00 | 0.00 | 0.00 | 0.00 | 0.00 | 0.00 | 0.00 | 0.00 |
| Cr | 0.00 | 0.00 | 0.00 | 0.00 | 0.00 | 0.00 | 0.00 | 0.00 | 0.00 | 0.00 | 0.00 | 0.00 | 0.00 | 0.00 | 0.00 |
| $Fe^{2+}$ | 0.15 | 0.14 | 0.20 | 0.15 | 0.16 | 0.22 | 0.10 | 0.13 | 0.15 | 0.12 | 0.14 | 0.19 | 0.12 | 0.12 | 0.19 |
| Mg | 1.85 | 1.86 | 1.83 | 1.87 | 1.86 | 1.81 | 1.91 | 1.87 | 1.86 | 1.87 | 1.89 | 1.84 | 1.90 | 1.90 | 1.85 |
| Ca | 0.01 | 0.01 | 0.00 | 0.00 | 0.00 | 0.00 | 0.00 | 0.00 | 0.01 | 0.00 | 0.01 | 0.00 | 0.00 | 0.01 | 0.00 |
| Total | 3.00 | 3.00 | 3.02 | 3.01 | 3.01 | 3.02 | 3.01 | 3.00 | 3.01 | 3.00 | 3.02 | 3.02 | 3.01 | 3.01 | 3.02 |
| Mg# | 0.93 | 0.93 | 0.90 | 0.93 | 0.92 | 0.89 | 0.95 | 0.94 | 0.93 | 0.94 | 0.93 | 0.91 | 0.94 | 0.94 | 0.91 |
| $\Delta FMQ$[b] | -1.12 | -2.89 | -2.87 | -1.50 | -1.54 | -3.43 | 3.82 | 2.59 | 1.85 | 2.41 | 2.22 | 2.70 | 2.46 | 2.50 | 2.22 |

Notes: [a]na: not analyzed on this sample
[b]calculated with these analyses and spinel analyses presented in Table 4.3.

Table 4.6. Olivine-glass (Fe/Mg) $K_D$ and glass $Fe^{3+}/\Sigma Fe$ in oxidized experiments.

| Run# | $K_D$ uncorrected | $K_D$ corrected[a] | $(Fe^{3+}/\Sigma Fe)_{glass}$[b] | $\Delta FMQ$[c] |
|------|------|------|------|------|
| 26 | 0.15 | 0.28 | 0.49 | 3.82 |
| 30Fe | 0.18 | 0.28 | 0.35 | 2.59 |
| 34C | 0.23 | 0.32 | 0.26 | 1.85 |
| 35 | 0.23 | 0.31 | 0.28 | 2.41 |
| 50 | 0.22 | 0.30 | 0.27 | 2.22 |
| 52 | 0.22 | 0.34 | 0.34 | 2.70 |
| 56 | 0.22 | 0.32 | 0.30 | 2.46 |
| 57 | 0.23 | 0.33 | 0.31 | 2.50 |
| 58 | 0.23 | 0.32 | 0.29 | 2.22 |
| | | | | |
| Ave | 0.212 | 0.31 | | |
| 1s | 0.004 | 0.01 | | |

Notes:  [a] corrected for ferric iron content in the glass
        [b] ferric iron in the glass. Calculated using Kilinc et al. (1983) and data from Table 4.5.
        [c] taken from Table 4.5

54

## 4.1.5. Spinel

Spinel was present in most runs, but often occurred as very small crystals, rarely larger than 5 $\mu$m. They occurred as equant crystals with trapezoidal sections that were included in olivine or isolated within quenched glasses. In a few experiments (runs, 52 and 58), "vermiform" (wormy) rims of spinel surrounded equant crystals of spinel. Examples of both types of spinel crystals are shown in Figure 4.7. Roeder et al. (2001) documented similar textures in natural and experimental glasses and concluded that the vermiform textures are growth textures, produced by diffusion-controlled growth, and not reaction textures. However, the experiment described in Roeder et al. (2001) was held at 1225 °C for 67 h and then slowly cooled to 1147 °C over 8 h, in contrast to the runs described here which were held at constant pressure and temperature and then quenched. The only significant difference to other runs is that both runs 52 and 58 contained more than 11% FeO in the bulk composition, which is reflected in the Fe content in the spinels. Run 52 was prepared using $FeSO_4$ as a complementary source of FeO in the run whereas in run 58 iron was added both as FeS and $Fe_2O_3$. Therefore a possible explanation is that the vermiform rims are related to the FeO in the melt. However, comparisons of the composition of the run products in run 52 with other similar experiments in this study (e.g., run 50 in which sulfate was added as $CaSO_4$) indicate that the equilibria studied in this work are not affected.

The chemical compositions of the spinels are shown in Table 4.7. In some experiments, the small size of the spinel crystals (in some cases smaller than 1 $\mu$m) made the determination of their composition by EPMA difficult or impossible; therefore, in the latter cases, spinel compositions are not documented. Ferric iron contents were calculated assuming stoichiometry following the method outlined by Droop (1987).

Table 4.7. Compositions of spinels in wt.%; $Fe^{3+}$ estimated from stoichiometry

| | Run# | Reduced experiments | | | | | | Oxidized experiments | | | | | | | | |
|---|---|---|---|---|---|---|---|---|---|---|---|---|---|---|---|---|
| | | 27C | 35C | 53 | 54 | 55 | 59 | 26 | 30Fe | 34C | 35 | 50 | 52 | 56 | 57 | 58 |
| Wt.% | SiO$_2$ | 0.5 | 0.7 | 0.3 | 0.8 | 0.5 | 0.3 | 0.5 | 0.2 | 0.7 | 0.4 | 0.5 | 0.4 | 0.4 | 0.4 | 0.4 |
| | TiO$_2$ | 0.1 | 0.1 | 0.2 | 0.2 | 0.1 | 0.1 | 0.2 | 0.1 | 0.1 | 0.1 | 0.2 | 0.3 | 0.1 | 0.1 | 0.2 |
| | Al$_2$O$_3$ | 59.5 | 53.7 | 57.1 | 43.7 | 44.5 | 54.8 | 48.8 | 51.5 | 55.7 | 45.0 | 52.9 | 47.0 | 45.4 | 44.7 | 48.1 |
| | Cr$_2$O$_3$ | 9.3 | 15.3 | 11.8 | 25.7 | 25.4 | 13.4 | 3.3 | 8.5 | 5.9 | 16.2 | 8.0 | 6.2 | 15.2 | 15.7 | 8.7 |
| | FeO | 6.7 | 6.7 | 9.5 | 7.6 | 6.5 | 10.6 | 23.4 | 17.7 | 14.8 | 16.1 | 15.5 | 24.8 | 16.1 | 16.3 | 20.7 |
| | MgO | 24.3 | 23.0 | 21.5 | 22.2 | 22.8 | 20.3 | 23.0 | 22.4 | 23.5 | 22.2 | 22.4 | 20.3 | 22.3 | 22.2 | 20.9 |
| | Total | 100.3 | 99.5 | 100.3 | 100.1 | 99.8 | 99.5 | 99.2 | 100.5 | 100.8 | 100.2 | 99.5 | 99.0 | 99.5 | 99.5 | 98.9 |
| Cations: | Si | 0.012 | 0.019 | 0.007 | 0.020 | 0.012 | 0.009 | 0.015 | 0.007 | 0.019 | 0.012 | 0.013 | 0.011 | 0.012 | 0.012 | 0.011 |
| | Ti | 0.002 | 0.001 | 0.003 | 0.003 | 0.003 | 0.003 | 0.003 | 0.002 | 0.002 | 0.003 | 0.003 | 0.005 | 0.003 | 0.003 | 0.004 |
| | Al | 1.763 | 1.638 | 1.728 | 1.384 | 1.405 | 1.692 | 1.583 | 1.620 | 1.698 | 1.449 | 1.656 | 1.554 | 1.466 | 1.448 | 1.566 |
| | Cr | 0.184 | 0.312 | 0.240 | 0.545 | 0.539 | 0.278 | 0.071 | 0.180 | 0.122 | 0.350 | 0.168 | 0.138 | 0.329 | 0.341 | 0.190 |
| | Fe2$^+$ | 0.140 | 0.145 | 0.204 | 0.170 | 0.146 | 0.232 | 0.538 | 0.394 | 0.319 | 0.368 | 0.345 | 0.581 | 0.368 | 0.375 | 0.478 |
| | Mg | 0.911 | 0.888 | 0.823 | 0.888 | 0.909 | 0.791 | 0.943 | 0.889 | 0.908 | 0.903 | 0.887 | 0.848 | 0.910 | 0.912 | 0.859 |
| | Total | 3.012 | 3.004 | 3.005 | 3.012 | 3.013 | 3.004 | 3.155 | 3.092 | 3.069 | 3.085 | 3.072 | 3.138 | 3.088 | 3.091 | 3.108 |
| With Fe$^{3+}$: | Si | 0.012 | 0.019 | 0.007 | 0.020 | 0.012 | 0.009 | 0.014 | 0.006 | 0.018 | 0.012 | 0.012 | 0.011 | 0.012 | 0.011 | 0.010 |
| | Ti | 0.002 | 0.001 | 0.003 | 0.003 | 0.003 | 0.003 | 0.003 | 0.002 | 0.002 | 0.003 | 0.003 | 0.005 | 0.003 | 0.003 | 0.003 |
| | Al | 1.756 | 1.636 | 1.725 | 1.379 | 1.399 | 1.689 | 1.505 | 1.572 | 1.660 | 1.409 | 1.617 | 1.486 | 1.425 | 1.405 | 1.511 |
| | Cr | 0.183 | 0.312 | 0.239 | 0.543 | 0.536 | 0.277 | 0.068 | 0.174 | 0.119 | 0.341 | 0.164 | 0.132 | 0.319 | 0.331 | 0.184 |
| | Fe$^{3+}$ | 0.033 | 0.011 | 0.014 | 0.031 | 0.035 | 0.011 | 0.392 | 0.237 | 0.179 | 0.221 | 0.188 | 0.351 | 0.227 | 0.235 | 0.277 |
| | Fe$^{2+}$ | 0.107 | 0.133 | 0.190 | 0.139 | 0.110 | 0.221 | 0.120 | 0.146 | 0.133 | 0.136 | 0.149 | 0.205 | 0.130 | 0.129 | 0.184 |
| | Mg | 0.907 | 0.887 | 0.821 | 0.885 | 0.905 | 0.790 | 0.897 | 0.863 | 0.888 | 0.878 | 0.866 | 0.811 | 0.884 | 0.885 | 0.830 |
| | Total | 3.000 | 3.000 | 3.000 | 3.000 | 3.000 | 3.000 | 3.000 | 3.000 | 3.000 | 3.000 | 3.000 | 3.000 | 3.000 | 3.000 | 3.000 |
| | Fe$^{3+}$/$\Sigma$Fe | 0.24 | 0.08 | 0.07 | 0.18 | 0.24 | 0.05 | 0.77 | 0.62 | 0.57 | 0.62 | 0.56 | 0.63 | 0.64 | 0.65 | 0.60 |
| | Cr/(Cr+Al) | 0.09 | 0.16 | 0.12 | 0.28 | 0.28 | 0.14 | 0.04 | 0.10 | 0.07 | 0.19 | 0.09 | 0.08 | 0.18 | 0.19 | 0.11 |

### 4.1.6. Pyroxenes

Orthopyroxene and clinopyroxene were present in several experiments. Both ranged in size from a few micrometers up to 10-15 $\mu$m diameter. Orthopyroxenes were usually equant whereas the habit of the clinopyroxenes varied from equant to slightly prismatic. Clinopyroxenes with cores of orthopyroxene were observed in some cases. Tables 4.8 and 4.9 show the chemical composition of clinopyroxenes and orthopyroxenes obtained in the experiments.

Table 4.8. Compositions of the clinopyroxenes produced in the experiments (wt.%).

| Run# | 2 | 3 | 4 | 5 | 7 | 12 | 26 | 27C | 34C |
|---|---|---|---|---|---|---|---|---|---|
| $SiO_2$ | 50.1 | 51.7 | 48.6 | 50.6 | 49.5 | 50.3 | 48.3 | 48.3 | 47.6 |
| $TiO_2$ | 0.262 | 0.194 | 0.509 | 0.225 | 0.371 | 0.240 | 0.221 | 0.636 | 0.694 |
| $Al_2O_3$ | 10.3 | 9.7 | 14.2 | 10.4 | 11.6 | 10.3 | 9.1 | 17.8 | 16.7 |
| $Cr_2O_3$ | 0.151 | 0.240 | 0.097 | 0.282 | 0.099 | 0.214 | 0.133 | 0.063 | 0.043 |
| FeO | 5.6 | 5.1 | 6.2 | 4.5 | 5.7 | 4.8 | 6.6 | 4.7 | 8.0 |
| MgO | 19.1 | 21.8 | 16.9 | 19.8 | 17.8 | 19.3 | 18.3 | 12.7 | 14.0 |
| CaO | 13.8 | 12.8 | 13.1 | 14.5 | 14.4 | 14.5 | 16.5 | 14.1 | 13.0 |
| $Na_2O$ | 0.574 | 0.532 | 0.706 | 0.547 | 0.694 | 0.539 | 0.483 | 1.491 | 1.512 |
| Total | 99.9 | 102.0 | 100.3 | 100.8 | 100.1 | 100.1 | 99.6 | 99.9 | 101.5 |
| | | | | | | | | | |
| **Cations** | | | | | | | | | |
| Si | 1.795 | 1.802 | 1.733 | 1.791 | 1.773 | 1.794 | 1.766 | 1.720 | 1.693 |
| Ti | 0.007 | 0.005 | 0.014 | 0.006 | 0.010 | 0.006 | 0.006 | 0.017 | 0.019 |
| Al | 0.436 | 0.398 | 0.596 | 0.432 | 0.488 | 0.432 | 0.392 | 0.748 | 0.700 |
| Cr | 0.004 | 0.007 | 0.003 | 0.008 | 0.003 | 0.006 | 0.004 | 0.002 | 0.001 |
| Fe | 0.168 | 0.149 | 0.186 | 0.135 | 0.170 | 0.142 | 0.203 | 0.140 | 0.237 |
| Mg | 1.020 | 1.133 | 0.898 | 1.043 | 0.952 | 1.025 | 0.996 | 0.672 | 0.742 |
| Ca | 0.528 | 0.478 | 0.500 | 0.550 | 0.553 | 0.556 | 0.645 | 0.537 | 0.495 |
| Na | 0.040 | 0.036 | 0.049 | 0.038 | 0.048 | 0.037 | 0.034 | 0.103 | 0.104 |
| Total | 3.998 | 4.008 | 3.978 | 4.002 | 3.996 | 3.999 | 4.047 | 3.940 | 3.991 |

Table 4.9. Compositions of the orthopyroxenes (wt.%).

| Run# | 2 | 3 | 4 | 5 | 7 | 11 | 12 | 26 | 27C | 30Ca | 30Fe | 34C | 35 | 35C |
|---|---|---|---|---|---|---|---|---|---|---|---|---|---|---|
| $SiO_2$ | 52.3 | 52.4 | 51.7 | 52.1 | 51.9 | 52.2 | 52.8 | 51.5 | 52.8 | 52.2 | 52.6 | 51.6 | 52.6 | 54.0 |
| $TiO_2$ | 0.132 | 0.153 | 0.126 | 0.105 | 0.109 | 0.116 | 0.099 | 0.086 | 0.099 | 0.095 | 0.074 | 0.110 | 0.106 | 0.109 |
| $Al_2O_3$ | 8.8 | 9.8 | 9.8 | 8.9 | 9.8 | 9.7 | 9.0 | 8.3 | 8.0 | 8.8 | 8.2 | 9.0 | 8.1 | 8.3 |
| $Cr_2O_3$ | 0.213 | 0.441 | 0.258 | 0.339 | 0.281 | 0.475 | 0.309 | 0.076 | 0.395 | 0.410 | 0.536 | 0.317 | 0.566 | 0.467 |
| FeO | 7.1 | 6.1 | 6.9 | 6.2 | 6.7 | 5.8 | 6.1 | 6.4 | 4.8 | 6.3 | 6.2 | 6.3 | 5.5 | 5.0 |
| MgO | 29.2 | 30.2 | 29.2 | 29.8 | 29.4 | 29.9 | 30.3 | 32.1 | 32.0 | 31.9 | 32.1 | 31.5 | 32.3 | 32.3 |
| CaO | 2.4 | 2.5 | 2.3 | 2.5 | 2.2 | 2.2 | 2.4 | 2.2 | 1.9 | 1.2 | 0.9 | 1.7 | 1.2 | 1.6 |
| $Na_2O$ | 0.115 | 0.118 | 0.117 | 0.096 | 0.097 | 0.087 | 0.089 | 0.069 | 0.059 | 0.055 | 0.054 | 0.079 | 0.045 | 0.064 |
| Total | 100.2 | 101.7 | 100.4 | 100.1 | 100.5 | 100.5 | 101.2 | 100.7 | 100.1 | 100.9 | 100.6 | 100.8 | 100.5 | 101.9 |
| **Cations** | | | | | | | | | | | | | | |
| Si | 1.816 | 1.788 | 1.791 | 1.807 | 1.796 | 1.799 | 1.810 | 1.781 | 1.818 | 1.792 | 1.810 | 1.781 | 1.808 | 1.825 |
| Ti | 0.003 | 0.004 | 0.003 | 0.003 | 0.003 | 0.003 | 0.003 | 0.002 | 0.003 | 0.002 | 0.002 | 0.003 | 0.003 | 0.003 |
| Al | 0.359 | 0.396 | 0.401 | 0.366 | 0.398 | 0.392 | 0.364 | 0.338 | 0.324 | 0.357 | 0.331 | 0.368 | 0.329 | 0.330 |
| Cr | 0.006 | 0.012 | 0.007 | 0.009 | 0.008 | 0.013 | 0.008 | 0.002 | 0.011 | 0.011 | 0.015 | 0.009 | 0.015 | 0.012 |
| Fe | 0.208 | 0.174 | 0.200 | 0.179 | 0.193 | 0.168 | 0.176 | 0.185 | 0.138 | 0.180 | 0.177 | 0.182 | 0.159 | 0.142 |
| Mg | 1.512 | 1.536 | 1.511 | 1.542 | 1.515 | 1.535 | 1.549 | 1.654 | 1.645 | 1.633 | 1.646 | 1.619 | 1.656 | 1.629 |
| Ca | 0.089 | 0.091 | 0.085 | 0.094 | 0.082 | 0.082 | 0.089 | 0.082 | 0.072 | 0.043 | 0.034 | 0.065 | 0.046 | 0.058 |
| Na | 0.008 | 0.008 | 0.008 | 0.006 | 0.007 | 0.006 | 0.006 | 0.005 | 0.004 | 0.004 | 0.004 | 0.005 | 0.003 | 0.004 |
| Total | 4.002 | 4.008 | 4.006 | 4.006 | 4.002 | 3.998 | 4.004 | 4.049 | 4.014 | 4.023 | 4.018 | 4.031 | 4.018 | 4.003 |

58

### 4.1.7. Alloys

Metallic alloys were present as run products in some runs. The alloys are mostly remnants of the HSE added as starting material in some experiments, either as powder or as discrete pieces as described in section 2.1.3. Very small grains ($<1$ $\mu$m) of Au and Pd were found in experiments contained in AuPd capsules. The composition, occurrence, and textures of the alloys are quite complex and are described in detail in section 4.5 along with the results of LA-ICP-MS analyses of HSE content in the quenched glasses.

### 4.2. Estimation of equilibrium

As discussed in section 2.5, reversals could not be used as criteria for equilibrium in these experiments. Time invariance and the use of two compositional "directions" were used to test for equilibration in experiments contained in graphite and AuPd capsules, respectively.

Experiments conducted in graphite capsules from sulfide-bearing starting materials (runs 2 to 12) and ranging in time from 1 to 48 hours have identical S concentrations (Table 4.2) indicating that equilibrium in these experiments was attained quickly ($<1$ hr). Results from paired experiments (30Fe and 30Ca; 56 and 57) using different combinations of glass and sulfate starting materials, and run for four hours, produced sulfate-saturated glasses of similar composition, showing that equilibrium is achieved within that time. Run 35C used sulfate starting material in a graphite capsule and was run for two hours. Sulfide was present as a run product, showing that reduction of sulfate to sulfide was achieved within two hours. One final test (paired experiments 39 and 40) used sulfate starting materials and was run for only one hour in graphite capsules. These experiments produced assemblages containing both sulfide and sulfate. Sulfides precipitated towards the contact with the graphite capsule whereas sulfates were still present at the center of the charge.

59

These results demonstrate that the charges reached equilibrium within one hour when sulfur was added as sulfide and run in graphite capsules. When sulfur was added as sulfate and reduced in graphite capsules to form sulfide, equilibrium is attained within two hours. When sulfur is added as sulfate and run in Au-Pd capsules to produce sulfate-bearing runs, equilibrium is also attained within two hours.

### 4.3. Oxybarometry

For runs in which both spinel and olivine were present as run products, the oxidation state of the system was calculated using the method of Ballhaus et al. (1991), as discussed in section 2.4.1.

To test the use of $Fe^{3+}$ estimates from stoichiometry based on EPMA, spinel and olivine in two spinel lherzolites (KR-35 and KR-37) from West Kettle River, British Columbia were analyzed on several occasions by EPMA along with spinel and olivine from the experimental runs. The data were used to calculate the oxidation state of these two samples and compared to the oxidation state obtained by using the spinel compositions documented in Canil et al. (1990) with $Fe^{3+}$ estimated by Mössbauer spectroscopy. To isolate the effect of the method used for $Fe^{3+}$ estimations, the same olivine composition and the same calibration of the oxybarometer (Ballhaus et al. 1991) was used in both cases. The results are summarized in Table 4.10. For KR-35 the average oxidation state (from four sessions) was estimated to be FMQ-0.35 ± 0.26 (compared with FMQ -0.31 using spinel data from Canil et al., 1990). For KR-37 the average (from five sessions) was estimated to be FMQ-1.07 ± 0.25 (compared with FMQ-0.86 using spinel data from Canil et al., 1990). These results validate the use of $Fe^{3+}$ estimations from stoichiometry based on EPMA for the calculations of oxidation state.

The other two columns in Table 4.10 are the estimates of oxidation state in both samples as documented in Canil et al. (1990) using O'Neill and Wall (1987) and Mattioli and Wood (1988) calibrations of the oxybarometer. The results indicate that the major discrepancies in estimates of oxidation state are related with the choice of oxybarometer. However, even in this case the discrepancies are well within the uncertainties associated

60

with the oxybarometers ($\pm$ 0.4 log units above FMQ, and $\pm$ 1.2 log units at $\Delta$FMQ $\approx$ -3 for the calibration of Ballhaus et al., 1991, similar uncertainties for the other two).

Table 4.10. Comparison of the oxidation state calculated for samples KR-35 and KR-37.

| | $Fe^{3+}$ from EPMA[a] Ballhaus et al. (1991) | $Fe^{3+}$ from C '90[b] | Documented in Canil et al. (1990) | |
| | | | O-W '87[c] | M-W '88[d] |
| --- | --- | --- | --- | --- |
| **KR-35** | -0.35 $\pm$ 0.26 | -0.31 | -0.81 | -0.18 |
| **KR-37** | -1.07 $\pm$ 0.25 | -0.86 | -1.45 | no data |

[a] $Fe^{3+}$ estimated from stoichiometry based on EPMA
[b] $Fe^{3+}$ from Mössbauer spectroscopy taken from Canil et al. (1990); olivine data from this work.
[c] using oxybarometer calibration of O'Neill and Well (1987)
[d] using oxybarometer calibration of Mattioli and Wood (1988)

The results for the experiments are summarized in Table 4.5 and show that the oxidation state in reduced (sulfide-saturated) experiments is < FMQ-1 whereas the oxidation state in oxidized (mostly sulfate-saturated) experiments is $\geq$ FMQ+2. Figure 4.8 illustrates the relationship between the measured sulfur concentration in the glasses and the estimated oxidation states in the experimental runs. The data on Figure 4.8 are summarized in Table 4.11.
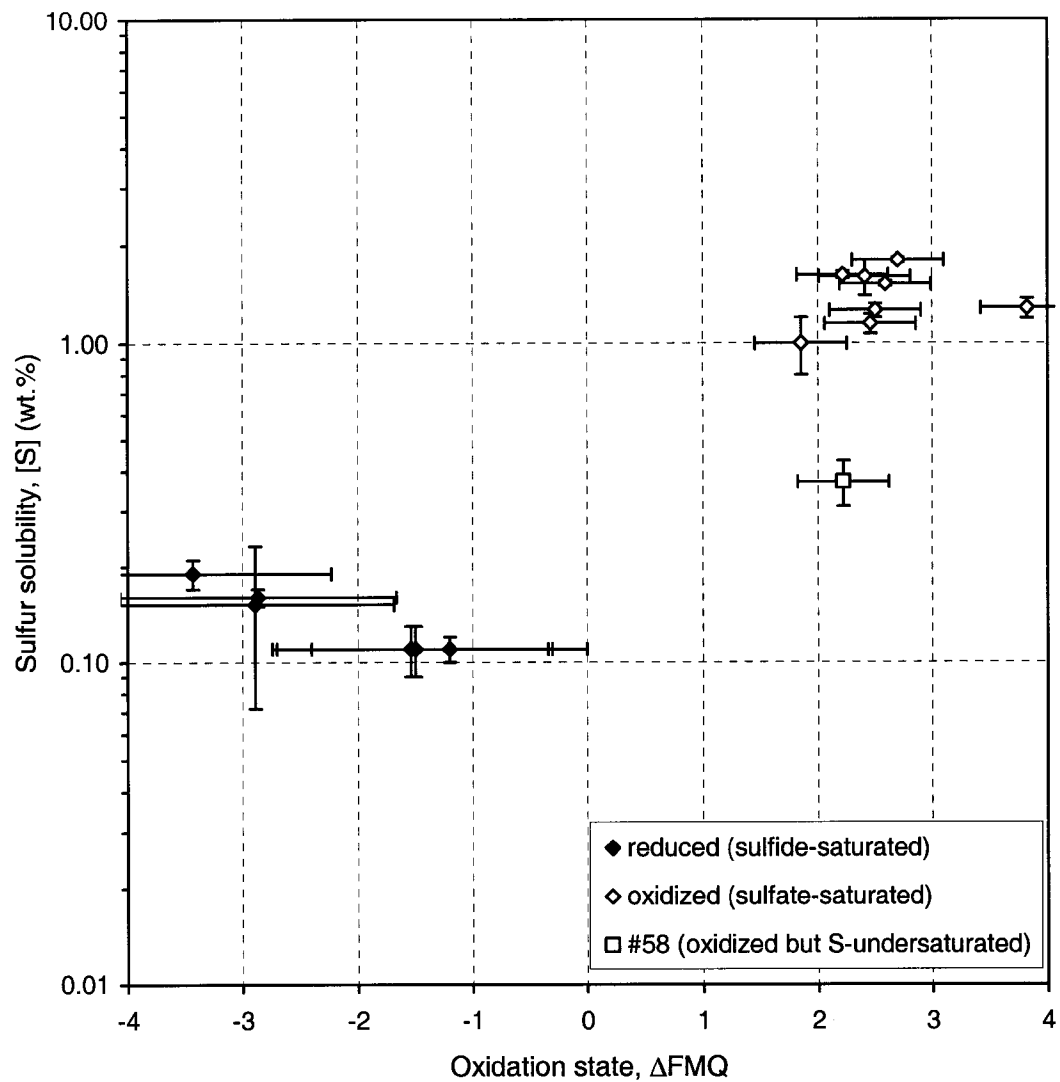
61

Figure 4.8. Sulfur concentration against oxidation state, measured in sulfate- and sulfide-bearing glasses. Sulfur concentrations measured by EPMA. Oxidation state, relative to the FMQ buffer, is calculated from olivine and spinel compositions using the oxybarometer calibration of Ballhaus et al. (1990, 1991). Error bars are 1σ standard deviation for sulfur concentrations and the uncertainties associated with the oxybarometer calibration of Ballhaus et al. (1990, 1991) (± 0.4 above FMQ and ~ ±1.2 at ~ FMQ-3).

Table 4.11. Summary of the sulfur solubility and oxidation state data.

| Run # | ΔFMQ | [S] | |
|---|---|---|---|
| **Reduced** | | | |
| **27C** | -1.20 | 0.11 | ± 0.01 |
| **35C** | -2.89 | 0.15 | ± 0.08 |
| **53** | -2.87 | 0.16 | ± 0.01 |
| **54** | -1.50 | 0.11 | ± 0.02 |
| **55** | -1.54 | 0.11 | ± 0.02 |
| **59** | -3.43 | 0.19 | ± 0.02 |
| | | | |
| **Oxidized** | | | |
| **26** | 3.82 | 1.28 | ± 0.09 |
| **30Fe** | 2.59 | 1.52 | ± 0.03 |
| **34C** | 1.85 | 1.00 | ± 0.2 |
| **35** | 2.41 | 1.60 | ± 0.2 |
| **50** | 2.22 | 1.62 | ± 0.04 |
| **52** | 2.70 | 1.80 | ± 0.03 |
| **56** | 2.46 | 1.15 | ± 0.08 |
| **57** | 2.50 | 1.26 | ± 0.06 |
| **58** | 2.22 | 0.37 | ± 0.06 |

63

## 4.4. Sulfur speciation versus oxidation state

Sulfur speciation in the experimental glasses was measured as outlined in section 3.2. The SKα peak profiles were measured in both the sphalerite and the barite standards several times during each session to estimate the peak shift and monitor for drift in the spectrometer during analysis. Figure 4.9 illustrates typical S Kα peaks for the standards and the shift in the peak position caused by the valence difference. Although the peak shift was consistent in all sessions, the absolute peak positions moved slightly (up to 0.13 pm) between sessions. Peak shift in the samples were estimated relative to the averaged peak position for the sphalerite standard measured in the same session as the sample. Figure 4.10 show examples of the peaks obtained for a sulfide-bearing and a sulfate-bearing experiment (runs 54 and 52, respectively) used to estimate sulfur speciation. The results are summarized in Table 4.12 and plotted against oxidation state in Figure 4.11. The standard deviation associated with the peak shift between sphalerite and barite (0.304 ± 0.010 pm) results in an uncertainty of 0.03 in $X(S^{6+})$ associated to the $X(S^{6+})$ scale. Thus, although uncertainties in Table 4.12 are the standard deviation of replicate analyses (2 for sulfide-bearing glasses and 2 or 3 analyses for sulfate-bearing samples), uncertainties in Figure 4.11 are those quoted in Table 4.12 or ± 0.03 whichever is higher.

The sulfur speciation in the glass in sulfide-saturated experiments ranges from $X(S^{6+})$ = -0.05 to $X(S^{6+})$ = 0.13. Negative values for runs 12 and 53 reflect the larger uncertainty associated with the low sulfur content of the sulfide-saturated samples, and the scattering of the data around $X(S^{6+})$ = 0. The relatively higher sulfate fraction in glasses from runs 27C and 35C (produced from sulfate-bearing starting material run in graphite capsules) along with their significantly larger error indicates that a significant proportion of sulfate species were still present in the glass. This effect is not seen in runs 54 and 55 in which graphite powder was mixed with the starting material before loading into AuPd capsules. The average of seven sulfide-saturated experiments (with the exception of runs 27C and 35C) yields $X(S^{6+})$ = 0.03 ± 0.04, as expected for the low oxidation state of those runs.
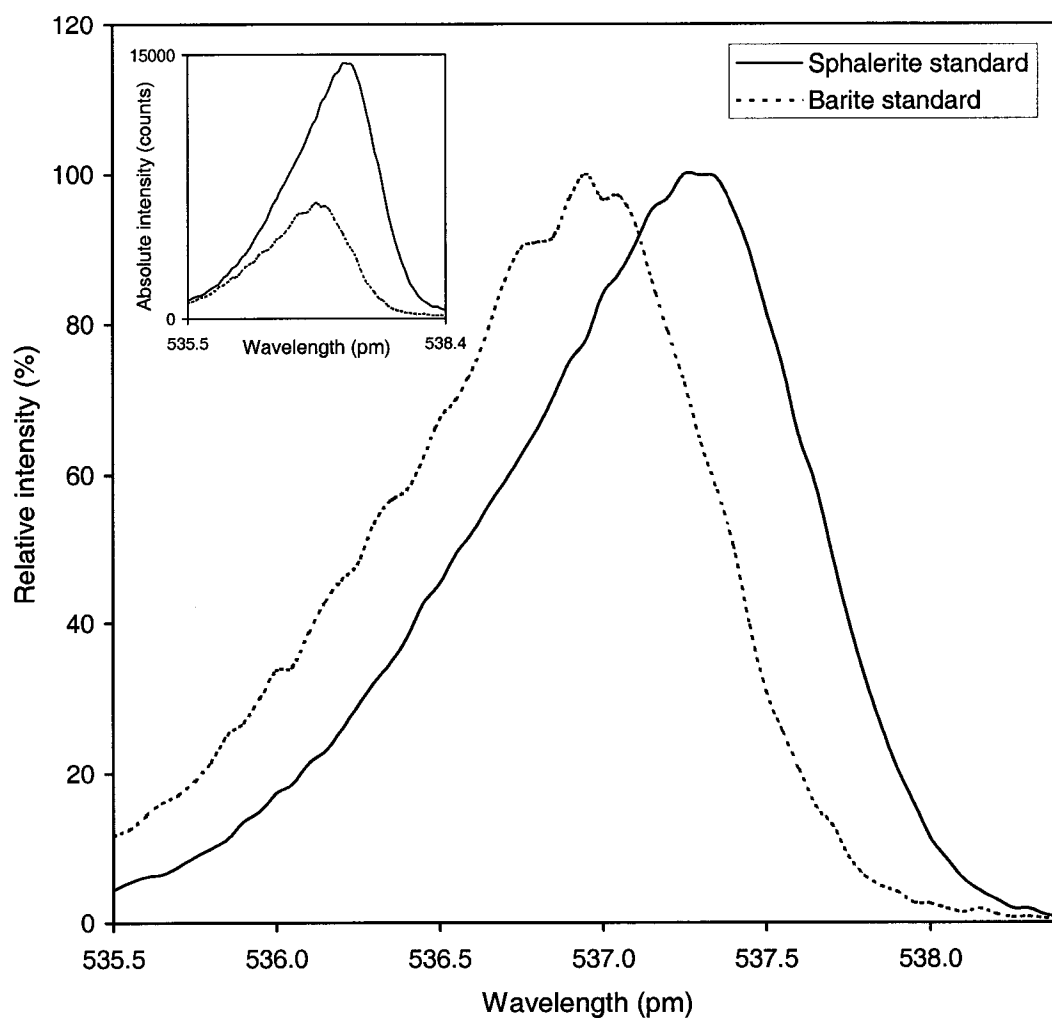
Figure 4.9. Example of the SKα peak profiles measured in sphalerite and barite standards normalized to relative intensities and with background subtracted. Original profiles in absolute intensities are shown in the insert. Measurement conditions were identical for both standards, the difference in intensities reflect the different proportions of sulfur in sphalerite and barite (32.9 and 13.7 wt.% respectively). Wavelength scale in picometers (1 pm = $10^{-12}$ m).
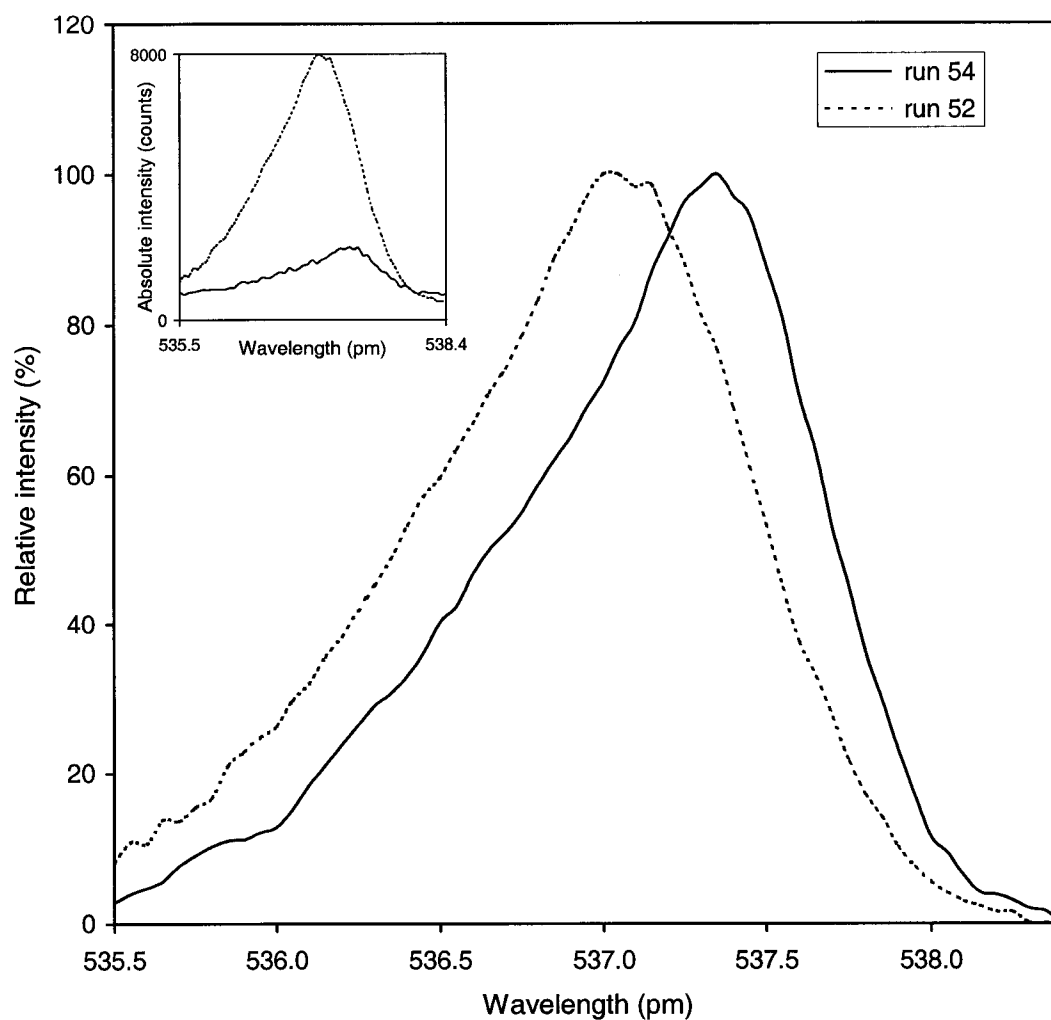
Figure 4.10. Example of the SKα peak profiles measured in the glasses. Runs 54 and 52 are examples of sulfide- and sulfate-saturated experiments, respectively. The peaks were background-corrected and converted to relative intensities. The peak for run 54 has been smoothed by a factor of 3 to reduce noise. The insert shows the original profiles in absolute intensities for both measurements. Measurement condition for the examples shown were identical except for the dwell time (30 s and 60 s for the sulfate- and sulfide-bearing samples, respectively).

66

Table 4.12. Sulfur speciation estimates for glasses and sulfates.

| Run# | ΔFMQ | X(S$^{6+}$) | 1σ |
|---|---|---|---|
| | **sulfide-saturated** | | |
| **4** | ne[a] | 0.05 | 0.02 |
| **7** | ne | 0.08 | -[b] |
| **12** | ne | -0.01 | 0.08 |
| **27C** | -1.18 | 0.13 | 0.16 |
| **35C** | -2.89 | 0.12 | 0.16 |
| **53** | -2.87 | -0.05 | 0.10 |
| **54** | -1.50 | 0.01 | 0.08 |
| **55** | -1.54 | 0.06 | 0.03 |
| **59** | -3.43 | 0.05 | 0.03 |
| | **sulfate-saturated** | | |
| **26** | 3.82 | 0.82 | 0.04 |
| **30Fe** | 2.59 | 0.92 | 0.02 |
| **34C** | 1.85 | 0.78 | 0.02 |
| **35AuPd** | 2.41 | 0.77 | 0.02 |
| **50** | 2.22 | 0.76 | 0.01 |
| **52** | 2.70 | 0.76 | 0.07 |
| **56** | 2.46 | 0.90 | 0.04 |
| **57** | 2.50 | 0.79 | 0.03 |
| **58[c]** | 2.22 | 0.55 | 0.10 |
| | **sulfate blebs** | | |
| **26** | 3.82 | 1.13 | 0.10 |
| **30Fe** | 2.56 | 1.21 | 0.01 |
| **34C** | 1.85 | 1.29 | - |

Notes:  [a] ne = not estimated
[b] only one measurement
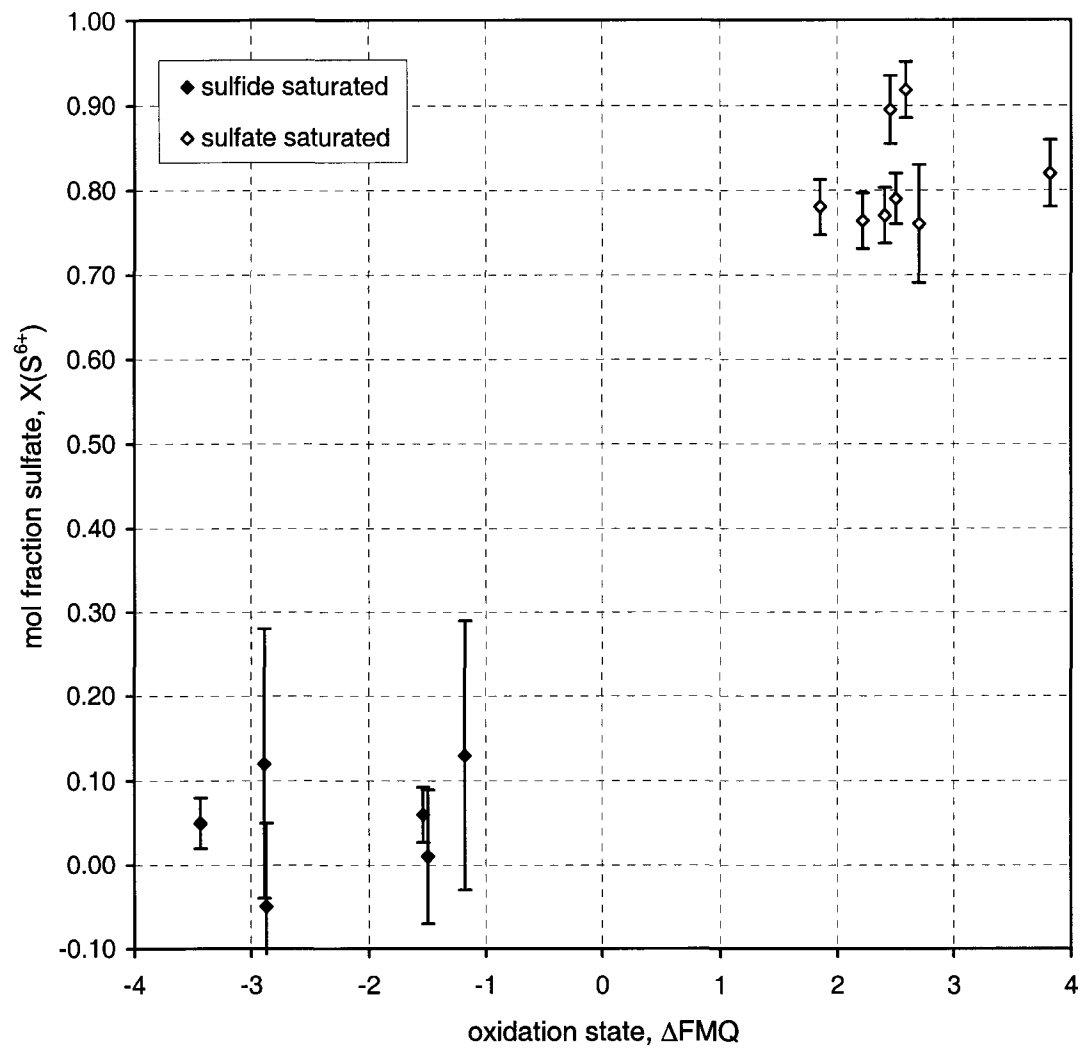[c] oxidized but sulfate-undersaturated

67

Figure 4.11. Sulfur speciation against oxidation state measured in glasses from this work.

68

In sulfate-saturated experiments $X(S^{6+})$ ranged from 0.76 to 0.92. Average from eight samples yields $X(S^{6+}) = 0.81 \pm 0.06$. Estimates of $X(S^{6+})$ for run 26 (at $\Delta FMQ+3.82$) indicate that this level ($X(S^{6+}) \approx 0.8$) is the maximum value for sulfate speciation in the glass at the conditions of these experiments, with no further increase in $X(S^{6+})$ with increasing oxidation state. Sulfur speciation in run 58 (produced from sulfide-bearing starting material) was estimated to be $0.55 \pm 0.10$. The lower $X(S^{6+})$ values estimated in this sample likely reflect incomplete oxidation of sulfide species to sulfate species.

The sulfate content was also estimated in a few sulfate blebs following the same method used for the glasses. In all cases $X(S^{6+}) > 1$, the average of three samples yielding $X(S^{6+}) = 1.22 \pm 0.06$ (Table 4.12, bottom). Because $S^{6+}$ is the highest oxidation state known for sulfur these values likely reflect a systematic error. One possible explanation is related with the uneven surface of the sulfate blebs in the polished section. Correct focusing of the sample is not possible and a large portion of the sulfate is likely to be below the focal plane. Because peak shifts are measured on very small variations of peak position (which in turn are dependent on spectrometer geometry) X-rays generated below the focal plane will be shifted systematically relative to X-rays generated on the focal plane.

## 4.5. Highly siderophile elements

### 4.5.1. HSE concentrations in quenched glasses by LA-ICP-MS

Twelve runs (26, 34C, 35C, 50, 52, 53, 54, 55, 56, 57, 58, and 59) were selected for analysis of the concentrations of Pd, Ir, Pt, and Au by LA-ICP-MS at the Department of Earth Sciences at Memorial University of Newfoundland, as described in section 3.2.

One hundred and sixteen time-resolved measurements (counts per second of every measured isotope versus time) were collected from the samples. These represent concentrations as a function of depth as the laser ablates the sample. The most important result from the analyses is the occurrence of multiple spikes (abrupt increases in counts per second) in almost all the measurements, which indicates that the HSE were present as small nuggets in every experiment analyzed. The intensity and duration of the spikes produced by these nuggets indicate that their dimensions are in the nanometer scale range. Several spectra produced steady count rates for the isotopes measured as a function of time, indicating that nuggets were absent in the ablated volume, and that these count rates reflect the amount of HSE dissolved in the quenched glasses.

To estimate concentrations of the HSE, only sections of spectra in which plateaus defining stable count rates could be identified were used for the calculations. Figure 4.12 illustrates one example of an ablation profile in which the count rates for the measured isotopes are steady, especially for Au and Pd. The scatter in Pt and Ir can be attributed to the low concentrations of these two metals in the sample, which translates to higher uncertainties. The low intensity for Pt and Ir could be caused by low solubility or by incomplete equilibration of these two metals with the glass.

Figure 4.13 illustrates the time-resolved spectra from an ablation pit in a sulfate-saturated glasses in which a single, well-defined nugget produced a large spike in the spectra for all four HSE measured.
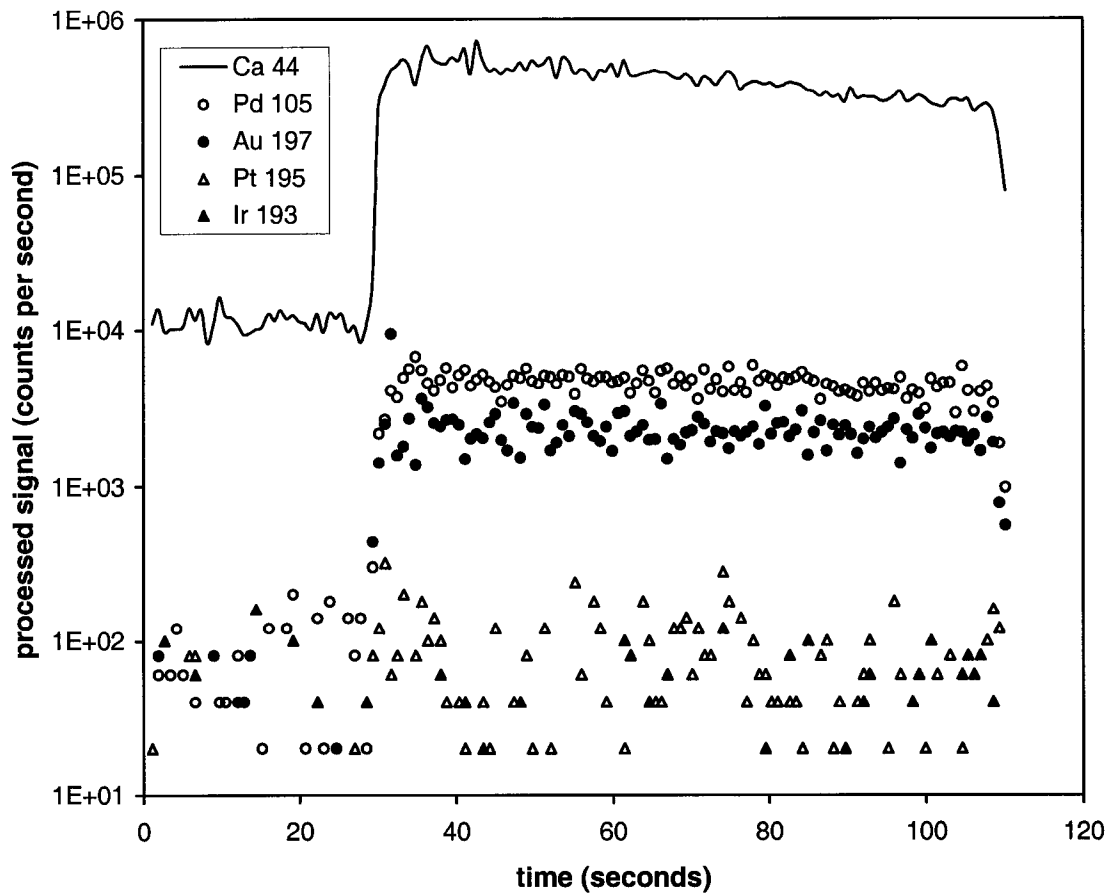
70

Figure 4.12. Example of LA-ICP-MS time-resolved spectra for $^{44}$Ca and the four HSE analyzed in the quenched glasses. This example is from an ablation pit in run 57 and illustrates stable and continuous plateaus for the $^{105}$Pd and $^{197}$Au spectra, indicating homogeneity in the glass and lack of nuggets. The scattering in the spectra for $^{193}$Ir and $^{195}$Pt could be caused by heterogeneous distribution of these two elements in the glass or variations in the count rate associated with the small amounts present for these two metals. Calcium (as $^{44}$Ca) is shown because it marks the onset of ablation with respect to background count at t $\approx$ 30 s. HSE concentrations calculated from this spectra yields Pd = 14.18 ppm, Au = 3.91 ppm, Pt = 0.14 ppm, and Ir < detection.
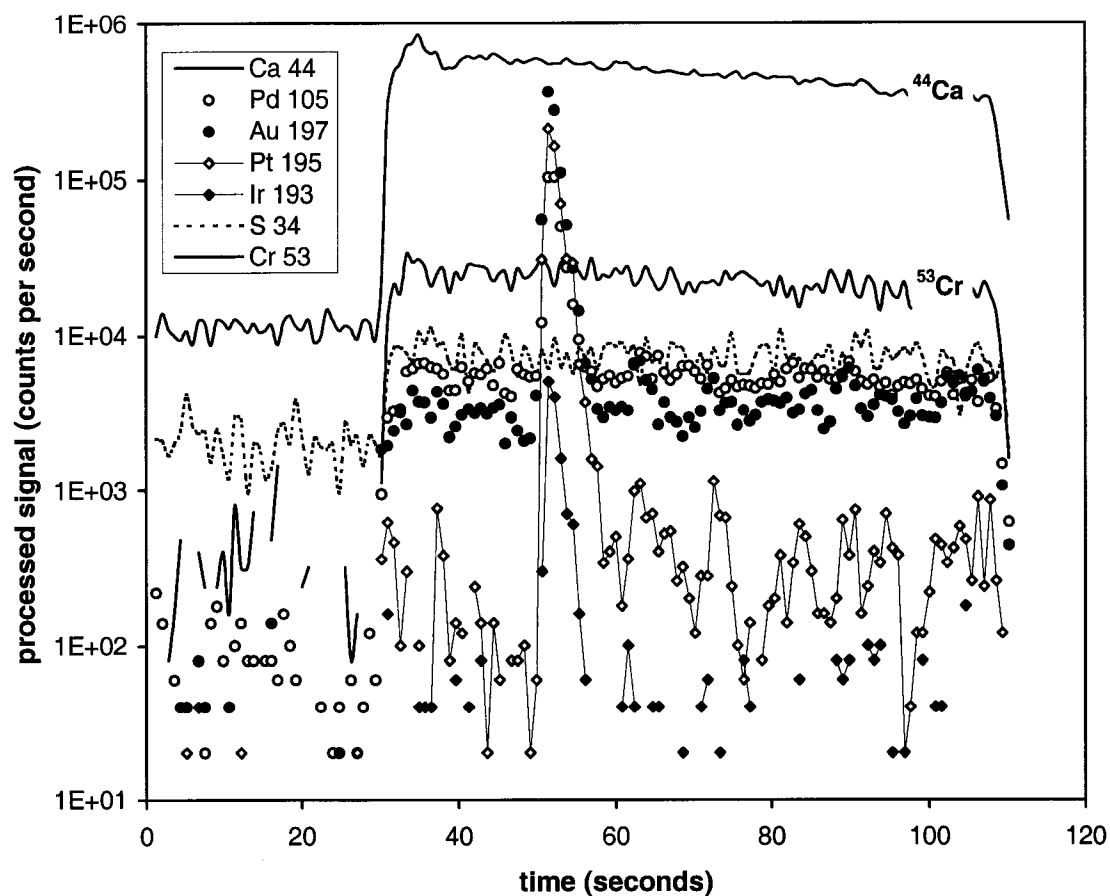
71

Figure 4.13. Example of LA-ICP-MS time-resolved spectra from an ablation pit containing a single, well-defined HSE-nugget in run 56. The large spike produced by the nugget starts at t ≈ 50 s; the count rates for four analyzed HSE increasing abruptly with respect to their average values at that point. The spectra for the $^{34}S$ and $^{53}Cr$ isotopes are included to show that the nugget is neither a sulfide nor associated with spinel.

Figure 4.14 shows an ablation pit in sulfide-bearing run 53. As seen in the insert, the ablated site is located in close proximity (~25 $\mu$m) to several sulfide blebs and olivine crystals. However, neither of these two phases were present on the surface of the ablated site. The time-resolved spectra obtained from this ablation pit are shown in Figure 4.15. Two metallic nuggets can be detected on the spectra. The first one, close to the onset of ablation (at t $\approx$ 35 s) is unrelated to any S or Cr increase. This likely corresponds to a nugget just below the polished surface or to a nugget too small to be detected in BSE imaging. The second one (at t $\approx$ 90 s) produced significantly larger counts for the four HSE measured than the first nugget. In this case, the increase is synchronous with an increase in the signal for S, implying the association of the nugget with a sulfide phase, most likely as an alloy inclusion in a sulfide bleb (as seen in section 4.1.2, Figure 4.4). The volume ablated between the two nuggets produced very low counts for the HSE compared to the counts obtained in sulfide-free, sulfate-bearing runs shown in Figures 4.12 and 4.13 and documents the lower solubilities of the HSE under reducing conditions.

The spectra shown so far correspond to one of the best spectra collected (Figure 4.12) and two spectra in which nuggets were few and easily recognized and baselines could be recognized and integrated to obtain the concentration of the HSE in the glass (Figures 4.13 and 4.15). However, the random occurrence of nuggets and their variable size (as indicated by peak size) was ubiquitous in most of the ablation pits, in some cases exceeding the upper limit in counts per second of the ICP-MS software used, causing its failure with loss of the data collected. Figures 4.16 and 4.17 illustrate a case of high nugget density in an ablation site and the possible relationship to other phases present. The ablation site is from run 58, which is oxidized but did not precipitate any sulfur-bearing phase. Figure 4.16 is a collage of various BSE images at different scales to illustrate the ablation site relative to other phases and the capsule walls, and details of the nano-nuggets observed in the BSE images. The ablation area was purposely chosen to be away from the capsule walls and in an area with high density of spinel crystals in order to detect the relationship between HSE concentration and the presence of spinel. Figures 4.16 C and D show clearly the presence of very small nuggets (estimated diameter ~ 500 nm) in the proximity of the ablation site.
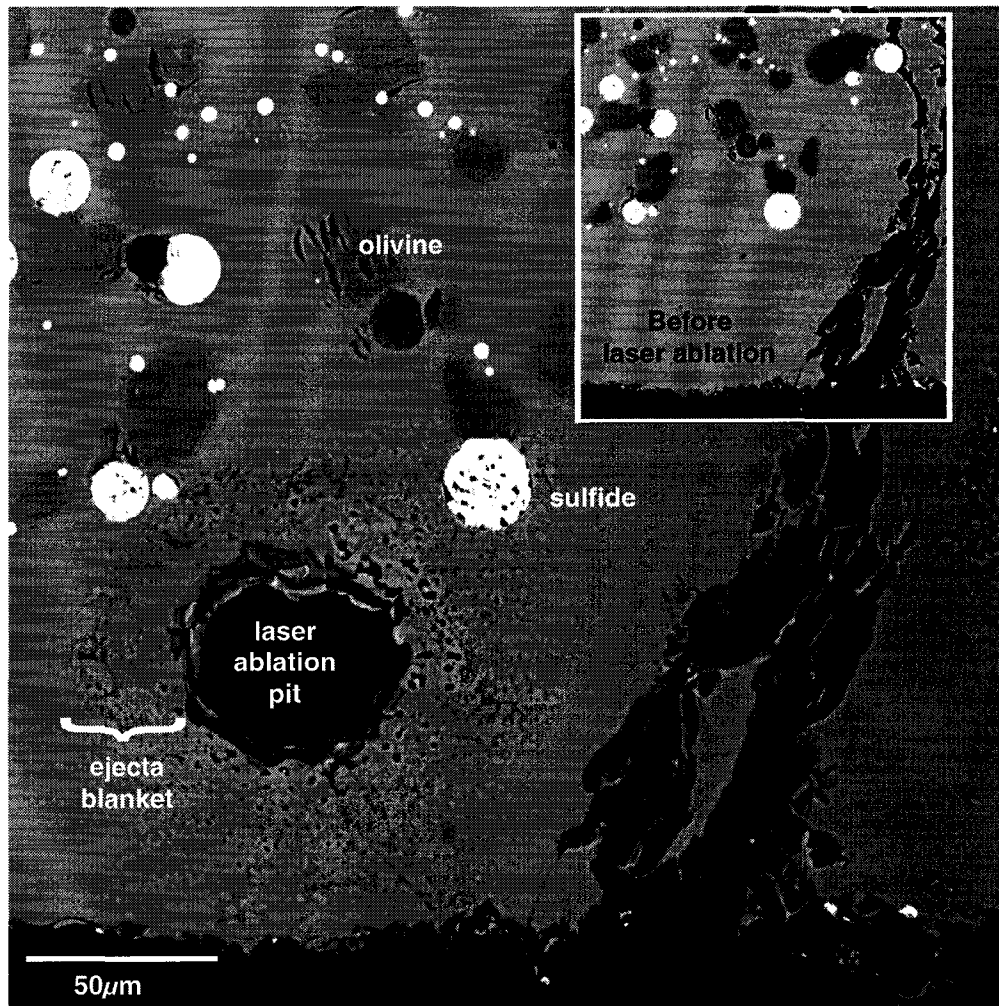
73

Figure 4.14. BSE images showing the location of the laser ablation pit and associated ejecta blanket relative to other phases in run 53, corresponding to the LA-ICP-MS measurements shown in Figure 4.15. The upper right insert shows the location of the pit before ablation. Note the proximity of discrete sulfide blebs. Black areas at the bottom and diagonally through the picture are the wall of the graphite capsule and quench-cracks respectively. White sulfide blebs and dark grey olivine are labeled. Some equant spinel crystals (relatively small, light grey) can be seen among sulfides and olivine in the upper left corner.
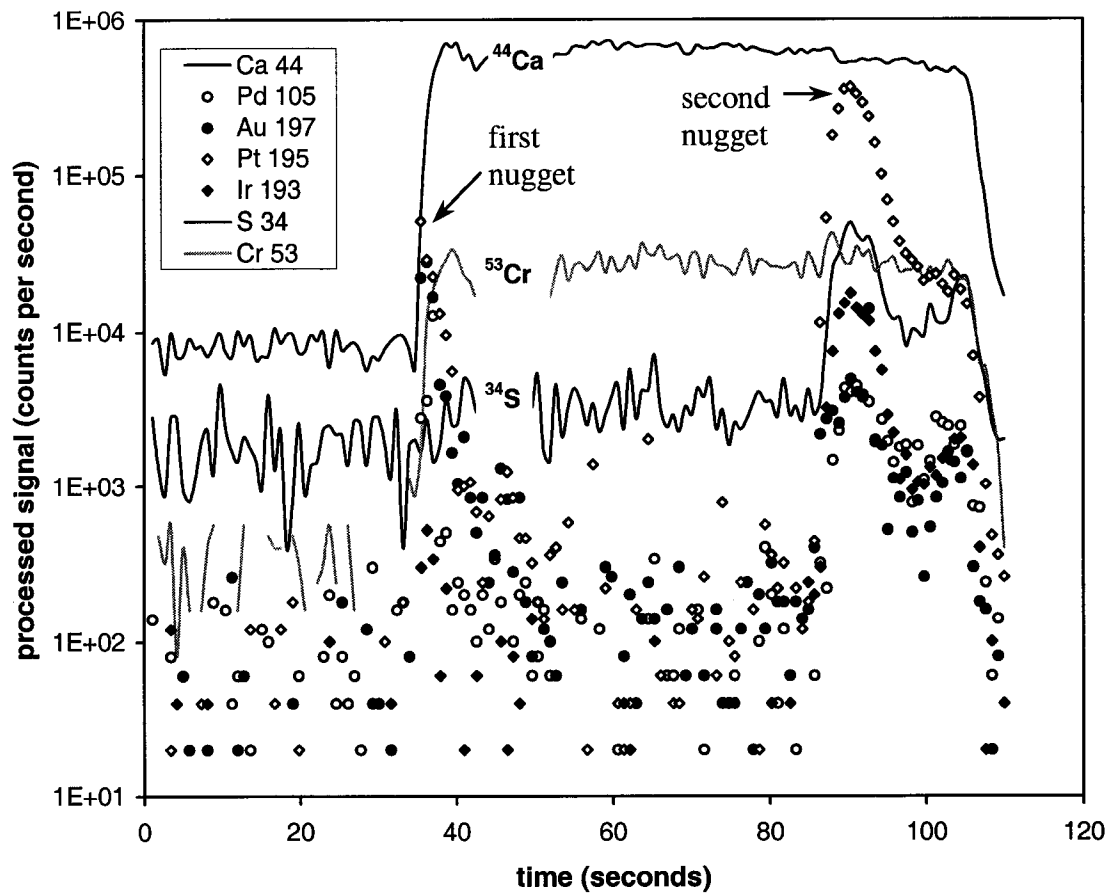
74

Figure 4.15. Example of LA-ICP-MS time-resolved spectra of an ablation pit containing two well-defined nuggets. These spectra are from the ablation pit in run 53 shown in Figure 4.14.
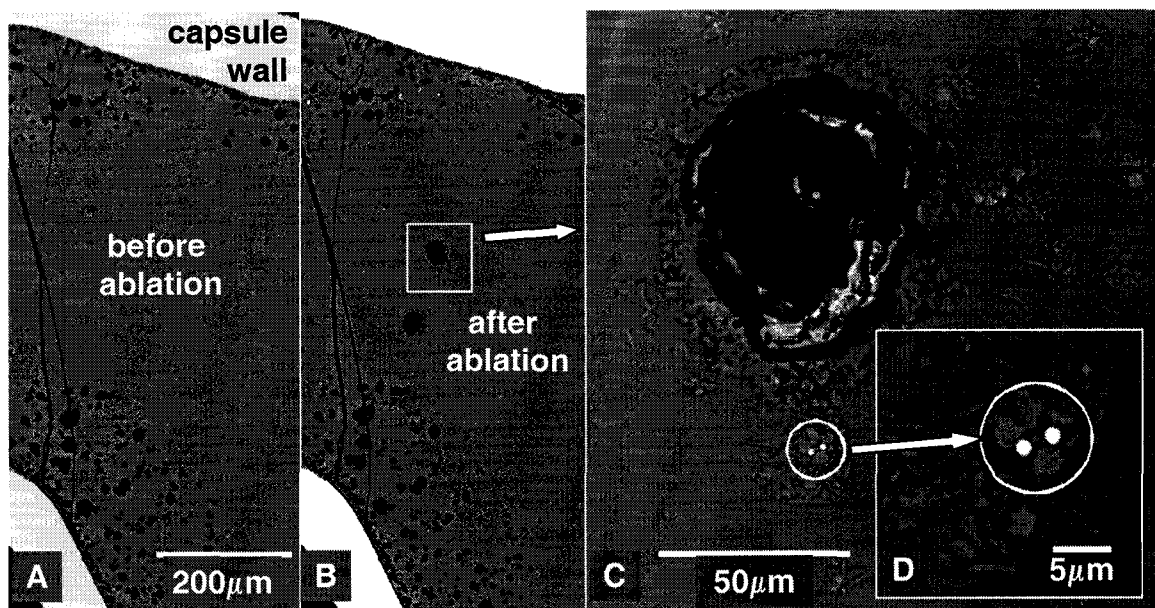
Figure 4.16. BSE images showing the location of a laser ablation pit in run 58 relative to other phases and the capsule walls.

**A:** Sample before ablation.

**B:** Sample after ablation. In both cases the white areas near the top margin and bottom left of the pictures are the AuPd capsule walls. The long dimension of the picture corresponds approximately to a cross-section of the capsule. The ablation site was chosen to be half way between capsule walls. Dark grey olivine crystals can be seen at top and bottom of the picture. The remaining medium-grey area with dusty appearance is the quenched glass with dispersed spinel crystals.

**C:** Detail of the ablation pit and surrounding area. Notice the abundance of spinel with vermiform overgrowth and the presence of two visible nuggets in the proximity.

**D:** Close up of the two nuggets circled in **C**. Notice that the nuggets are surrounded by several spinel crystals but not included in them. Their apparent size (~1 $\mu$m) is caused by their brightness relative to other phases in BSE imaging. Their real diameter is ~500 nm.

Figure 4.17 shows highly variable spectra for all the HSE elements with no correlation with variations in sulfur concentration (effectively constant sulfur; no sulfides or sulfates being present in this sample). The HSE peaks are asynchronous with variations in Cr (Fig. 4.17), consistent with the HSE being present as discrete alloys and not as solid solution in spinel. Note how the spectra for the four HSE define sub-parallel and synchronous patterns showing uniform metal ratios (Pd>Au>Pt>>Ir) in all the nuggets ablated in this sample. In contrast, the relative intensities in the HSE spectra between the two nuggets shown in Figure 4.15 are different, the second nugget containing more Pt and Ir than the first one. In general, the dominant compositions (inferred from their LA-ICP-MS spectra) for the nuggets in sulfate saturated samples are Au≥Pd>Pt>Ir, whereas in sulfide saturated samples the dominant population of nuggets have relative intensities in the order Pt>>Au≥Pd>Ir.

To calculate HSE concentration in the glass, only time intervals in which flat "valleys" could be identified were integrated. Signals interrupted by spikes were split and integrated in two and in some cases three steps to minimize the nugget effect. Spectra with no identifiable valleys or with obvious "false valleys" (e.g., Figure 4.17) were not used. Some of the samples (26, 34C, and 35C) contained numerous remnants of the Pt and Ir powders added as starting material and were analyzed only for Pd and Au. The amount of nuggets in run 26 produced heavily spiked spectra that could not be used for reliable estimation of the concentration of any of the HSE (calculated values from minima in several measurements yields Pd = 62 ± 17 ppm and Au = 9.5 ± 5.2 ppm). Results of the analyses for all samples are summarized in Table 4.13 for sulfide-saturated experiments and in Table 4.14 for oxidized experiments (5 sulfate saturated plus run 58).

The concentrations of Pd and Au in the glasses are significantly higher in the oxidized runs than in the reduced runs, but there is no significant change in the Pt and Ir concentrations.
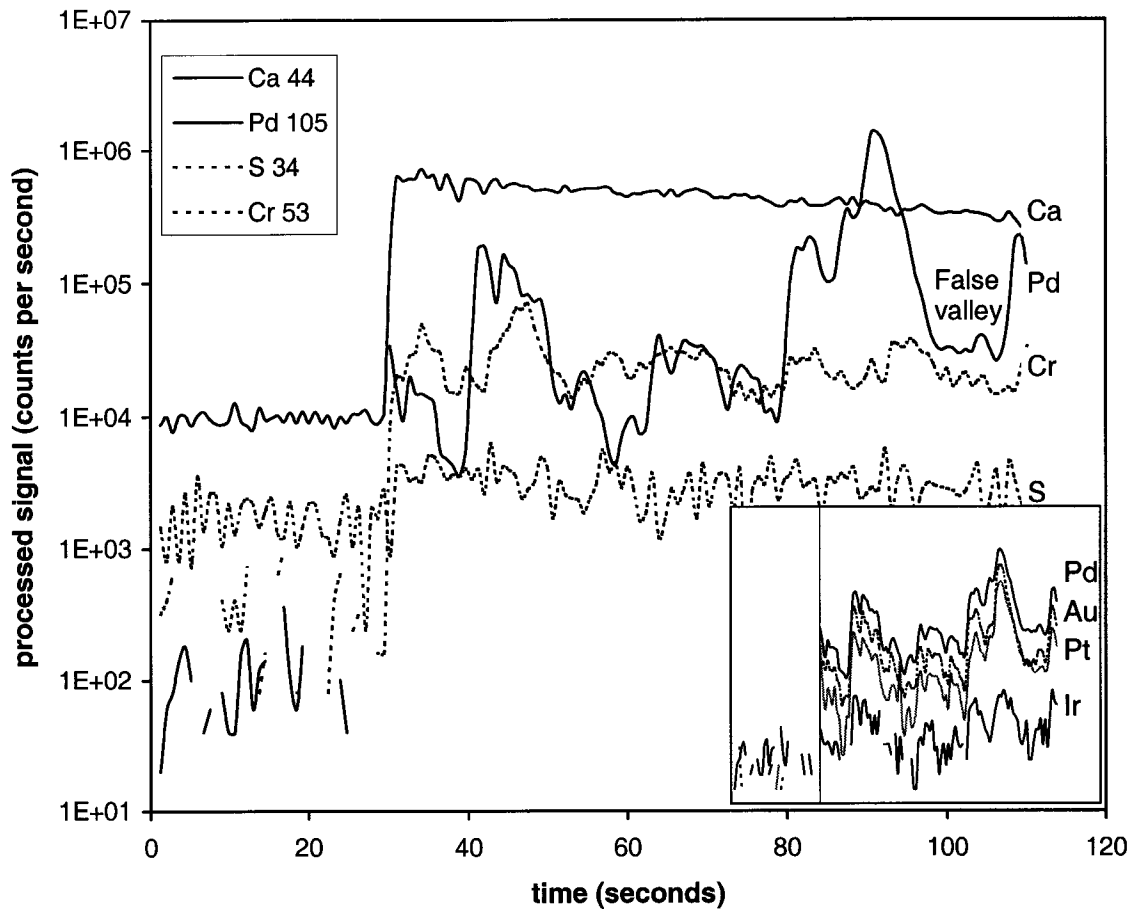
77

Figure 4.17. Example of extremely noisy LA-ICP-MS spectra caused by buried nano-nuggets in the ablation pit shown in Figure 4.16. The spectra are split in two plots for clarity. The larger plot illustrates the heavily spiked count rates for Pd and its association with the spiked count rates for Cr, while the count rates for S remains relatively steady. Note that the peaks for Pd and Cr are not in phase. The decoupled behavior between Cr and Pd indicates that Pd is not present in spinel as solid solution. The insert shows the spectra for the four HSE analyzed. The four spectra are synchronous indicating that, in this ablation site, the compositions of the alloy phases are similar. Time-resolved spectra like this one were not used for calculations of HSE concentrations.

78

Table 4.13. Concentrations of Pd, Ir, Pt, and Au in sulfide-saturated runs (in ppm).

| Run# | Pd | 1σ | Ir | 1σ | Pt | 1σ | Au | 1σ |
|------|------|--------|--------|--------|------|--------|------|--------|
| 35C | 0.13 | (0.25) | na[a] | | na | | 0.26 | (0.29) |
| 53 | 0.07 | (0.24) | 0.02 | (0.07) | 0.42 | (0.50) | 0.38 | (0.44) |
| 54 | 0.70 | (0.88) | 0.28 | (0.39) | 2.62 | (1.45) | 0.57 | (0.73) |
| 55 | 1.60 | (1.79) | 0.19 | (0.42) | 1.54 | (1.03) | 0.79 | (0.55) |
| 59 | bl[b] | | 0.46 | (0.74) | 0.35 | (0.19) | 0.61 | (0.64) |
| Ave. | 0.63 | | 0.24 | | 1.23 | | 0.52 | |
| 1δX[c] | 0.31 | | 0.08 | | 0.46 | | 0.08 | |

[a] na = not analyzed
[b] bd = below detection
[c] standard deviation of the mean ( $\delta X = \sigma_x / \sqrt{n}$ )

Table 4.14. Concentrations of Pd, Ir, Pt, and Au in oxidized runs (in ppm).

| Run# | Pd | 1σ | Ir | 1σ | Pt | 1σ | Au | 1σ |
|------|-------|--------|--------|--------|------|--------|------|--------|
| 34C | 7.17 | (2.13) | na[a] | | na | | 2.28 | (0.78) |
| 50 | 9.99 | (2.92) | 0.14 | (0.24) | 1.92 | (2.02) | 4.42 | (1.39) |
| 52 | 10.78 | (3.91) | 0.08 | (0.13) | 1.74 | (1.98) | 5.08 | (2.17) |
| 56 | 15.52 | (2.29) | 0.09 | (0.17) | 1.87 | (2.06) | 8.17 | (2.48) |
| 57 | 14.49 | (2.16) | 0.04 | (0.06) | 2.11 | (2.56) | 6.20 | (2.30) |
| 58 | 13.48 | (2.74) | 0.02 | (0.04) | 0.36 | (0.60) | 1.92 | (0.70) |
| Ave. | 11.9 | | 0.07 | | 1.6 | | 4.7 | |
| 1δX[b] | 1.2 | | 0.02 | | 0.3 | | 0.9 | |

[a] na = not analyzed
[b] standard deviation of the mean.

79

## 4.5.2. Composition of metallic alloys

The composition of the coexisting alloys was not examined in detail. In runs in which Pt and Ir were added as powder and which were saturated in sulfides, the composition of enclosed nuggets (Table 4.4) is variable and related to whether the sulfide bleb enclosed an Ir or a Pt particle. In experiments in which the HSE were added as discrete pieces of wire, these were rarely exposed in the sections prepared for EPMA because of their very small volume relative to the capsules. In run 52, a piece of the added $Pt_{80}Ir_{20}$ wire was exposed during sample preparation and analyzed by EPMA. In run 59 a complex bleb, containing S and the four HSE added to the charge, was present and was analyzed in detail by EPMA. The small pieces of alloy shown in Figure 4.16 for run 58, were also analyzed, but their small size resulted in very low totals. A single, larger (~1 $\mu$m) isolated bleb in the same run gave an example of the composition of these blebs. The results of these analyzes are presented in Table 4.15 and are explained in detail below.

Table 4.15. Compositions of the phases containing HSE in runs 52, 58, and 59 (wt.%).

|  | 52, Pt-Ir | 58, Au-Pd[a] | 59, Fe-S | 59, Pd-S | 59, Pt-Ir-Fe | 59, Au-rich |
|---|---|---|---|---|---|---|
| **S** | 0.05 (0.02)[b] | 9.02 | 37.6 (0.9) | 15.9 (4.6) | 0.02 (0.01) | 0.23 (0.29) |
| **Fe** | 0.16 (0.20) | 0.66 | 59.5 (0.9) | 5.1 (1.3) | 12.8 (0.1) | 3.10 (0.31) |
| **Pd** | 0.06 (0.05) | 82.1 | 0.99 (0.67) | 80.7 (4.7) | 2.96 (0.27) | 7.07 (0.45) |
| **Ir** | 20.4 (0.1) | bd | 0.47 (0.31) | bd | 15.8 (3.1) | bd |
| **Pt** | 78.8 (0.3) | bd | 0.16 (0.13) | 0.12 (0.19) | 70.0 (1.1) | 5.0 (1.7) |
| **Au** | 0.13 (0.09) | 8.57 | 0.02 (0.03) | 1.6 (1.0) | 9.3 (1.0) | 80.8 (2.2) |
| **Total** | 99.4 (0.3) | 100.3 | 98.7 (1.1) | 103.3 (1.1) | 110.9 (1.7) | 96.3 (0.4) |

[a] only one bleb large enough to give total close to 100
[b] numbers in parenthesis are the standard deviation (1$\sigma$).
bd = below detection

The added $Pt_{80}Ir_{20}$ alloy (by wt) in run 52 is effectively unchanged from its original composition and contains only small amounts of S, Fe, Pd, and Au. In contrast, the single metallic bleb analyzed in run 58 is dominantly Pd with small amounts of Au and S, trace

80

amounts of Fe and no measurable Ir or Pt. The composition of this alloy is almost the opposite of the composition of the capsule ($Au_{80}Pd_{20}$ by wt.), which was the source of Au and Pd metals for that run.

The nature and texture of the phases containing HSE found in run 59 are quite complex and are illustrated in Figures 4.18 and 4.19. For this experiment, sulfur was added as sulfide, Pt and Ir as pieces of $Pt_{80}Ir_{20}$ wire, and Au and Pd as pieces of $Au_{80}Pd_{20}$. Figure 4.18 shows how these three phases coalesced during the experiment to form a single, relatively large bleb (~ 500 $\mu$m diameter), which quenched to form four distinct domains in terms of their S, Fe, Pd, Ir, Pt, and Au concentrations. The nature of these domains is better seen in Figure 4.19 for a sector of the bleb. The most significant aspect that can be gathered from these pictures is the different association of the four HSE present. The top three pictures in Figure 4.19 (S, Fe, and Pd maps) show that the rim surrounding the bleb is composed of quenched Fe-S-rich and a Pd-S-rich phases which were probably part of a single sulfide liquid at run conditions. Blebs of Pt-Ir-Fe alloy and interstitial Au-rich material form the core zone of the bleb. Palladium mobilization from the added AuPd alloy into the sulfide resulted in a Au-rich immiscible liquid. The liquid nature of the Pt-Ir-Fe phase as interpreted from the textures seen in Figure 4.19 is at odds with the highly refractory nature expected in Pt-Ir-Fe alloys (with melting points above 1500 °C at 1 atm, Massalski, 1986). However, incorporation of carbon and sulfur should decrease the melting point of the alloy.

The compositions presented in Table 4.15 are the result of 5 to 11 analyses for each of the four domains shown in Figures 4.18 and 4.19 and illustrate the geochemical affinities of the HSE involved. The Fe-S phase is similar to that measured in sulfides from other runs (and from the smaller sulfide blebs dispersed in run 59). It contains ~ 1 wt.% Pd, 4700 ppm Ir, 1200 ppm Pt and 200 ppm Au. The Pd-S rich phase contains no measurable Ir and ~ 1200 ppm Pt, 5 wt.%Fe and 1.6 wt.% Au. If these two phases were part of a single immiscible liquid, then upon exsolution the pyrrhotitic phase retained all the Ir relative to the Pd-S phase, Au partitioned preferentially with Pd (by a factor of ~80), whereas Pt partitioned equally between the pyrrhotitic phase and the Pd-rich sulfide.
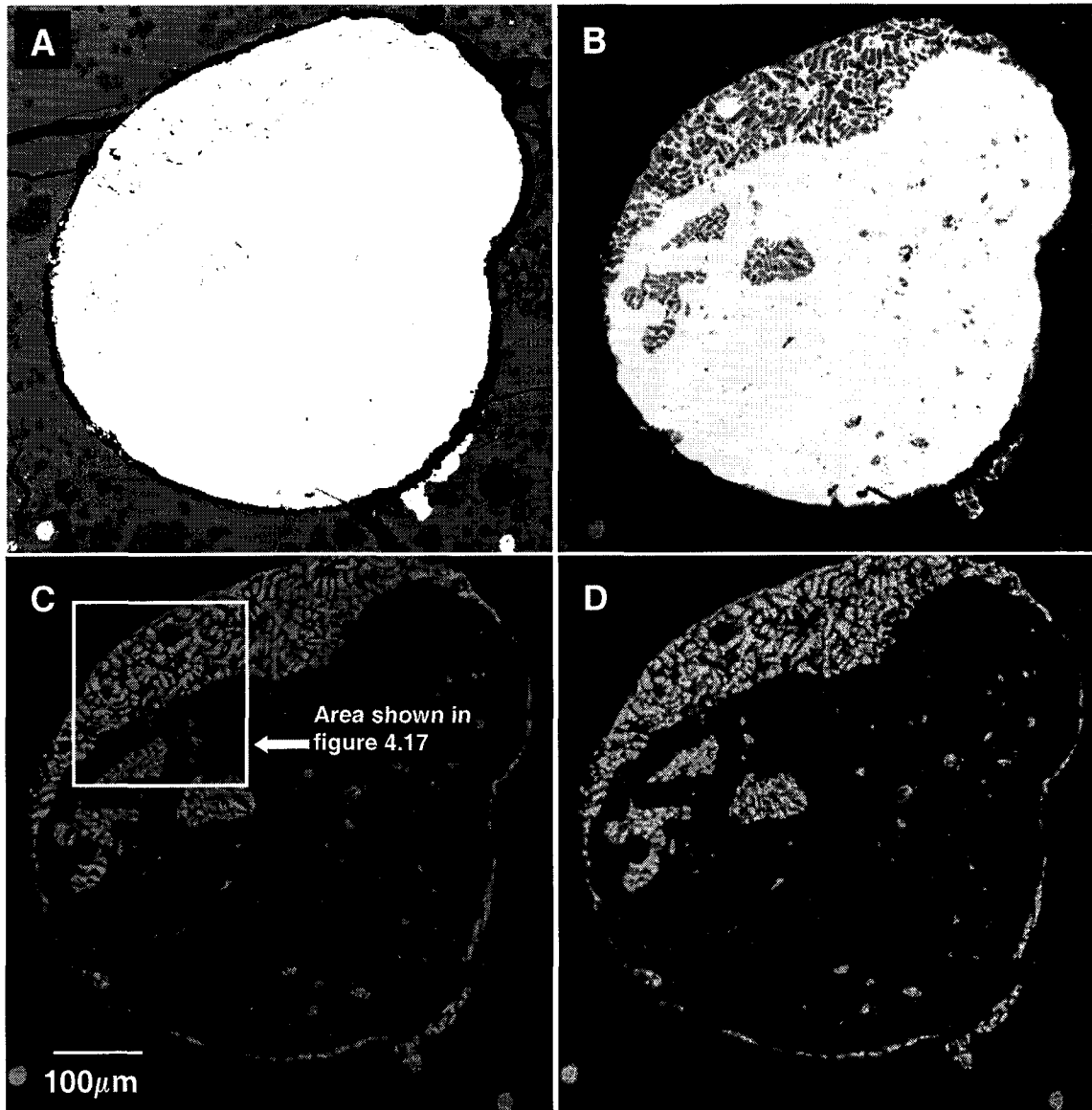
81

Figure 4.18. BSE images and X-ray maps for a large bleb of S, Fe, Pd, Ir, Pt, and Au, exposed in run 59.

A: BSE image of the bleb as seen with brightness and contrast optimized for observation of silicate phases. Olivine crystals and surrounding glass are easily recognized around the bleb.

B: BSE image optimized to show the internal texture of the bleb.

C: Fe X-ray map showing three distinct domains: an Fe-rich domain surrounding the bleb and in some isolated areas inside, and a Fe-poor "core" containing patches of intermediate Fe concentrations. Additional X-ray maps of the enclosed area are shown in Figure 4.19.

D: S X-ray map showing that the "core" domains are S-poor and the perimeter is S-rich, but composed of two separate phases.
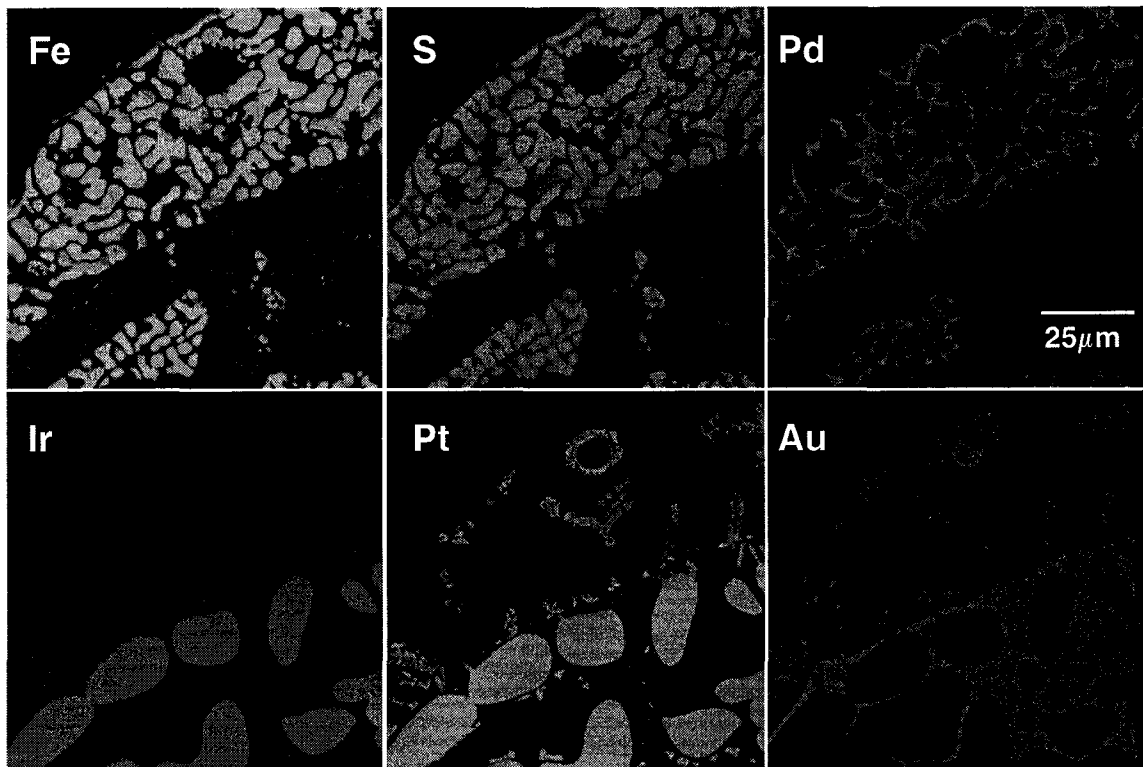
82

Figure 4.19. X-ray maps for Fe, S, Pd, Ir, Pt, and Au for the area enclosed in Figure
4.18 C. The relative concentrations of these elements define four distinct domains. The
top three pictures show that two of these domains are S-rich, most of the sulfur
forming a Fe-S phase while the rest of the sulfur forms a Pd-S phase. The intergrowth
observed is likely a quench effect, and these two phases were probably a single
immiscible liquid at the run conditions. The two other domains are best recognized in
the lower three pictures. One of them shows a "boudinage" texture and is composed of
Pt, Ir, and Fe, with small amounts of gold and no Pd or S. The fourth domain is Au-
rich and contains only small amounts of Pt, Ir and Pd, and appears to have a porous
texture.

83

The Au-rich phase incorporates significant amounts of Pd (7%), Pt (5wt%), and Fe (3%) very small amounts of S (2300 ppm) and behaves in the same way as the PdS phase with respect to Ir, with no measurable amounts of this refractory metal.

The Pt-Ir rich phase is a remnant of the $Pt_{80}Ir_{20}$ wire added as starting material, and equilibrated with the charge, incorporating a significant amount of Fe as expected for alloys under reduced conditions (Borisov and Palme, 2000) (compared to the almost inert behavior of the $Pt_{80}Ir_{20}$ alloy in sulfate-saturated run 52). This phase contained significant amounts of Au and Pd (9.3 and ~3 ppm, respectively) but negligible amounts of sulfur (200 ppm)

An additional phase, best seen in the Pt X-ray map in Figure 4.19 as dendrites growing from the Pt-Ir-Fe alloy into the sulfide rim, contains more Au and less Ir than the Pt-Ir-Fe alloy at the core of the bleb. Its relationship with the other phases described is difficult to assess. The dendritic nature of this phase, radiating from the S-poor core of the bleb, indicates that it was not part of the sulfide liquid that segregated the Fe-S and Fe-Pd phases.

The textures observed in Figures 4.18 and 4.19 and the composition of the different phases (Table 4.14) indicate that Pt and Ir are more siderophile than Au and Pd, and that Pd is the most chalcophile of the four elements analyzed. This behavior is similar to the behavior of the HSE in lherzolites and harzburgites from Pyrenean orogenic massif (Lorand et al. 1999). The implications for the behavior of the HSE in natural systems are discussed in section 5.5.1.

## 4.6. Insight from unequilibrated experiments

Because they are unequilibrated, experiments 39 and 40 provide information about the kinetics of processes relevant to this work. Experiment 39 was prepared from mixtures of $FeSO_4$ and low-Fe-glass, and experiment 40 from mixtures of $CaSO_4$ and low-Ca-glass; thus, they are compositionally identical to runs 30Fe and 30Ca. The charges for experiments 39 and 40 were loaded in graphite-lined Pt capsules and run at 1.2 GPa and 1315 °C for only 1 hour, rather than the 6 hours that 30Fe and 30Ca were run. No HSE were added to the charge, because the only purpose of these two runs was to help constrain the minimum time needed to reduce all sulfate to form sulfide in experiments using sulfate as starting material and run in graphite capsules.

The results showed that although sulfides were present as run products, they occurred only towards the perimeter of the capsule, whereas sulfates were present in the central portions, indicating that the experiment was not in equilibrium (Figure 4.20). Data from these experiments provide insight on kinetic aspects of this study. First, EDS analyses of the sulfate blebs showed that they were Ca-rich, which indicates that Fe-Ca exchange between the glass and the sulfates occurs within one hour. Glass analyses corroborate this: CaO concentrations, when measured beyond 150 $\mu$m from the capsule walls, were $11.9 \pm 0.2$ wt. % (n = 6) and $12.2 \pm 0.5$ wt. % (n = 9) for runs 39 and 40, respectively. FeO concentrations (on the same spots) were $6.3 \pm 0.3$ and $6.0 \pm 0.2$ wt. %, respectively. Figure 4.21 shows measurements of S concentrations as a function of the distance to the graphite capsule walls for these two experiments. The sulfur concentrations in both glasses were significantly higher towards the center of the capsule and of the same order of magnitude as the sulfur concentration of experiments run for longer times and equilibrated with sulfate. In contrast, the sulfur concentrations towards the margin of the capsules were significantly lower and in the range measured for experiments saturated with sulfide. These observations further demonstrate that the experiments presented in the previous sections reached oxidation-reduction equilibrium, and emphasize the role of graphite in the reduction of the system and in the saturation of sulfide blebs.
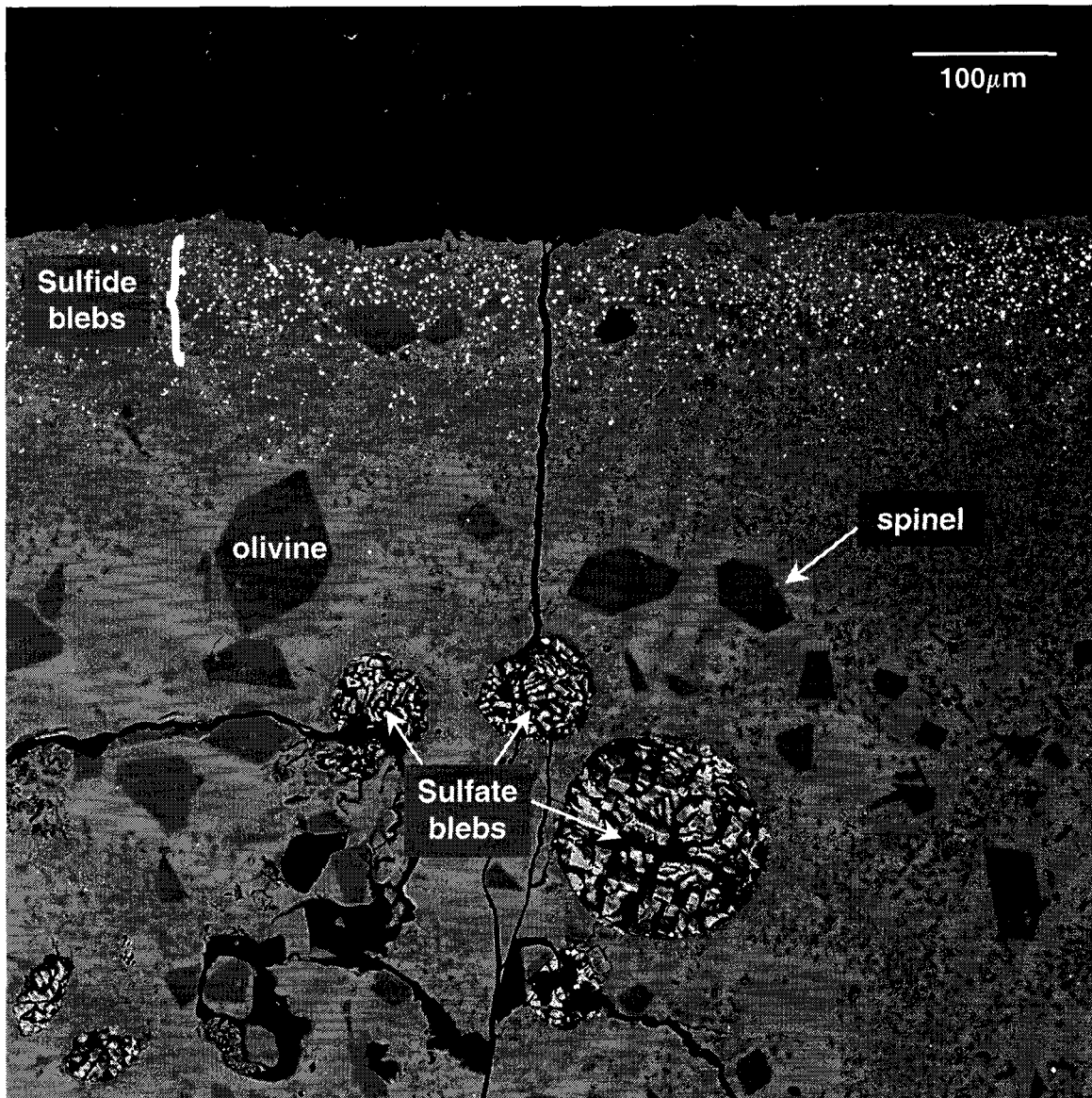
Figure 4.20. Detail of run 39, produced from $FeSO_4$ and low-Fe-glass. The black margin at the top of the picture is the wall of the graphite capsule. Light grey matrix is the quenched glass. Relatively large olivine crystals and very small pyroxene and spinel crystals are dispersed throughout the charge. Large sulfate blebs are located towards the center of the capsule whereas small sulfide blebs (in white) are distributed in a narrow band along the capsule wall. Two spinel crystals half-embedded in an olivine crystal are indicated. The rough texture of the sulfate blebs is due to partial dissolution during sample preparation.

86
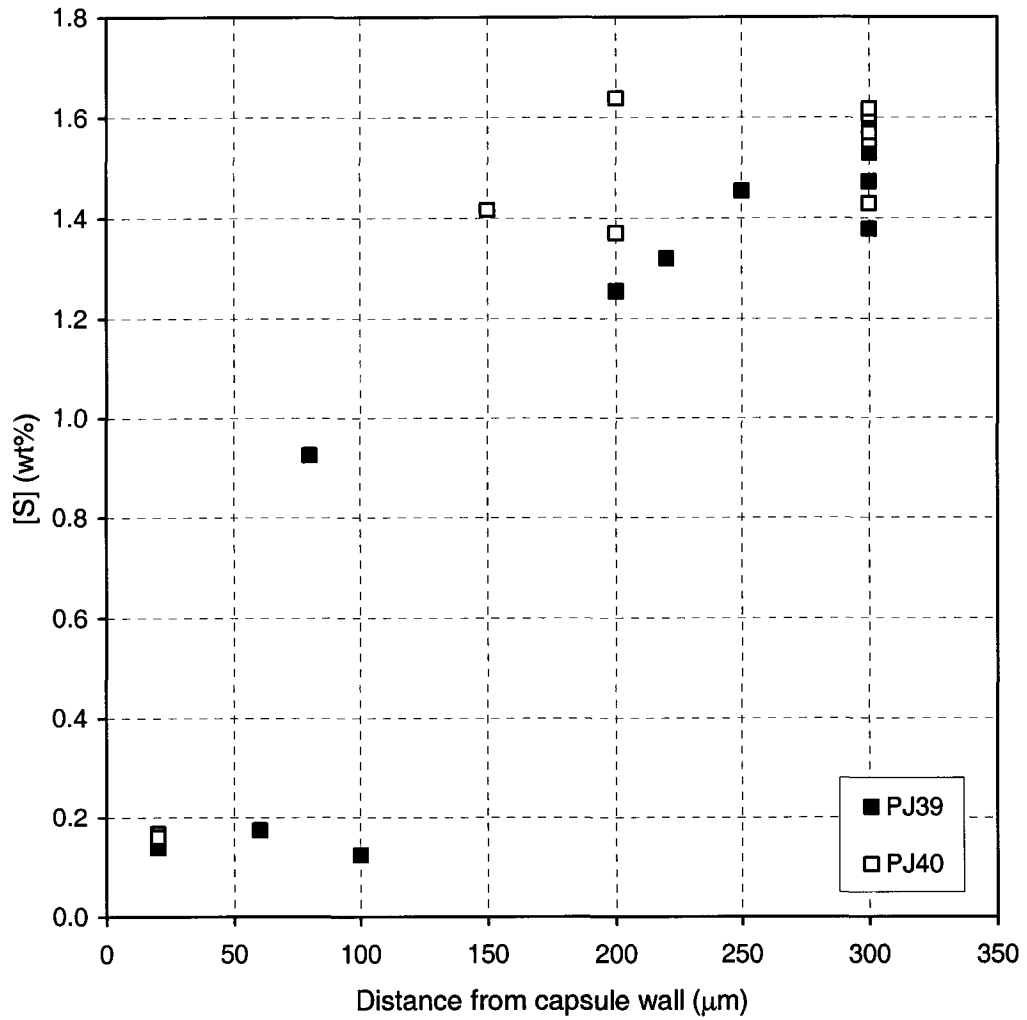
Figure 4.21. Spot analyses of sulfur concentration in the glass against distance from the graphite capsule walls in runs 39 and 40. With the exception of one analysis, the data cluster in two fields. Close to the capsule wall (within 100 $\mu$m) and in the area in which sulfide blebs are present (Figure 4.20) sulfur concentration in the glass is below 0.2 wt.%. Towards the center of the capsule, beyond 150 $\mu$m from the capsule walls sulfur concentration in the glass is above 1.2 wt.% and up to 1.6 wt.%.

# 5. Discussion

In this chapter, the chemical equilibria affecting the experimental system are evaluated with a focus on the factors affecting the oxidation state of the system and the oxidation of sulfides. Available models for sulfur speciation as a function of oxidation state are evaluated and discussed, and the data on sulfur speciation from this and other work are used to derive a new, simpler empirical equation for the dependence of sulfur speciation on oxidation state for basaltic magmas. The equation derived for sulfur speciation is combined with the solubility data obtained in this work and the experimental constraints from the work of Carroll and Rutherford (1985, 1987) to create three possible models for the change in the solubility of sulfur in the melt with increasing oxidation state. These models are then used to estimate the minimum degree of partial melting required to produce sulfur-undersaturated basaltic melts.

Finally, the implications of the findings of this work are discussed for the behavior of the HSE in igneous processes and the fractionation of Pd and Au (more chalcophile) from the rest of the HSE (more siderophile). The role of sulfide elimination by oxidation in supra-subduction zones for the Au enrichment in magmas related to porphyry and epithermal deposits is analyzed. For orthomagmatic deposits, evidence is present to support a model in which reduction of a relatively oxidized magma is the trigger for sulfide precipitation and a key element in the generation of these deposits. To conclude, the contribution of this work to the understanding of the processes that lead to high sulfur degassing in some arc volcanoes are discussed.

## 5.1. Chemical equilibria

Most of the reactions presented here have been discussed previously by many authors. They are presented as a review and to provide a context in which to discuss the results of this work. The key reactions that control the oxidation state of the system are linked to those relating sulfides and sulfate phases and analyzed in the context of sulfide oxidation.

88

The ferric-ferrous equilibria relating the fayalite-magnetite-quartz oxygen buffer to a system containing olivine-spinel-orthopyroxene are presented and used subsequently as an analog to discuss sulfide-sulfate equilibria and some misconceptions that arise from the use of a theoretical "sulfide-sulfate" buffer. The important effect of carbon (graphite) stability on oxidation state is analyzed, as well as the role of water in closed, nominally anhydrous systems.

## 5.1.1. Oxygen fugacity

Oxygen fugacity, as a thermodynamic variable "is a parameter that indicates the oxidation state of a system, much like a thermometer indicates the temperature of a system" (Anderson and Crerar, 1993, p. 495). It is also related to the chemical potential of oxygen in a system. As a thermodynamic component, it does not necessarily have a physical meaning (i.e., only in very few cases $O_2$ is present in the system as a chemical species). For a closed system and at given temperature and pressure conditions, the oxidation state is determined by the bulk composition of the system. One way to translate oxygen fugacity (as a measure of oxidation state) to physical entities is to consider it as the capacity of a system to form oxygenated compounds (e.g., FeO from metallic Fe).

For the system studied here (and their natural analogs), Fe, S and C are the only major elements that exist in multiple oxidation states ($Fe^{2+}$, $Fe^{3+}$; $S^{2-}$, $S^{6+}$; $C^0$, $C^{2+}$, $C^{4+}$). All other major elements (Si, Al, Mg, Ca, Na, K, and Ti) have fixed oxidation states (valence). Trace elements such as V, Eu, and Ce respond to changes in oxidation state, and exist with several valences. They are useful indicators of oxidation state but given their small concentrations in natural systems and their partitioning as trace elements into mineral phases, they respond to, rather than affect, the oxidation state. Thus, oxygen fugacity is controlled by multiple equilibria dominated by three oxidation reactions:

$$4FeO + O_2 = 2Fe_2O_3 \tag{5.1}$$
$$S^{2-} + 2O_2 = SO_4^{2-} \tag{5.2}$$
$$C + O_2 = CO_2 \tag{5.3}$$

89
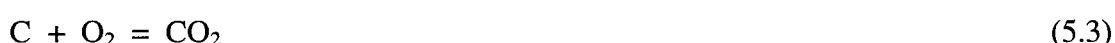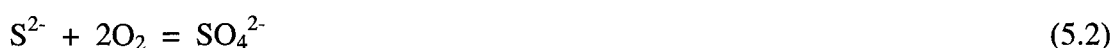
Even though $O_2$ in these reactions is a theoretical thermodynamic component with no necessary identity as an equivalent chemical species, it is legitimate to inquire for a "source" of $O_2$ especially if we are dealing with a closed system. One possible mechanism simply involves changes in the polymerization of the melt:
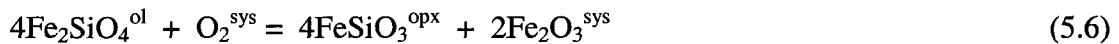
$$2SiO_4^{4-} = 2SiO_3^{2-} + 2O^{2-} \tag{5.4}$$

which implies a change from isolated silica tetrahedra to a single-chain polymer in this case (although the same exercise can be done for any set of more and less polymerized SiO units).

### 5.1.2. Fe-based equilibria

An equivalent of equation 5.4 can be derived using Fe (for purpose of subsequent analysis and to eliminate charged components) and related to components of two possible phases in the systems of interest:

$$Fe_2SiO_4^{ol} = FeSiO_3^{opx} + FeO^{sys} \tag{5.5}$$

and combining equations 5.1 and 5.5:

$$4Fe_2SiO_4^{ol} + O_2^{sys} = 4FeSiO_3^{opx} + 2Fe_2O_3^{sys} \tag{5.6}$$

which now relates $O_2$ to the equilibria between the fayalite component in olivine and the ferrosilite component in orthopyroxene.

The hematite component in equation 5.6 can be related to the magnetite component in spinel by the reaction:
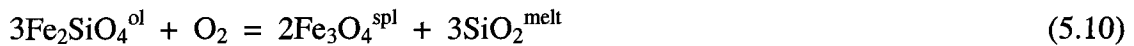
$$6Fe_2O_3^{sys} = 4Fe_3O_4^{mt} + O_2^{sys} \tag{5.7}$$

90

which, when combined with 5.6, provides the equilibrium with which the oxidation state of the experiments is estimated:

$$6Fe_2SiO_4{}^{ol} + O_2{}^{sys} = 6FeSiO_3{}^{opx} + 2Fe_3O_4{}^{spl} \qquad (5.8)$$
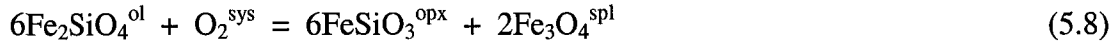
Furthermore, the ferrosilite component in orthopyroxene is by itself an indicator of the chemical potential of silica in the melt:

$$2FeSiO_3{}^{opx} = Fe_2SiO_4{}^{ol} + SiO_2{}^{melt} \qquad (5.9)$$

which substituted in (5.8) gives:

$$3Fe_2SiO_4{}^{ol} + O_2 = 2Fe_3O_4{}^{spl} + 3SiO_2{}^{melt} \qquad (5.10)$$
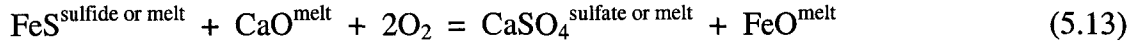
When the pure crystalline phases (fayalite, magnetite) and quartz (instead of $SiO_2{}^{melt}$) are used, this equation defines the FMQ buffer, which provides a convenient reference to compare the oxidation state of different systems. Expressing $fO_2$ relative to FMQ has the advantage of removing much of the temperature dependence inherent in absolute values of $fO_2$, because the slopes of oxidation-reduction reactions in T-$fO_2$ space tend to be similar. Otherwise, equation 5.10 shows that the four components involved are related by the equilibrium constant of this reaction, and that the compositions of the phases (olivine, spinel, melt) are interdependent and a function of oxygen fugacity.

### 5.1.3. Sulfide-sulfate equilibria

An equation involving sulfide-sulfate equilibria expressed in terms analogous to phases present in the experiments (and in natural systems) can be obtained by eliminating the ionic components in equation 5.2 using:
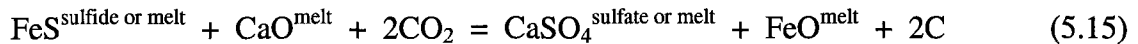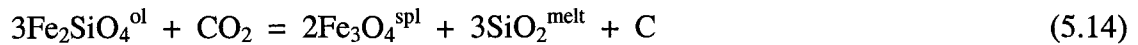
91

$$S^{2-} + FeO = FeS + O^{2-} \tag{5.11}$$

$$SO_2^{2-} + CaO + O_2 = CaSO_4 + O^{2-} \tag{5.12}$$

which yields:

$$FeS^{sulfide\ or\ melt} + CaO^{melt} + 2O_2 = CaSO_4^{sulfate\ or\ melt} + FeO^{melt} \tag{5.13}$$

and relates the FeS component in sulfide (or melt), the CaSO$_4$ component in sulfate (or melt) and the FeO and CaO components in a melt. The differences observed in melt composition in oxidized versus reduced paired experiments with identical bulk composition (52 and 53, 58 and 59) are consistent with this equilibrium. Specifically, the oxidized runs (52 and 58) contained higher FeO and lower CaO in the melt than their reduced, sulfide-bearing counterparts (53 and 59) regardless of the starting material being sulfate (pair 52-53) or sulfide (pair 58-59).

### 5.1.4. Effect of carbon

In experiments performed in graphite capsules, carbon controls the oxidation state of the system by the reaction shown in equation 5.3, which can be combined with equation 5.10 and 5.13 to understand the effect of graphite of the ferric-ferrous and sulfide-sulfate equilibria:

$$3Fe_2SiO_4^{ol} + CO_2 = 2Fe_3O_4^{spl} + 3SiO_2^{melt} + C \tag{5.14}$$

$$FeS^{sulfide\ or\ melt} + CaO^{melt} + 2CO_2 = CaSO_4^{sulfate\ or\ melt} + FeO^{melt} + 2C \tag{5.15}$$

with CO$_2$ dissolving in the melt in an anhydrous (or fluid undersaturated) system and partitioned between the melt and a hydrous phase in a gas-saturated system. As long as elemental carbon (graphite capsule, or graphite powder in the experiments) is present, reaction (5.14) is driven to the left, decreasing the magnetite component in spinel at the expense of dissolving CO$_2$ in the melt (or stabilizing a CO$_2$-rich fluid), and constraining the oxidation state to reducing conditions. Reaction (5.15) follows the same pattern and

92

sulfate is consumed to form sulfide as seen in the experiments. In run 34C, in which small amounts of powdered graphite was added, carbon was likely completely dissolved as $CO_2$ in the melt, probably accompanied by some FeS dissolved in the melt but not enough to saturate sulfide.

### 5.1.5. Effect of water

Although most experiments were nominally anhydrous (except runs 58 and 59, which were water undersaturated), water is a key component in metasomatism and its role needs to be evaluated. The effects of water are discussed here for a closed system, in analogy with the treatment of the other components that affect the oxidation state of the system (C, S, and Fe). The basic reaction:

$$2H_2 + O_2 = 2H_2O \qquad (5.16)$$

shows a key element in the potential of water as an "oxygen donor" to the system: generation of molecular hydrogen. In some experimental configurations, water is an oxidizing agent only because the system is not closed to hydrogen and osmotic equilibration of hydrogen through the wall capsules can be used to increase or decrease the oxygen fugacity by affecting the equilibrium in 5.16. In closed systems in general, water should not be expected to play a significant role in oxidation processes being subordinate to the reactions shown in equations 5.1 to 5.3 written for a fluid phase (e.g., $H_2S$, and $CH_4$ instead of S and C). In nature, the role of water in oxidation-reduction processes is largely dependent on the permeability of the system to hydrogen. For example, hydrous metasomatism, followed by hydrogen loss (which drives reaction 5.16 to the left), would be effective oxidation mechanism.

### 5.1.6. Summary

Several key aspects seen in the experiments, related to the chemical equilibria discussed above, and with implications to natural systems can be summarized in four points:

- As long as carbon is present in the assemblage, the oxidation state of the system is controlled by carbon equilibrium at or below the CCO buffer (defined by equation 5.3). Only when graphite is eliminated (for example by dissolution into a melt, or by reaction with oxidized iron to form $CO_2$) can the oxidation state of the system increase above the CCO buffer.
- In a carbon-free system, and because Fe is a major component in silicate systems, the oxidation state is controlled by ferric-ferrous equilibria among Fe-bearing phases.
- Addition of sulfur as sulfate or carbon as carbonate would contribute to increasing the oxidation state of the system, but would normally be subordinate to the presence of graphite and the ferric-ferrous equilibria.
- Addition of water by itself cannot affect the oxidation state of the system unless the system is open, such that hydrogen fugacity can be modified (e.g., by diffusion in and out of the systems as $H_2$ or as $CH_4$ and $H_2S$ removed in a volatile phase).

Regarding the first point, note that in experiments 54 and 55, around 1:1 C:S (by wt) in the bulk composition was enough to keep graphite in the system and reduce the sulfate starting material to sulfide. In run 34C, C:S is 1:0.74, graphite was dissolved and sulfate was the only sulfur-bearing phase present. This simplistic analysis does not consider differences in the bulk $Fe^{3+}/\Sigma Fe$ among the experiments, but nonetheless opens the possibility of studying the sulfide-sulfate equilibria by fixing the bulk $Fe^{3+}/\Sigma Fe$ in the charge and altering the C-S ratios.

An additional point to address is how crystallization and fractionation may affect the oxidation state of a system. Carmichael (1991) discussed the effect of olivine, phlogopite and augite crystallization on the oxidation state of a melt. He argued that because ferric

94

iron is not incorporated in the olivine structure, crystallization of olivine would increase the proportion of ferric iron in the melt, whereas crystallization of phlogopite or augite (that can incorporate ferric iron in their structure) would increase the proportion of ferrous iron in the melt, dereby making it more reduced. Thus, crystallization of mineral phases would control the oxidation state of the system. However, this cause-effect mechanism may not be applicable to complex systems crystallizing multiple phases, some of which can incorporate both ferric and ferrous iron (e.g., clinopyroxene, spinel) in which case the opposite occurs: the oxidation state of the system dictates the composition ($Fe^{3+}/\Sigma Fe$) of crystallizing phases. Luth and Canil (1993), for example, found significant amounts of $Fe^{3+}/\Sigma Fe$ (ranging from 0.12 to 0.24) in clinopyroxenes from spinel lherzolites from British Columbia, and predicted values up to 0.45 $Fe^{3+}/\Sigma Fe$ in clinopyroxenes for similar assemblages at FMQ. Figure 5.1 shows the correlation of $Fe^{3+}/\Sigma Fe$ in the spinel against oxidation state from the experiments in this work. Figure 5.2 illustrates the change in $Fe^{3+}/\Sigma Fe$ in the melt (calculated using the method of Kilinc et al., 1983) as a function of oxidation state for the same experiments shown in Figure 5.1. In essence, the higher $Fe^{3+}/\Sigma Fe$ of oxidized melts would be reflected as higher $Fe^{3+}/\Sigma Fe$ in those minerals that can incorporate both ferric and ferrous iron. However, saturation of minerals containing ferric iron does not necessarily cause a decrease in the ferric iron content in the melt as suggested by Carmichael (1991).
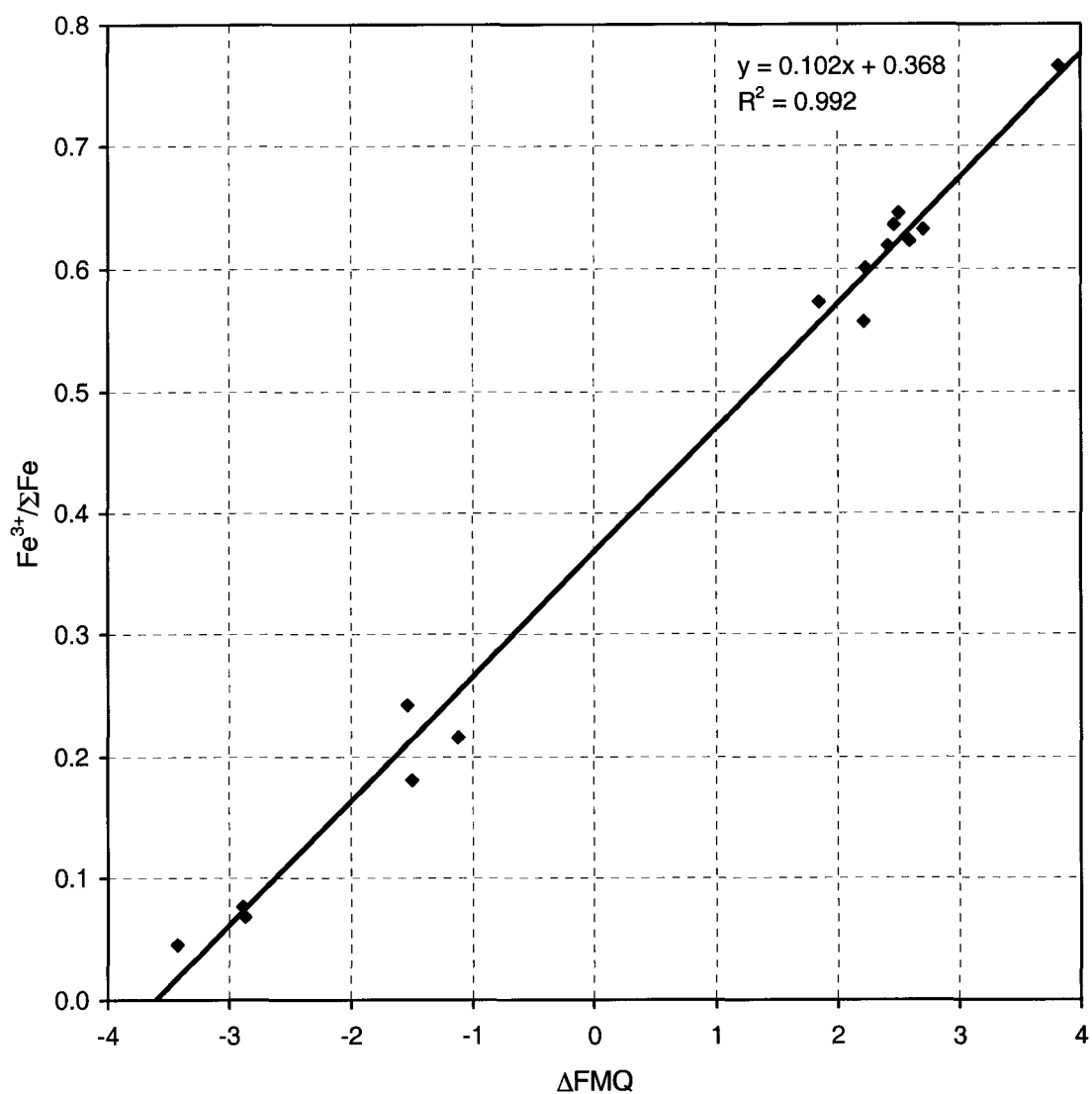
Figure 5.1. $Fe^{3+}/\Sigma Fe$ in spinel against oxygen fugacity, determined using the oxide-silicate equilibria, for the experiments in this study.
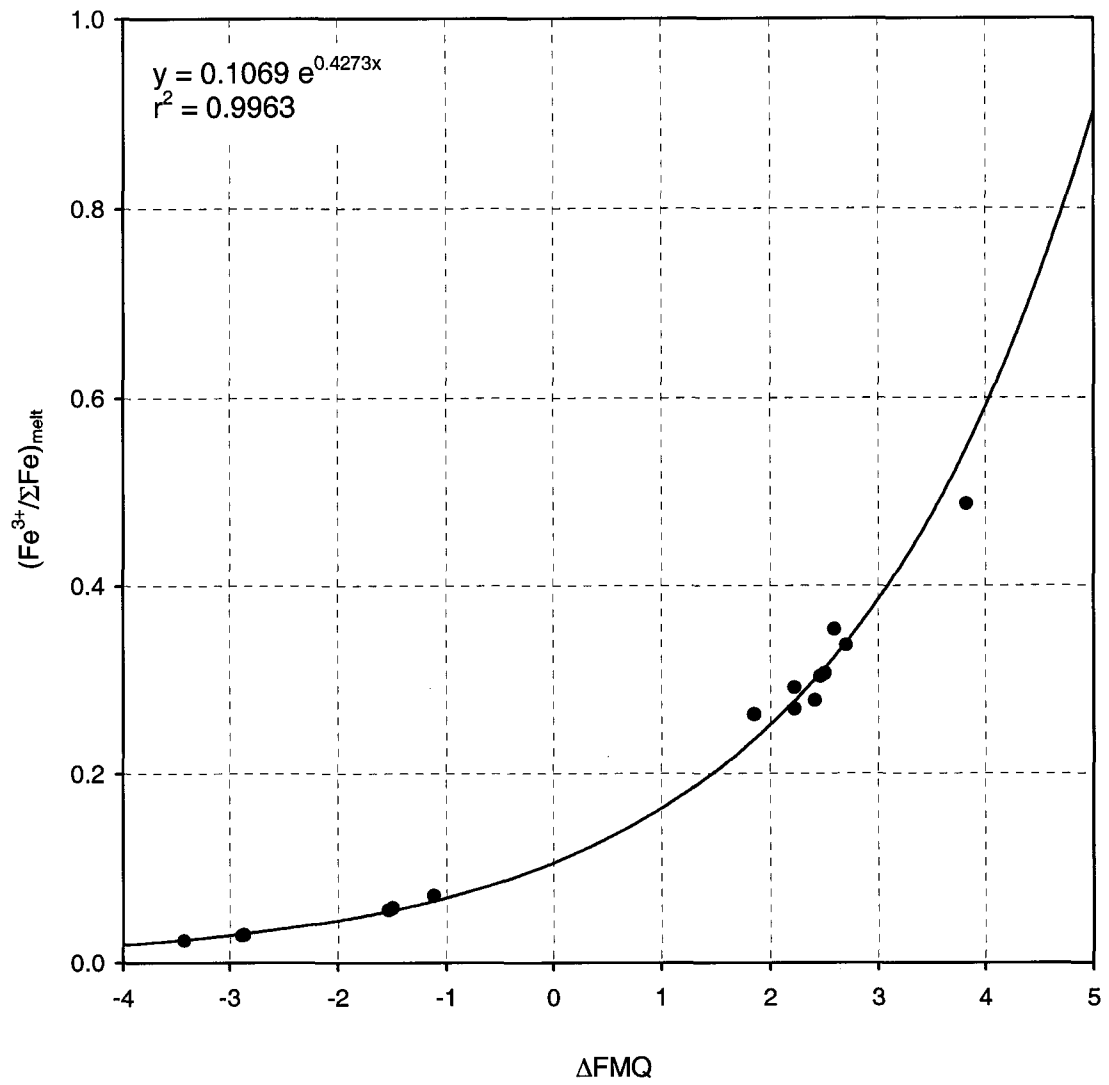
96

Figure 5.2. $Fe^{3+}/\Sigma Fe$ in the melt against oxidation state for the experiments in this study.

## 5.2. Speciation of sulfur

The eruption of El Chichón volcano (Mexico) in early 1982 produced anhydrite-bearing pumices and brought attention to the stability of sulfate-bearing phases in volcanic environments (Luhr et al., 1984). The Mt. Pinatubo eruption in 1991 released more than 17 Mt of $SO_2$ into the atmosphere (Gerlach et al., 1996) and emphasized the need to understand the occurrence of anhydrite and other sulfate-bearing phases in magmatic systems for both their relevance to sulfur-rich volcanic gases and their impact on climate, as well as for their implications for the stability of S-bearing phases in igneous systems. Other examples of anhydrite occurrence in volcanic rocks predate the El Chichón eruption: for example, Arculus et al. (1983) described anhydrite-bearing andesites from the Mount Lamington eruption in 1951 that were previously documented by Taylor (1958, cited in Arculus et al., 1983). Determination of whether anhydrite is a common magmatic phase in other oxidized volcanic environments is hampered by the rapid weathering of this phase. Luhr et al. (1984) documented the lack of anhydrite in rocks collected after one rain season in the El Chichón volcano and Arculus et al. (1983) could only confirm the presence of anhydrite in the andesites from Mount Lamington using the original samples collected by Taylor (1958).

Chappell and White (1968) used the shift in the wavelength ($\lambda$) of the sulfur $K\alpha$ characteristic X-ray ($SK\alpha$) to determine that sulfur in scapolites from the Laacher See volcanic rocks in Germany was present as sulfate. Carroll and Rutherford (1988) showed that the speciation of sulfur in a silicate melt changes from sulfide-dominated at FMQ-2 to sulfate-dominated at FMQ+2 for trachyandesites and dacites at pressures and temperatures similar to those at which the El Chichón magmas were generated (~200 MPa and 1000 °C). Carroll and Rutherford (1988) refined the use of the shift in the wavelength of the $K\alpha$ peak for sulfur ($\Delta\lambda(SK\alpha)$) as a way to estimate sulfur speciation and introduced most of the terminology used in subsequent work (Wallace and Carmichael, 1992, 1994; Nilsson and Peach, 1993; Metrich and Clocchiatti, 1996; Winther et al., 1998; Matthews et al., 1999; Gurenko and Schmincke, 1998, 2000; this study).

98

The shift in the wavelength of sulfur $K\alpha$ radiation in a sample is typically measured relative to a sulfide reference (FeS, FeS$_2$, PbS, or ZnS):

$$\Delta\lambda(SK\alpha)_{sample} = \lambda(SK\alpha)_{sulfide\ reference} - \lambda(SK\alpha)_{sample} \qquad (5.17)$$

The maximum shift in the wavelength ($\Delta\lambda(SK\alpha) \approx 0.3$ pm) is obtained for sulfates (CaSO$_4$, BaSO$_4$). The sulfate mole fraction of a sample ($X(S^{6+})$) can be estimated assuming that sulfur is dominantly present as a combination of sulfide and sulfate species and that $\Delta\lambda(SK\alpha)$ is proportional to the mole fraction of sulfate:

$$X(S^{6+}) = \Delta\lambda(SK\alpha)_{sample}/\Delta\lambda(SK\alpha)_{anhydrite} \qquad (5.18)$$

Three important premises for the validity of equation 5.18 are:
- that sulfur is present in the glasses only as sulfide or sulfate species
- that the observed shifts in the $SK\alpha$ peaks are only a result of the relative proportion of these two species in the sample, and
- that there is a linear relationship between wavelength shift and proportions of the two species.

With regard to the first premise, Winther et al. (1998) suggested that other sulfur species such as $S_2^-$ and $S_3^-$ could be present in silicate melts, and that in those cases the estimated $X(S^{6+})$ values should be considered "mole fraction sulfate equivalents". Paris et al. (2001) used X-ray absorption near-edge spectroscopy (XANES) of the sulfur K-edge to investigate sulfur speciation in one natural and four synthetic glasses and concluded that no species, other than $S^{2-}$ and $S^{6+}$, were present. They extrapolated these results to conclude that these are the only two sulfur species present in magmatic systems. However, the four synthetic samples analyzed by Paris et al. (2001) were equilibrated at high oxidation states (above FMQ+4) and thus only sulfate species should be expected for them. Their results from analyses on the natural sample (a back-arc basalt) show that for that sample sulfur is present as $S^{2-}$ and $S^{6+}$, but it is not clear that this is generalizable for all cases.

Shifts in $K\alpha$ can also be related to differences in bonding. Li et al. (1995) measured sulfur K-edge XANES for 23 sulfides and sulfosalts and found that the wide scattering of

99

the data for sulfides and sulfosalts overlaps the range measured for native sulfur and $FeS_2$ (pyrite and marcasite, for which they estimated sulfur is present as $S_2^{2-}$). Because XANES and shift in $\lambda K\alpha$ obtained by EPMA are based on the same principles (i.e., that electronic configuration affects the difference in energy between orbitals), a scatter in the $\lambda K\alpha$ peak obtained by EPMA should be expected. For example, using the data of Winther et al (1998) and sphalerite as the reference for $X(S^{6+}) = 0$, galena (PbS), arsenopyrite (FeAsS), and pyrite ($FeS_2$) have $X(S^{6+})$ of 0.05, 0.11, and 0.18, respectively. Although the value obtained for pyrite can be explained by sulfur being present as $S_2^{2-}$ ion, the differences observed for galena and arsenopyrite can only be attributed to slight differences in bonding energies unrelated to the oxidation state of sulfur (otherwise $X(S^{6+})$ for galena and arsenopyrite would also be zero).

At high oxidation states, three possibilities exist for the oxidation state of sulfur, two of them being sulfite ($S^{4+}$) and sulfate ($S^{6+}$). Thiosulfate, which is typically written as $S^{2-}S^{6+}O_3^{2-}$ was found to be more consistent with sulfur oxidation as $S^-S^{5+}O_3^{2-}$ by Vairavamurthy et al. (1993) and Li et al. (1995) using XANES. The data obtained from XANES (Li et al., 1995) and EPMA (Winther et al., 1998) for various sulfates show no significant differences in S-edge among sulfates, and very distinctive differences between sulfates, sulfites and the $S^{5+}$ ion in thiosulfates.

All this evidence indicates that the oxidation state of sulfur is quite complex. Although $S^{2-}$ and $S^{6+}$ are clearly the dominant species at the extreme conditions of reduced versus oxidized environments, other species cannot be disregarded, specially for the range of oxidation state in which the transition from sulfide to sulfate speciation occurs.

Regardless of the possible presence of other sulfur species, the use of $X(S^{6+})$ derived from EPMA as "mole fraction sulfate equivalent" provides a framework in which the speciation of sulfur can be measured and compared. Several conclusions can be drawn from the works of Kucha et al. (1989), Vairavamurthy et al. (1993), Li et al. (1995), Winther et al. (1998), Matthews et al. (1999), and Paris et al. (2001):

- Sphalerite and galena (ZnS and PbS) are the best choice of sulfide reference for EPMA estimations of $X(S^{6+})$.

- The $X(S^{6+})_{eq.}$ for native sulfur $(S^0)$ ranges from 0.12 to 0.20-0.25.

- The $X(S^{6+})_{eq.}$ for sulfite $(S^{4+})$, based on sodium sulfite measurements, ranges from 0.68 to 0.79.

- No significant difference is observed in the $\Delta\lambda(SK\alpha)$ among different sulfates $(CaSO_4, BaSO_4,$ or $SrSO_4)$ and any of these could be used as a reference to define $X(S^{6+}) = 1$.

- Sodium thiosulfate $(Na_2S^{2-}S^{6+}O_3,$ or $Na_2S^-S^{5+}O_3$ as suggested by Vairavamurthy et al., 1993), which ideally should yield $X(S^{6+}) = 0.5$, was measured at $X(S^{6+})_{eq.} = 0.38$ (Kucha et al., 1989).

## 5.2.2. Evaluation of current models of sulfur speciation as a function of oxidation state

Based on the data of Carroll and Rutherford (1988), Wallace and Carmichael (1994) derived an expression based on equation 5.2 to describe the sulfur speciation as a function of oxidation state:

$$\log (X(S^{6+})/X(S^{2-})) = a\times\log fO_2 + b/T(K) + c, \qquad (5.19)$$

where $a = 1.02, b = 25410, c = -10,$ and $T(K) =$ temperature in Kelvin.

Wallace and Carmichael (1994) obtained the "a" and "c" coefficients from linear regression of Carroll and Rutherford's (1988) data. The "b" coefficient is the temperature coefficient taken from the Ni-NiO buffer (NNO) of Huebner and Sato (1970), and multiplied by 1.02 (the value of "a"). This assumes that $X(S^{6+})/X(S^{2-})$ has the same T dependency of solid redox buffers, (they chose the temperature coefficient from the NNO buffer because this was their reference buffer).

Equation 5.19 was used by Metrich and Clocchiatti (1996) and Gurenko and Schmincke (1998, 2000) to estimate the oxidation state of magmas from measurements of sulfur speciation. Although Wallace and Carmichael (1994) plotted $X(S^{6+})$ against $\Delta NNO$ based

101

on equation 5.19, this cannot be done directly, because this equation is neither solved for $X(S^{6+})$ nor expressed relative to $\Delta$NNO. Further manipulations and assumption that were not shown in Wallace and Carmichael (1994), Metrich and Clocchiatti (1996), or Gurenko and Schmincke (1998, 2000) are required. What follows is a development of equation 5.19 to derive the appropriate expressions that relate $X(S^{6+})$ to a reference buffer, either NNO or FMQ.

Because Wallace and Carmichael (1994) used the temperature coefficient from the NNO buffer of Huebner and Sato (1970) this buffer will be used as the reference buffer. Using the NNO buffer expression of Huebner and Sato (1970):

$$\log fO_2 \text{ at Ni-NiO (atm)} = \log fO_{2(NNO \pm 0.03)} = 9.36 - 24930/T(K) \quad (5.20)$$

one can define $\Delta NNO_{sample}$ as:

$$\Delta NNO_{sample} = \log fO_{2(sample)} - \log fO_{2(NNO)}$$

therefore:

$$\log fO_{2(sample)} = \Delta NNO_{sample} + \log fO_{2(NNO)}$$

$$\log fO_{2(sample)} = \Delta NNO_{sample} + 9.36 - 24930/T(K)$$

which used in equation 5.19 gives:

$$\log (X(S^{6+})/X(S^{2-})) = 1.02(\Delta NNO_{sample} + 9.36 - 24930/T(K)) + 25410/T(K) - 10$$

$$\log (X(S^{6+})/X(S^{2-})) = 1.02\Delta NNO_{sample} - 18.60/T(K) - 0.45 \quad (5.21)$$

and converted to a natural logarithmic expression:

$$\ln(X(S^{6+})/X(S^{2-})) = 2.35\Delta NNO_{sample} - 42.83/T(K) - 1.04 \quad (5.22)$$

Since the equilibrium used to derive equation 5.21 assumes that $S^{6+}$ and $S^{2-}$ are the only options for the oxidation state of sulfur, we can assume that:

$$X(S^{2-}) = 1 - X(S^{6+}) \quad (5.23)$$

and solve for $X(S^{6+})$:

$$X(S^{6+}) = 1/(1 + \exp(42.83/T(K) + 1.04 - 2.35\Delta NNO)) \quad (5.24)$$

This is a sigmoidal ("S" shaped) function of the form:

$$y = a/(1 + \exp(b - cx))$$

In this case $a = 1$, $b = 42.83/T(K) + 1.04$, and $c = 2.35$. The effect of the term associated with temperature on $X(S^{6+})$ is small and decreases with increasing temperature. A

102

simplified parametrization of equation 5.24 can be obtained using T = 1000 °C, which is a reasonable magmatic temperature. This simplification introduces an error in the calculated $X(S^{6+})$ of less that 0.6% for temperatures between 500 and 1500 as illustrated in Figure 5.3.

The resulting equation:

$$X(S^{6+}) = 1 / (1 + exp(1.08 - 2.35 \times \Delta NNO)) \qquad (5.25)$$

can be rearranged to solve for $\Delta NNO$ :

$$\Delta NNO = 0.98 \times ln(X(S^{6+})/X(S^{2-})) + 0.46 \qquad (5.26)$$

This is the explicit form of the expression presented by Wallace and Carmichael (1994) (equation 5.19) and used by Metrich and Clocchiatti (1996) and Gurenko and Schmincke (1998, 2000) to calculate the oxidation state of primitive melts from determinations of sulfur speciation.

Wallace and Carmichael (1994) did not assign any uncertainties for the coefficients in equation 5.19, nor did Huebner and Sato (1970) report uncertainties for the coefficients in equation 5.20 (although they estimated an uncertainty of 0.03 in the $fO_2$ of the NNO buffer). Therefore, no uncertainty can be assigned to the coefficients in equations 5.25 and 5.26 at this point.

Equations 5.25 and 5.26 can be translated into FMQ units. The difference between FMQ and NNO is pressure and temperature dependent (e.g., NNO = FMQ + 0.70 at 0.1 GPa, 1000 °C; FMQ + 0.50 at 0.5 GPa, 1000 °C; FMQ + 0.25 at 1 GPa, 1000 °C ). As a first approximation, and for general comparison between NNO and FMQ, a conversion factor of $\Delta NNO = \Delta FMQ - 0.70$ will be used. This is the value used by Wallace and Carmichael (1994) to compare their data (in $\Delta NNO$) to the data of Carroll and Rutherford (1988) (in $\Delta FMQ$) and was likely also adopted by Metrich and Clocchiatti (1996) and Gurenko and Schmincke (2000) as inferred from the position of the data from Carroll and Rutherford (1988) in their plots.
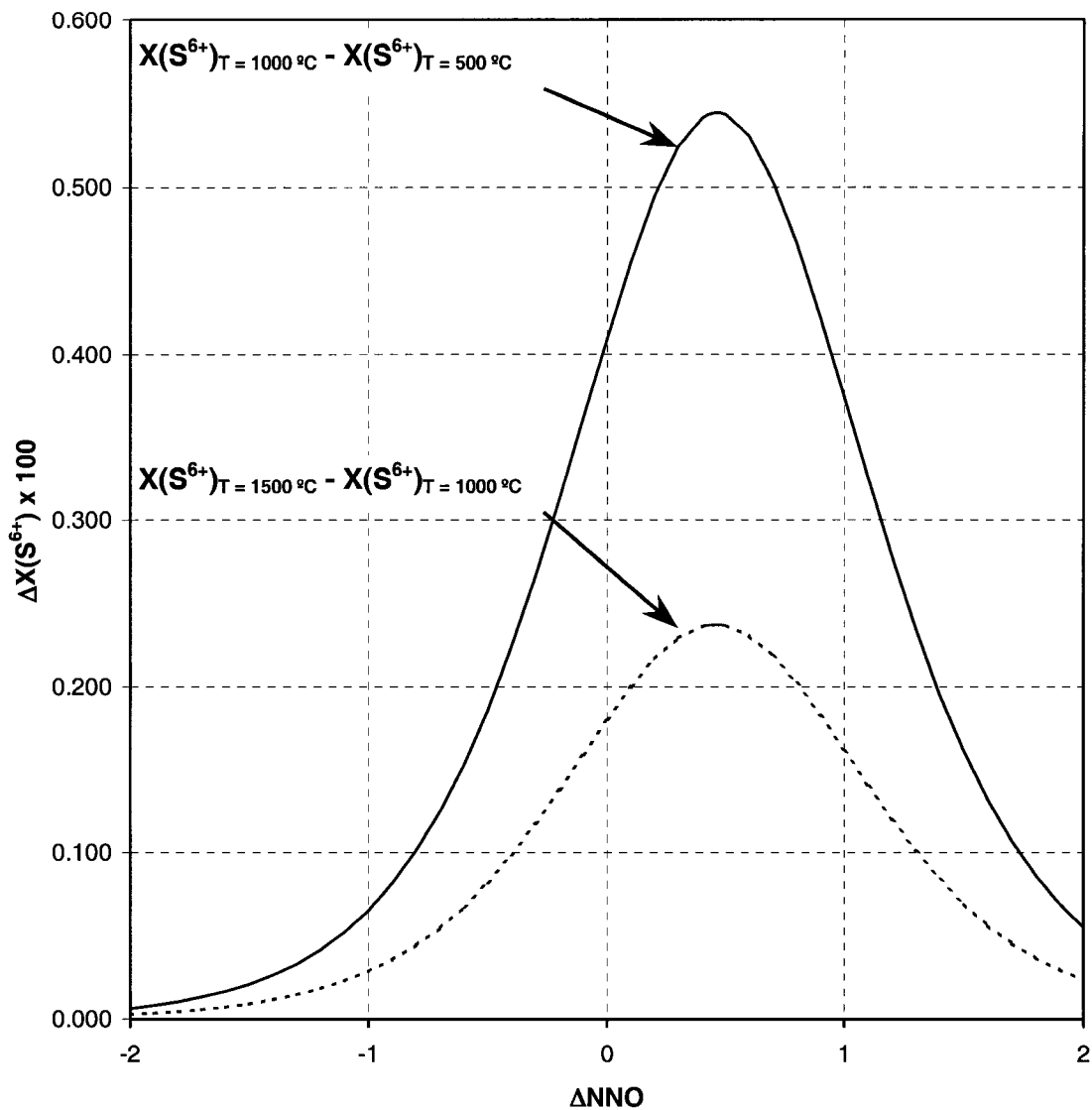
Figure 5.3. Evaluation of the term related to temperature in equation 5.24. The ordinate shows the difference in the calculated $X(S^{6+})$, multiplied by 100, that results from simplifying equation 5.24 using T = 1000 °C. The solid and dashed curves are the difference of the estimated $X(S^{6+})$ using this simplification relative to T = 500 °C and T = 1500 °C respectively. The maximum error in $X(S^{6+})$ obtained by assigning a T = 1000 °C to the T-term in equation 5.24 is less than 0.6% between the temperature range 500 < T < 1500 °C.

Note that although NNO $\approx$ FMQ + 0.7, $\Delta$NNO $\approx$ $\Delta$FMQ - 0.7 because of the definition of the delta notation[1].

Thus, the equations relating sulfur speciation and oxidation state (as $\Delta$FMQ) using Wallace and Carmichael model are:

$$X(S^{6+}) = 1 / (1 + \exp(2.73 - 2.35\Delta FMQ)) \qquad (5.27)$$

$$\Delta FMQ = 0.43 \times \ln(X(S^{6+})/X(S^{2-})) + 1.16 \qquad (5.28)$$

The curve defined by equation 5.27 is shown in Figure 5.4 along with the data from Carroll and Rutherford (1988) and the data from Wallace and Carmichael (1992, 1994). The insert shows the data from Metrich and Clocchiatti (1996) and Gurenko and Schmincke (1998, 2000), which use the model of Wallace and Carmichael (equation 5.27) to estimate oxidation state from estimates of sulfur speciation (and consequently fit the curve perfectly).

Additional data on sulfur speciation with independent estimates of oxidation state is available from the work of Nagashima and Katsura (1973), Katsura and Nagashima (1974), Nilsson and Peach (1993), Matthews et al. (1999), and the present study. The compiled data is shown in Figure 5.5 along with the curve fit of Wallace and Carmichael (1994). The data from Nagashima and Katsura (1973) and Katsura and Nagashima (1974) is consistently shifted to lower oxidation states relative to the rest. The former study used $Na_2O$-$SiO_2$ glass and the latter tholeiite basalts from Hawaii. In both cases experiments were conducted at 1250 °C and 1 atmosphere total pressure. They used $CO_2$-$H_2$-$SO_2$ gas mixtures to control oxygen fugacity and a solid electrolyte cell $((ZrO_2)_{0.85}(CaO)_{0.15})$ to measure it. The deviation of their data seems to result from systematic errors in the estimation of oxidation state because it is consistently shifted by $\sim$ -1.5 log units with respect to the rest of the data, but I was not able to identify any potential source of error.

---

[1] $\Delta$NNO = log$fO_{2(sample)}$ - log$fO_{2(NNO)}$
$\Delta$FMQ = log$fO_{2(sample)}$ - log$fO_{2(FMQ)}$
hence, $\Delta$NNO = $\Delta$FMQ + log$fO_{2(FMQ)}$ - log$fO_{2(NNO)}$
substituting log$fO_{2(NNO)}$ = log$fO_{2(FMQ)}$ + 0.7 above yields: $\Delta$NNO = $\Delta$FMQ - 0.7
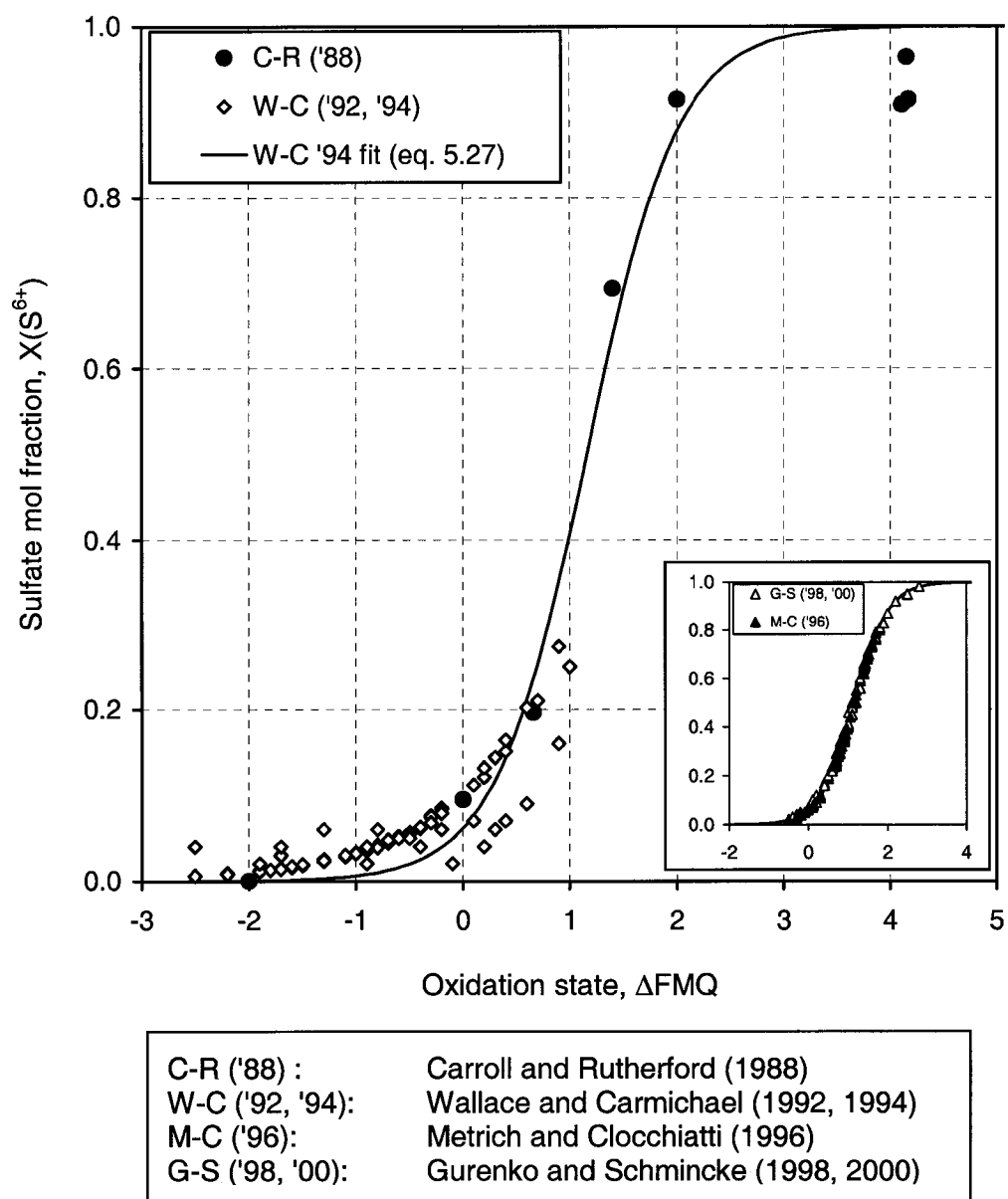
Figure 5.4. Sulfur speciation model of Wallace and Carmichael (1994) based on the data from Carroll and Rutherford (1988).
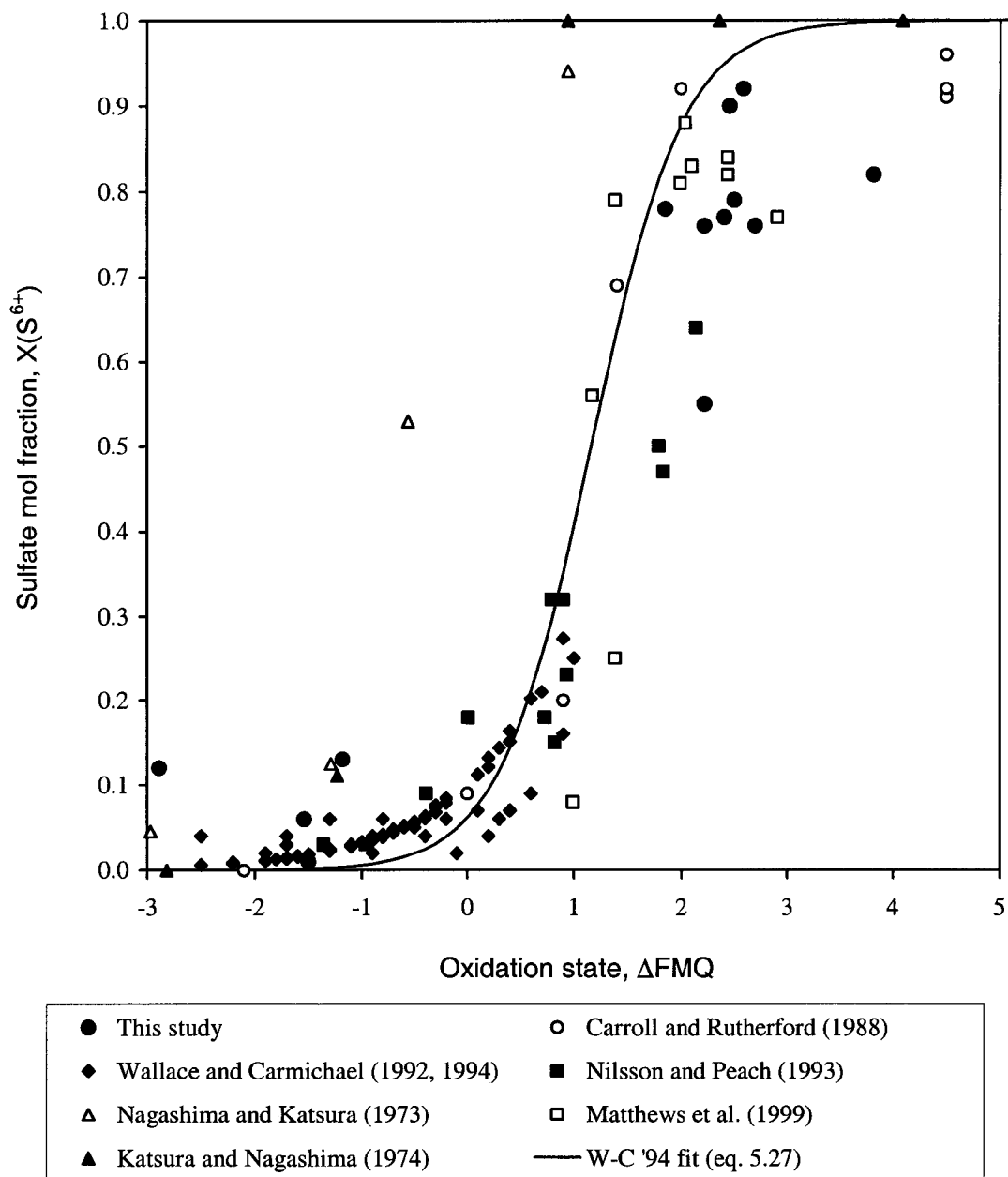
Figure 5.5. Comparison of the sulfur speciation model of Wallace and Carmichael (1994) to all available data on sulfur speciation against oxidation state.

Because of their systematic deviation, the data from Nagashima and Katsura (1973) and Katsura and Nagashima (1974) will not be included in subsequent analysis. However, an observation about their data justifies further discussion. The sulfur speciation trends defined by the results of the two compositions ($Na_2O$-$SiO_2$ glass versus tholeiite basalts) overlap, contrary to how their data are shown by Carroll and Rutherford (1988) and Baker and Rutherford (1996a, 1996b) where the trend defined by the sulfur speciation in the tholeiitic melt was misplotted. This is relevant because Baker and Rutherford (1996a, 1996b) suggested that the apparent shift between the curves could be related to differences in the alkali content of the melts.

The data from Carroll and Rutherford (1988) are from trachyandesites, andesites and dacites (equilibrated experimentally between 100 and 200 MPa and ~1000 °C), whereas the rest of the data correspond mostly to basalts and basaltic andesites. Few data are available for oxidation states $\geq$FMQ+1. The data from Nilsson and Peach (1993) are from basalts and basaltic andesites from the Lau Basin (southwest Pacific). The data from Matthews et al. (1999) are from seven basaltic andesites and three andesites from the Lascar volcano (Chile) and Cerro Overo, a basaltic maar crater located in the vicinity of Lascar. The data provided in this dissertation are the only experimental data on sulfur speciation in basaltic melts available.

Matthews et al. (1999) recognized that their data and the data from Nilsson and Peach (1993) were not well fitted by the model of Wallace and Carmichael (1994), and derived an empirical calibration with a fifth-order polynomial fit:

$$\Delta FMQ = a(X(S^{6+}))^5 + b(X(S^{6+}))^4 + c(X(S^{6+}))^3 + d(X(S^{6+}))^2 + eX(S^{6+}) + f \qquad (5.29)$$

where a = 227.55; b = -532.83; c = 464.77; d = -186.88; e = 36.563, and f = -1.8793.

This polynomial fit (shown in Figure 5.6) accounts for the shift to higher oxidation states of the $X(S^{6+})$ data relative to the model of Wallace and Carmichael (1994) but the changes in slope in this fit (specially between FMQ+1 and FMQ+2) are an artifact of the polynomial fit.
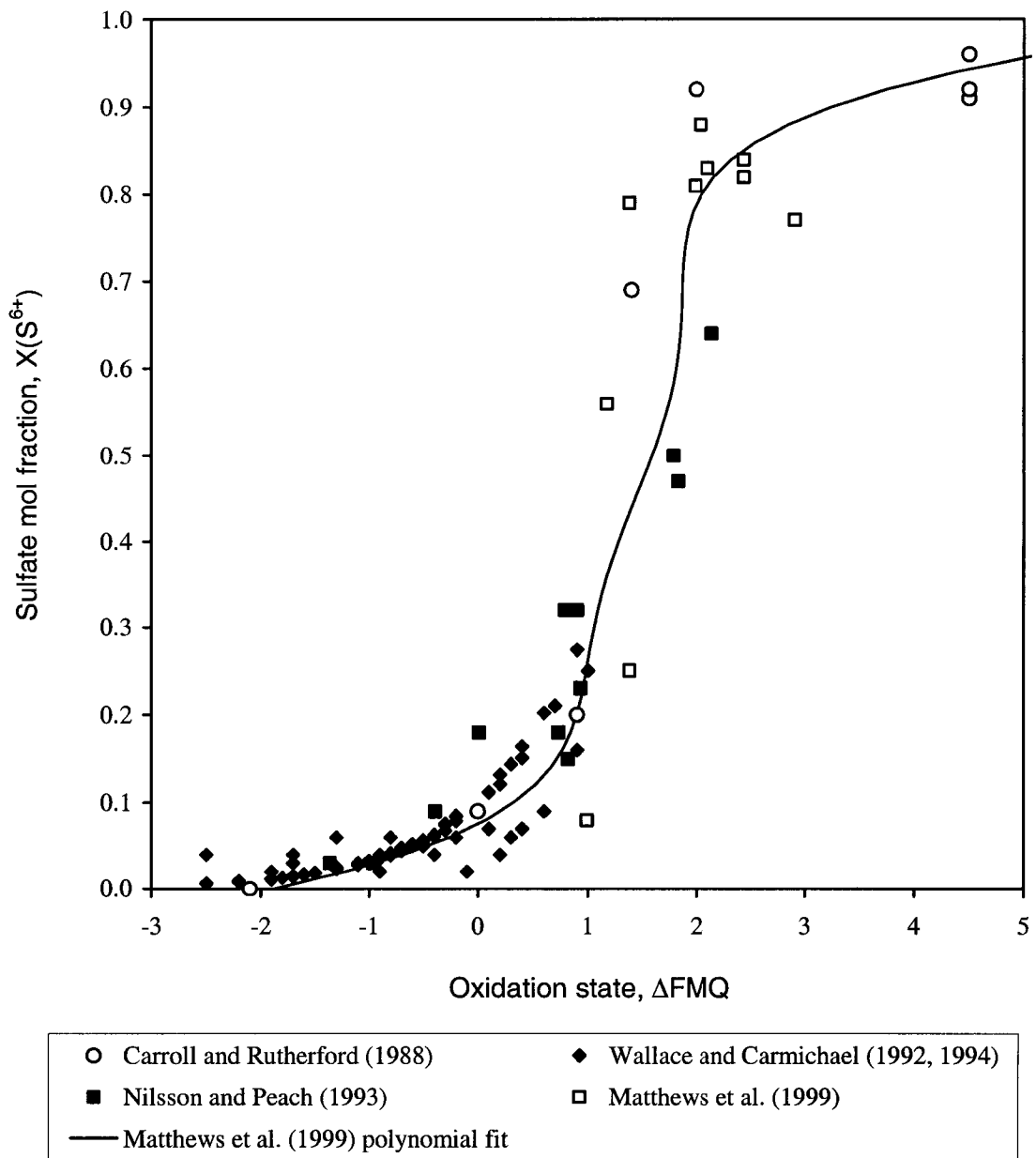
Figure 5.6. Sulfur speciation model of Matthews et al. (1999) using a fifth order polynomial fit, and the data used for the derivation.

To obtain a function that relates sulfur speciation and oxidation state for mafic melts, a non-linear regression to a sigmoidal curve analogous to equation 5.27 (Figure 5.7) was performed using a statistical software package (SigmaPlot) and using only data from basalts and basaltic andesites to minimize compositional effects. The resulting equation:

$$X(S^{6+}) = 0.86/(1 + \exp(2.89 - 2.23\Delta FMQ)) \qquad (5.30)$$

fits the data with a correlation coefficient $r^2 = 0.91$.

Because the average values of $X(S^{6+})$ at high oxidation states are $X(S^{6+}) = 0.83 \pm 0.03$ for the data in Matthews et al. (1999), and $X(S^{6+}) = 0.81 \pm 0.06$ for the data in this work, the asymptotic value for $X(S^{6+})$ in equation 5.30 is $X(S^{6+}) = 0.86$. These values may reflect that sulfur is present as $S^{4+}$ (with $X(S^{6+}) = 0.80 \pm 0.07$, as calculated from the work of Kucha, 1989) but the presence of sulfur as $S^{4+}$ instead of $S^{6+}$ could not be evaluated in this work.

The relation obtained in equation 5.30 indicates that maximum change in speciation from sulfide to $X(S^{6+}) = 0.86$ is expected to occur in the range FMQ-2 to FMQ+3, but the transition is more abrupt between FMQ and FMQ+2 with a change in speciation from $X(S^{6+}) \approx 0.05$ to $X(S^{6+}) \approx 0.70$, respectively.

If solved for $\Delta FMQ$:

$$\Delta FMQ = 1.30 - 0.45[\ln(0.86 / X(S^{6+}) - 1)] \qquad (5.31)$$

this relationship could be used for preliminary estimations of the oxidation state of basaltic glasses, in particular in the range $0.2 < X(S^{6+}) < 0.7$ ($\sim 0.75 < \Delta FMQ < \sim 2$) where the curve can be approximated to a linear function:

$$\Delta FMQ = 2.28X(S^{6+}) + 0.32 \qquad (5.32)$$

and the uncertainties associated with the estimation of $X(S^{6+})$ translate to small uncertainties in $\Delta FMQ$ because of the slope of the line (Figure 5.8). However, more direct methods (e.g., olivine-orthopyroxene-spinel equilibria) are recommended for the estimation of oxidation states when possible (i.e., if the required phases are present).
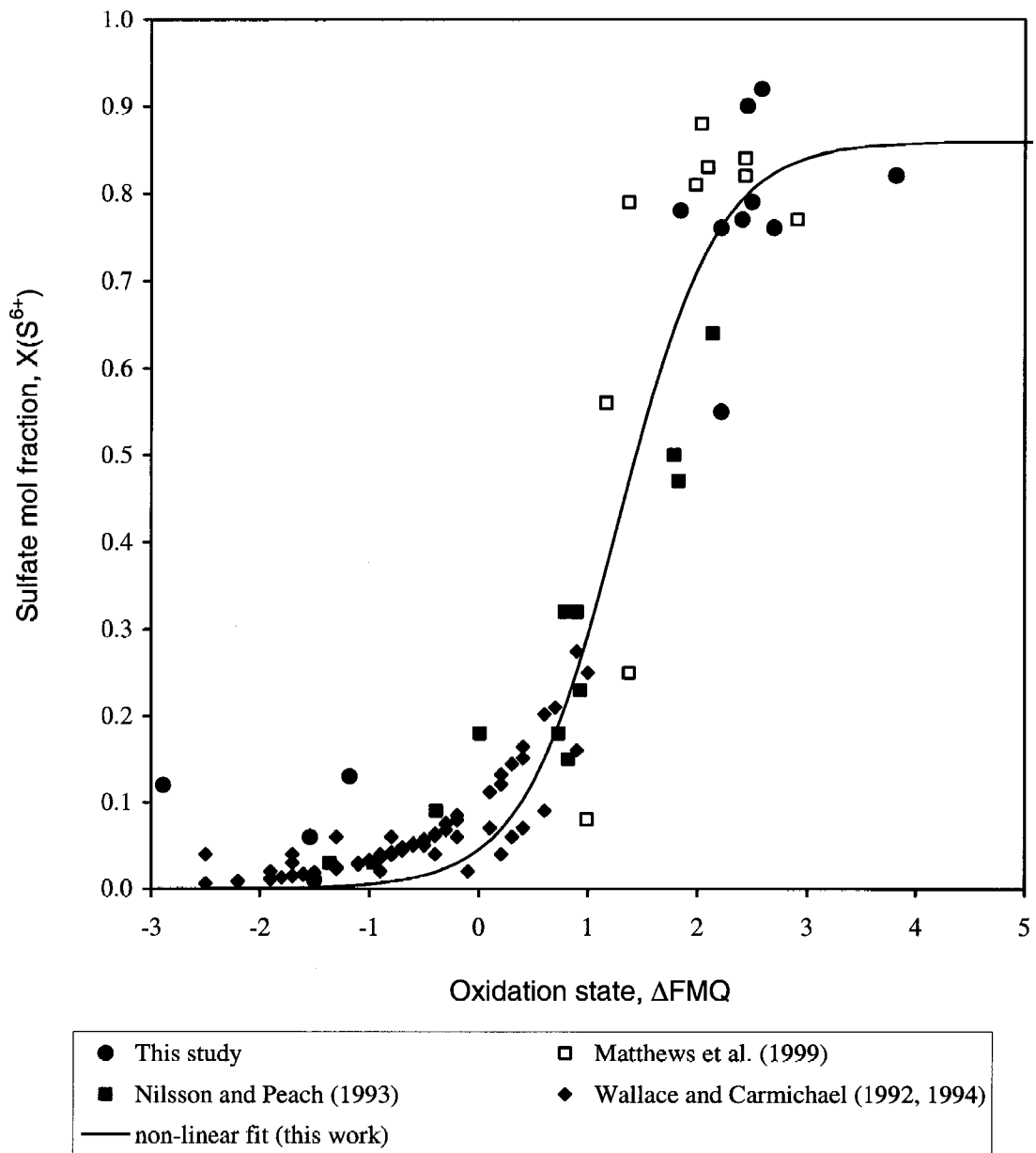
Figure 5.7. Curve for sulfur speciation against oxidation state obtained from non-linear regression of the data shown.
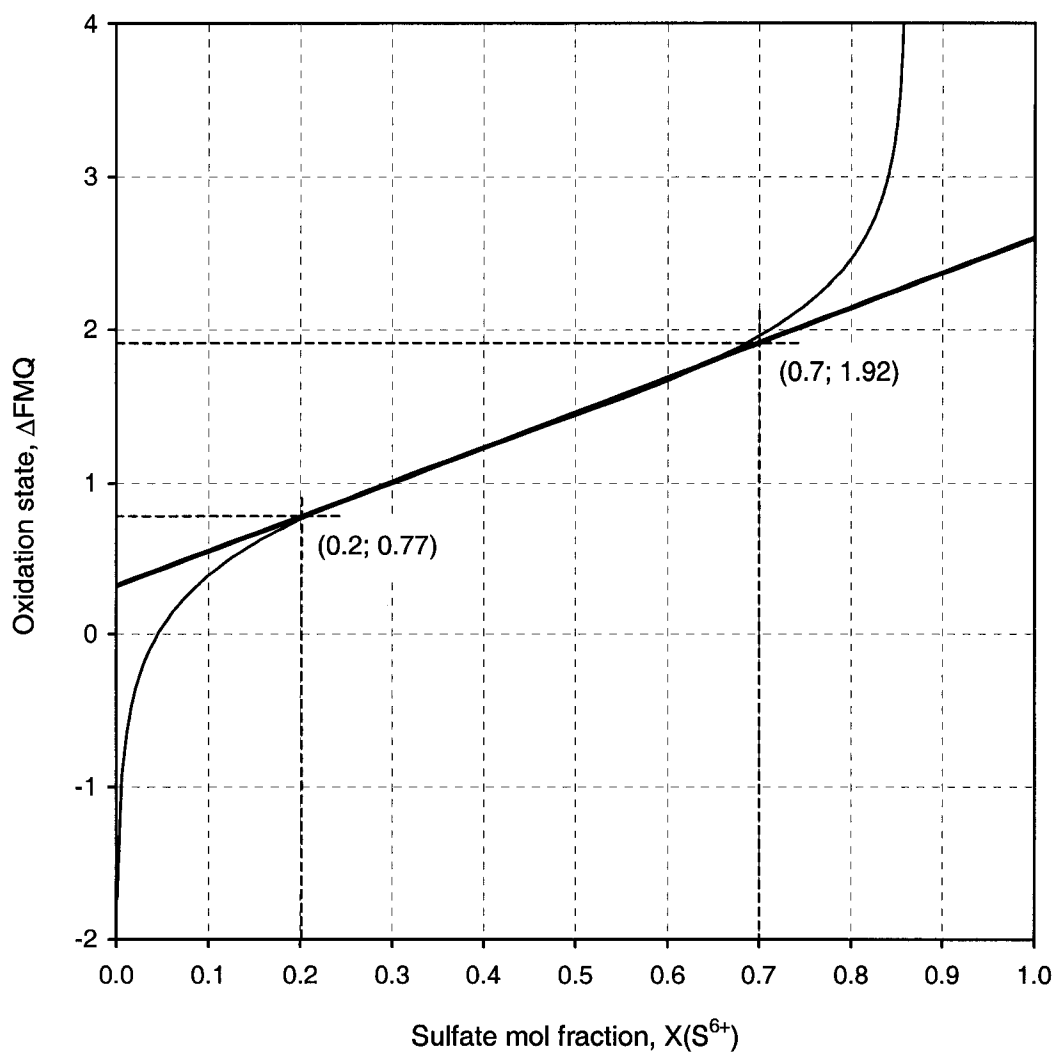
Figure 5.8. Oxidation state against sulfur speciation (equation 5.31). The straight line is the linear fit of the curve in the interval $0.2 < X(S^{6+}) < 0.7$ (equation 5.32). Numbers in parenthesis are $X(S^{6+})$ and the $\Delta FMQ$ calculated from the linear regression).

112

Additional independent estimations of oxidation state and sulfur speciation (in particular in the range $+1 < FMQ < +2$) are needed before equation 5.32 can be used to estimate oxidation state with confidence. For $X(S^{6+})$ outside the range $0.2 < X(S^{6+}) < 0.7$, where the curve defined by equation 5.31 becomes asymptotic, small differences in $X(S^{6+})$ translate to large differences in $\Delta FMQ$ and the equation is not reliable for the estimation of oxidation states, although it constrains $X(S^{6+}) < 0.2$ to $\Delta FMQ < +0.75$, and $X(S^{6+}) > 0.7$ to $\Delta FMQ \geq +2$.

## 5.3. Sulfur solubility

Sulfur solubility in basaltic systems has been investigated extensively (see Poulson and Ohmoto, 1990 for a compilation). However, most studies have been done under low oxidation states, where sulfide is the only stable sulfur-bearing phase. The only available experimental data on the solubility of sulfur in sulfate-bearing systems are the work of Carroll and Rutherford (1985,1987), and Luhr (1990). Fincham and Richardson (1954), Nagashima and Katsura (1973), and Katsura and Nagashima (1974) investigated sulfur "solubility" at 1 atmosphere under oxidizing conditions. In their experiments, the melts did not coexist with any sulfur-bearing solid phase, so their data do not reflect true solubility values but rather the dependence of S concentration in a liquid on the partial pressure of S in a gas phase (Henry's law), as discussed in detail in section 5.2.1. Carroll and Rutherford (1985,1987), and Luhr (1990) investigated the conditions for anhydrite saturation in trachyandesitic to dacitic magmas at shallow, upper crustal conditions of pressure and temperature. The only indications of sulfur solubility in basaltic magmas under upper mantle pressure and temperature conditions comes from Luhr (1990) who extrapolated his results and predicted sulfur solubilities of 1.5 up to 2.5 wt.% $SO_3$ (0.6 to 1 wt.% S) for basaltic melts at 1200 °C and 3 GPa.

In this section, the change of sulfur solubility as a function of oxidation state from sulfide-saturated systems to sulfate-saturated systems is discussed and several models to relate the change in sulfur solubility with the change in sulfur speciation and oxidation state are presented. Assuming that sulfur speciation is dominantly as sulfide or as sulfate species, two end members for sulfur solubility can be described:

(1) For oxidation states lower than FMQ -2, sulfur is present only as sulfide and sulfur solubility is a function of FeO concentration in the melt, pressure, and temperature. Sulfur solubility under these low oxidation states is directly proportional to FeO content of the melt (Haughton et al., 1974; Poulson and Ohmoto, 1990) and temperature (Holzheid and Grove, 2002). There is no agreement as to how pressure affects sulfide solubility, with some experimental work showing an increase with increasing pressure

114

and some showing a decrease with increasing pressure (Holzheid and Grove, 2002). Figure 5.9A shows that there is a weak correlation between sulfur solubility and FeO concentration in the melt for the sulfide-saturated runs.

(2) The work of Carroll and Rutherford (1985, 1987) and Luhr (1990) showed that sulfur solubility in sulfate-saturated silicate melts is significantly higher than in sulfide-saturated melts and that sulfur solubility as sulfate increases significantly with increasing pressure and temperature. By analogy to sulfide saturated systems, a dependence of sulfur solubility with CaO concentration in the melt could be expected for oxidation states higher than FMQ+2 where sulfur is expected to present as sulfate. There was no correlation between CaO in the melt and sulfur solubility observed in the sulfate-saturated experiments in this study (Figure 5.9B).

The experiments presented here were done over a narrow range of pressure, temperature and composition to isolate as much as possible the effect of oxidation state as the variable of interest. The results indicate that sulfur solubility changes from 0.16 wt.% to 1.5 wt.% over three log units in oxidation state. The range of oxidation state in which this transition takes place lies between FMQ-1 and FMQ+2. Several attempts to conduct experiments in this transitional range of oxygen fugacity for basaltic compositions were made but were unsuccessful. As explained in chapter 2, water-saturated experiments quench to amphibole; thus the use of external buffers that require $H_2$ osmotic equilibration to control $fO_2$ was not possible. Attempts to impose an intermediate oxidation state using different bulk compositions were not totally successful. For example, in runs 34, 54, and 55, ~1 wt.% graphite powder was added to the charge (Table 2.3). The bulk composition in these experiments is almost identical, with the exception of slightly higher S in run 34. Run temperature and duration is identical (T = 1300 °C, t = 4 h) and there is only a small difference in pressure (1.2 GPa for run 34 versus 1.0 GPa for runs 54 and 55). These small differences resulted in run 34 being sulfate saturated (although providing the lowest estimate in oxidation state for sulfate-bearing runs), whereas in the other two experiments the added sulfate was reduced to sulfide.
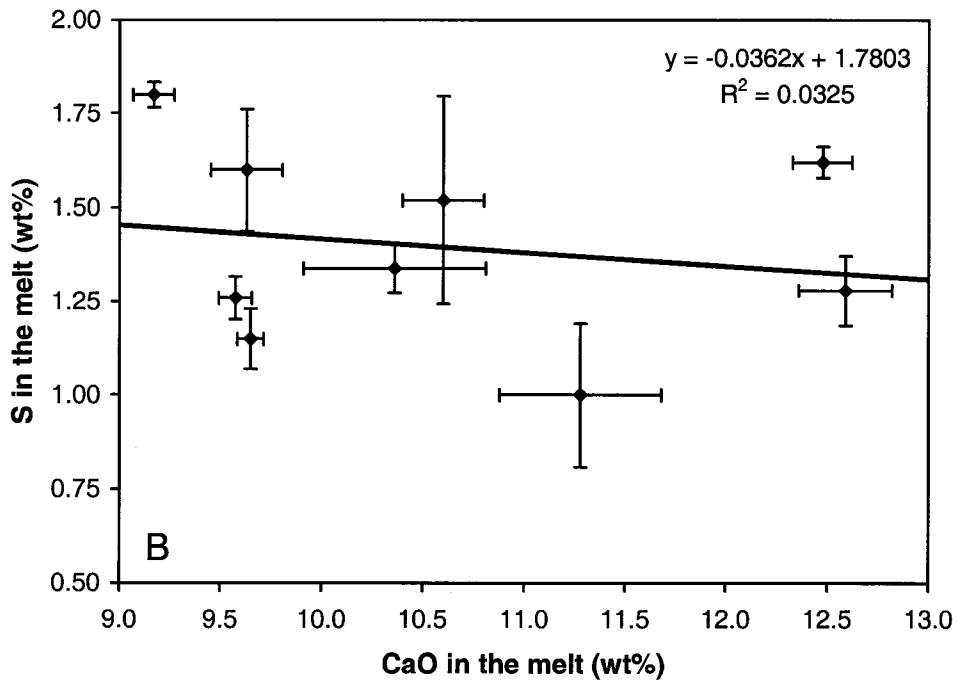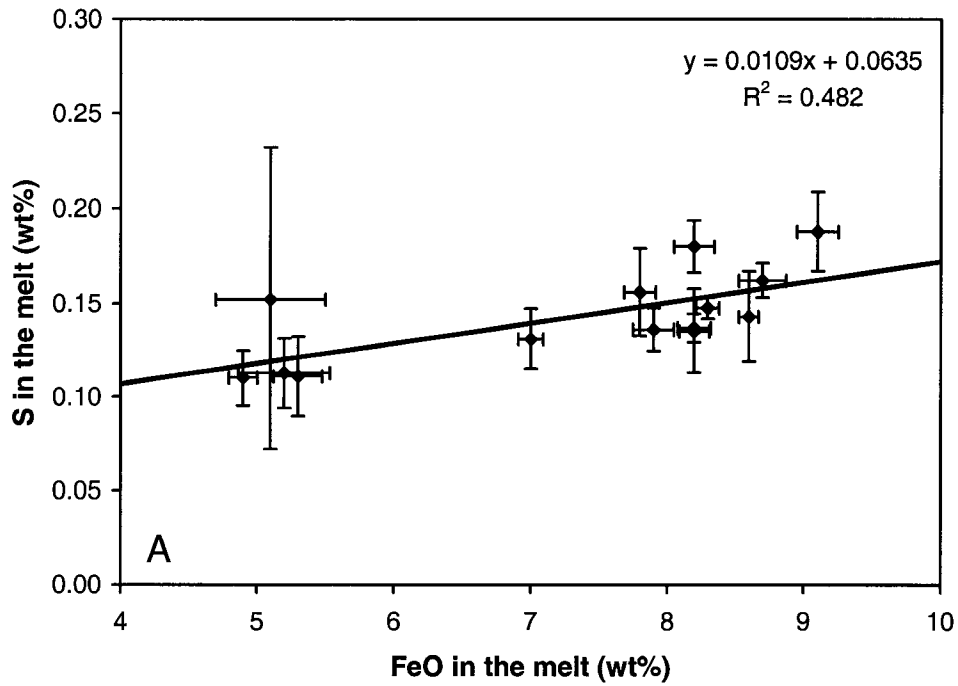
115

Figure 5.9. **A** Sulfur solubility against FeO concentration in the melt for sulfide saturated melts in this study. **B** Sulfur solubility against CaO concentration in the melt for sulfate saturated melts in this study. Note the weak correlation in the first plot and the lack of it in the second.

116

### 5.3.1. The "sulfur solubility minimum" misconception

The work of Fincham and Richardson (1954), Nagashima and Katsura (1973) and Katsura and Nagashima (1974) merits detailed analysis because they are the main source of the paradigm of a "sulfur solubility minimum" at NNO (~FMQ+0.7). This is relevant because this minimum has been used to explain sulfur behavior in a variety of geological problems. Alt et al. (1993), for example, attributed the low S content of submarine arc lavas in the Mariana Arc to loss of sulfur-bearing vapor at NNO, and Kress (1997) used the "sulfur solubility minimum" at NNO to explain magma mixing as a mechanism for the Pinatubo eruption in 1991.

Fincham and Richardson (1954), Nagashima and Katsura (1973) and Katsura and Nagashima (1974) studied sulfur "solubility" as a function of oxidation state at one atmosphere. Sulfur was not added to the samples; instead, sulfur equilibration was obtained by flushing a gas mixture of $SO_2$-$CO_2$-$H_2$ through the furnace, the gas mixture used simultaneously to impose the desired oxygen fugacity. Their data show that at any given oxygen fugacity, the sulfur concentration in the glasses was a function of the initial concentration of $SO_2$ gas flushed through the furnace (a fact that was acknowledged by Fincham and Richardson, 1954, p.51: "if the $SO_2$ input was doubled at a constant $p_{O_2}$ value, the sulphur content of the melt was approximately doubled"). The documented sulfur concentrations in glasses are, with very few exceptions, below 1000 ppm, and mostly on the order of a few hundreds of ppm to below detection limits (~10 ppm). Only Fincham and Richardson (1954) documented the saturation of sulfur-bearing phases in a few of their runs. For those cases they concluded the melt had saturated CaS (their glasses were $CaO$-$Al_2O_3$-$SiO_2$) and wrote "the value of % S in the melt, at which this presumed CaS saturation was found, is in fair agreement with limits found for similar mixtures by other workers. Glaser (1926) found the solubility of CaS in liquid $CaSiO_3$ to correspond to 5.5%S by weight at 1500 °C; Filer & Darken (1952) found that CaS saturation limit in blast-furnace slags to be 3.5 to 4.5%S at 1500 °C. MacCaffery & Oesterle (1923) found the solubility of CaS in $CaO$-$Al_2O_3$-$SiO_2$ melts at 1500 °C to

117

correspond to about 8%S for 'acid' melts and 11% for more 'basic' melts." (Fincham and Richardson, 1954, p.51).

A strict definition of the term "solubility" implies saturation of the solution with a condensed phase. At saturation, addition of more of the substance in consideration (e.g., sulfur) to the system increases the amount of the condensed phase present (e.g., sulfide or sulfate) without increasing the concentration of the substance in the solvent. Below saturation, addition of the condensed phase increases the concentration of the substance in the solvent without precipitating a condensed phase (i.e., the condensed phase is "dissolved"). Thus, "solubility" is the maximum concentration of a substance in a solvent. The sulfur concentrations documented by Fincham and Richardson (1954), Nagashima and Katsura (1973), and Katsura and Nagashima (1974) reflect Henry's law correlations between the partial pressure of sulfur species in a gas and the concentration of those species in the silicate liquid and do not provide relevant information on the sulfur concentration required to saturate a silicate melt in either sulfide or sulfate.

The results documented by Carroll and Rutherford (1985, 1987) (Figure 5.10) have also been used to support the claim of a sulfur solubility minimum at NNO (e.g., Kress 1997). Carroll and Rutherford (1985) used graphite-methane (GCH $\approx$ FMQ-3), FMQ, manganosite-hausmanite (MnO - $Mn^{2+}Mn_2^{3+}O_4$ or MNO $\approx$ FMQ+4), and magnetite-hematite (MH $\approx$ FMQ+4.5) to buffer the oxidation state in their experiments. An apparent trend towards a minimum solubility around NNO could be inferred (e.g., dot-dash curve in Figure 5.10), but it results from the effect of very high FeO in some of the experiments buffered at GCH (FeO $\geq$ 17.8 wt.% versus all other data at FeO $\leq$ 7.3 wt.%). If only data with similar FeO content are used (dashed curve), the data from Carroll and Rutherford (1985, 1987) do not support the idea of a S solubility minimum at NNO. The data rather show that below NNO ($\Delta$FMQ $\approx$ +0.7) changes in oxidation state do not have significant impact on sulfur solubility.

118

4000

Experimental data from Carroll
and Rutherford (1985, 1987)
**200 MPa. 1025 °C**

3500

♦ (22.6)

(4.7)

3000

2500

(3.6)

[S] (ppm)

2000

(17.8)

(5.1)

1500

1000

(7.3)

(6.9)

500

(2.1)          (7.1)

(4.1)

(3.7)          (5.3)

(5.4)

0

-4    -3    -2    -1    0    1    2    3    4    5

Oxidation state, ΔFMQ
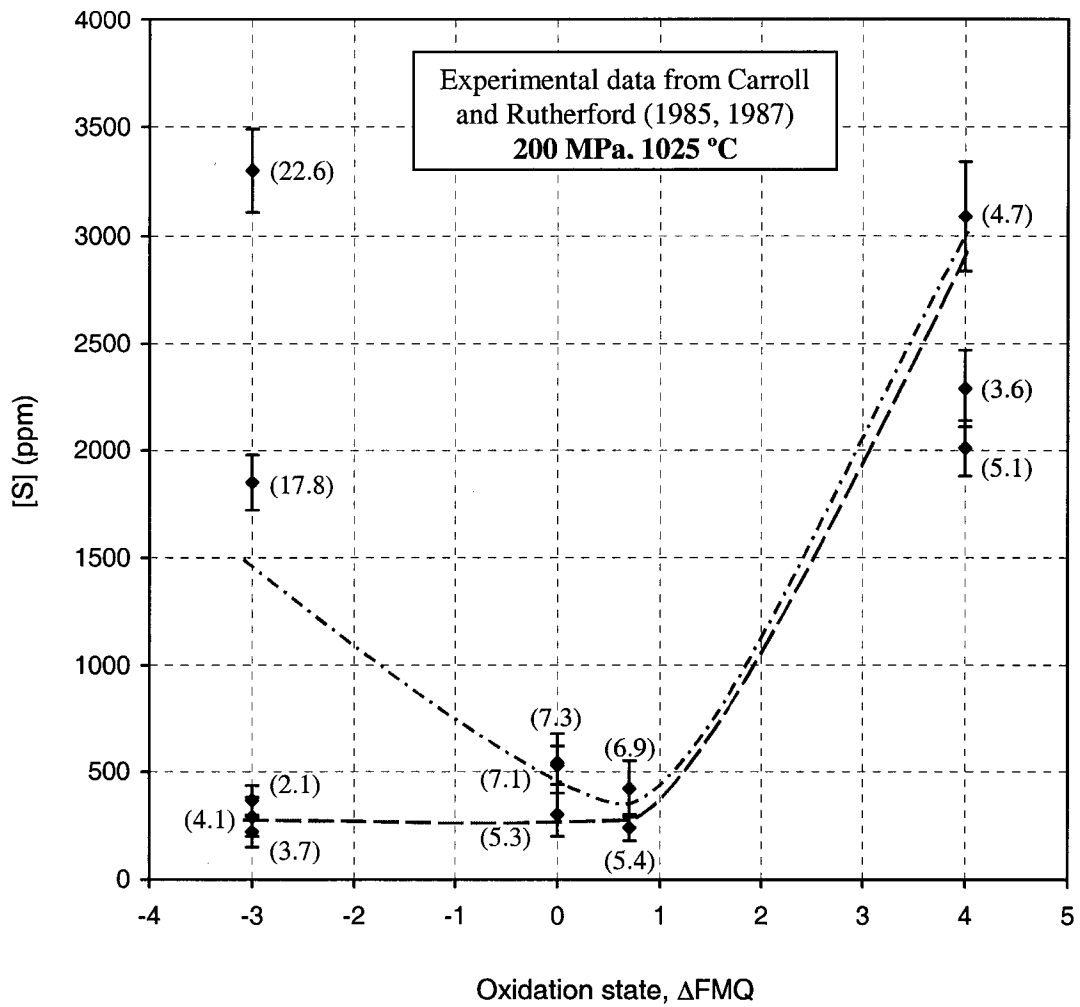
Figure 5.10. Sulfur solubility against oxidation state from Carroll and Rutherford (1985, 1987). Numbers in parenthesis are FeO content in the melt. The dot-dash curve (U-shaped) is the trend showing an apparent minimum in the solubility of sulfur that results from using all the data without consideration of differences in FeO content in the glasses. The dashed curve is the approximate shape of the curve if the data with FeO content higher than 7.3 wt. % are excluded.

119

## 5.3.2. Sulfur solubility models for the transition from sulfide to sulfate species dominance

Three models for sulfur solubility as a function of oxidation state are derived in this section. The first one assumes that changes in sulfur solubility with changes in oxidation state mirror the changes in sulfur speciation. The second model uses the data in this work and constraints from the experimental data of Carroll and Rutherford (1985, 1987) which provide the only available experimental data on sulfur speciation and solubility in the range $-1 < FMQ < +1.5$. This model assumes that changes in sulfur solubility are negligible below NNO (FMQ = 0.7). The third model provides the limiting case in which the change in solubility is sharp at FMQ $\approx$ +1.9 (the minimum oxidation state in the sulfate-saturated experiments in this work).

If changes in sulfur solubility against oxidation state mirrors the changes in sulfur speciation (model 1), these changes can be described with an equation analogous to equation 5.32 but of the form:

$$y = K/(1+\exp(a-bx)) + y_o \qquad (5.33)$$

The parameters "a" and "b" are related to the translations in "x" ($\Delta FMQ$ in this case) and therefore, are taken directly from equation 5.30. The parameters "K" and "$y_o$" are related to "y" and define the asymptotic values of the sigmoidal curve. Because "b" is positive when "x" tends to $-\infty$ the exponential term tends to $+\infty$ and the ratio $K/(1+\exp(a-bx))$ tends to zero. Therefore, the minimum asymptotic value is:

$$y_{min} = y_o \qquad (5.34)$$

whereas when "x" tends to $+\infty$ the exponential term tends to zero and the maximum asymptotic value corresponds to:

$$y_{max} = K + y_o \qquad \text{or} \qquad y_{max} = K + y_{min} \qquad (5.35)$$

thus, $K = y_{max} - y_{min}$, and the general equation that relates sulfur solubility and oxidation state can be expressed as:

$$[S]_t = \frac{[S]_{max} - [S]_{min}}{(1 + \exp(a - b \times \Delta FMQ))} + [S]_{min} \qquad (5.36)$$

120

The minimum sulfur solubility corresponds to the solubility measured in sulfide-dominated-systems and the maximum sulfur solubility corresponds to the solubility in sulfate dominated-systems. For the conditions of the experiments presented here (1300 °C and 1 GPa) a minimum S solubility $[S]_{min} = 0.14 \pm 0.02$ wt.% was obtained from 5 samples produced by reduction of sulfate to sulfide ($[S]_{min} = 0.13 \pm 0.02$ wt.%; runs 27a, 35C, 53, 54, 55) and 8 runs produced by sulfur saturation of glass with sulfide ($[S]_{min} = 0.15 \pm 0.02$ wt.%; runs 2, 3, 4, 5, 7, 10, 11, and 12). A maximum S solubility $[S]_{max} = 1.5 \pm 0.2$ wt.% was obtained from an average of 8 samples (runs 26, 30Ca, 30Fe, 35AuPd, 50, 52, 56, and 57) that are sulfate saturated.

Using these values for sulfur solubility at sulfide and sulfate saturation in equation 5.36, we can then derive an expression to estimate sulfur solubility as a function of oxidation state for basaltic compositions at $T \approx 1300$ °C and $P \approx 1$ GPa:

$$[S]_t = \frac{1.36}{1 + exp(\,2.89 - 2.23\Delta FMQ\,)} + 0.14 \tag{5.37}$$

Figure 5.11 shows some of the data used to derive equation 5.37 and the fit provided by this equation. Some of the data used to obtain $[S]_{min}$ are not plotted because their oxidation state could not be determined. However these runs consisted of sulfide-bearing starting materials equilibrated in graphite capsules and therefore at $fO_2 <$ FMQ-1.5. According to this model sulfur solubility starts to increase at FMQ-1 and is expected to be ~6000 ppm at FMQ +1.

In contrast, the results of Carroll and Rutherford (1985, 1987), shown in Figure 5.10, indicate that for their experiments the increase in sulfur solubility was only noticeable after the oxidation state increased above NNO. Despite numerous attempts, and because external buffers could not be used in this study, no data on sulfur solubility is available in the range -1<FMQ<1.5 could be obtained in this work. Because they provide experimental data in the range of oxidation state of interests, the results of Carroll and Rutherford (1985, 1987) will be used to derive the second model. Comparing sulfur speciation (Figure 5.4) and sulfur solubility from their experiments (Figure 5.10) it can be
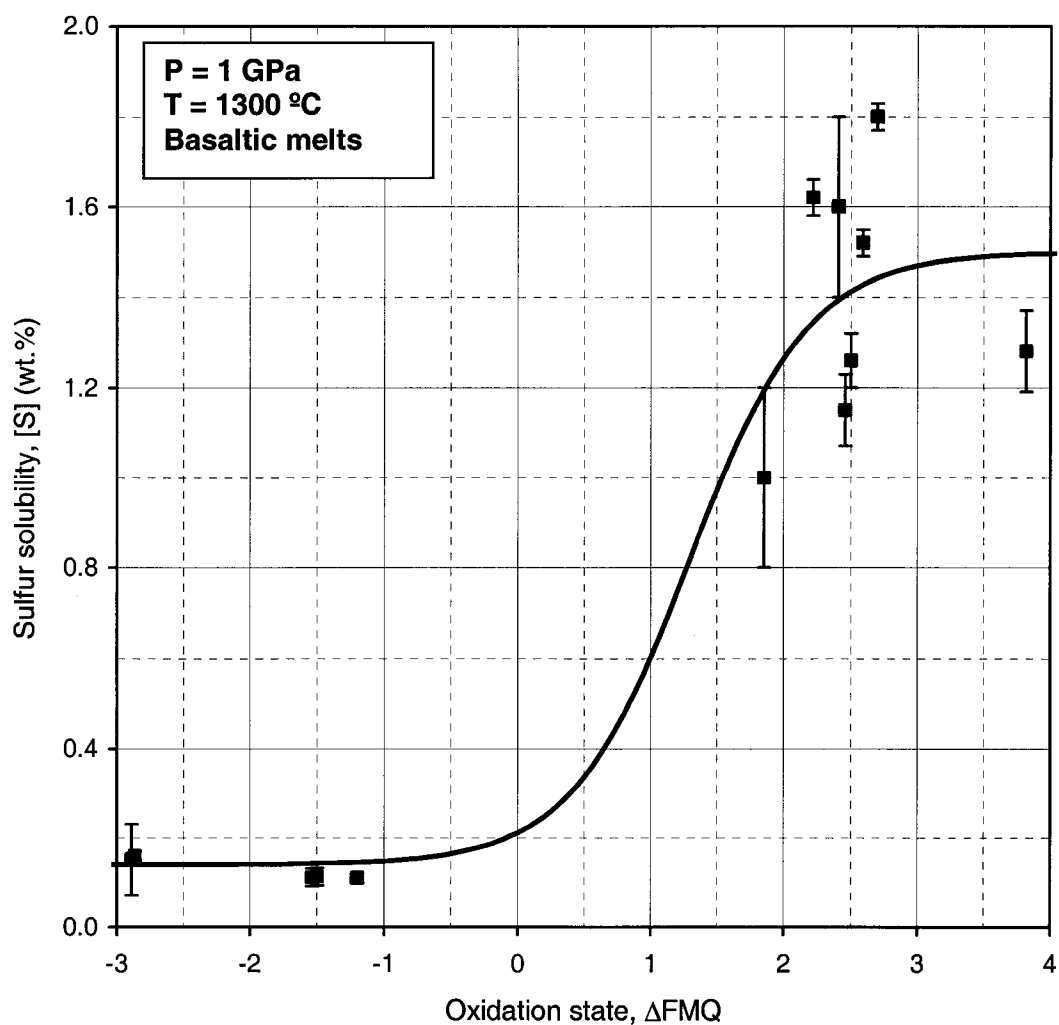
121

Figure 5.11. Sulfur solubility as a function of oxidation state from equation 5.37 (model 1) and the experimental data used to derive it. According to this model the effect of oxidation starts to be noticeable at about FMQ-1. At FMQ+0.5 a sulfur solubility of 4000 ppm can be expected, and at FMQ+1 sulfur solubility is 6000 ppm.

seen that although speciation starts changing at FMQ-1, there is no effect on sulfur solubility until oxidation state reaches NNO (FMQ+0.7) and $X(S^{6+}) \approx 0.3$.

A third model, which provides the limiting case for the change of sulfur solubility from sulfide- to sulfate-dominated systems, is constructed assuming that oxygen fugacity needs to reach FMQ+2 before solubility as sulfate overtakes solubility as sulfide.

For both model 2 and model 3 the conditions for minimum sulfur solubility ([S] = 0.14 wt.%) and maximum sulfur solubility ([S] = 1.5 wt.%) are kept. The generalized sigmoidal curve analogous to equation 5.37 is:

$$[S]_t = \frac{1.36}{1 + exp(a - b\Delta FMQ)} + 0.14 \tag{5.38}$$

but in this case the parameters "a" and "b" (related to the slope and position of the steep part of the sigmoidal curve) are varied to fit the constraints discussed above for models 2 and 3.

To obtain these parameters two points in [S]-$\Delta$FMQ space are needed. For model 2, the curve is forced to pass through NNO (FMQ+0.7) at [S] = 0.1536. This value of [S] at NNO corresponds to 1% contribution of sulfur solubility as sulfate ([S] = 0.14 + 1.36/100) and is used as an approximation because 0% contribution in sulfur solubility in equation 5.38 does not have a solution (it corresponds to the asymptotic value at FMQ-$\infty$). The curve is also forced to pass through the values obtained from run 34 (FMQ+1.85; [S] = 1), the only control point available between the minimum and the maximum sulfur solubility data.

For model 3 (the limiting case), the curve is forced to pass through the point defined for run 34 and produces the maximum change in sulfur solubility over the minimum interval in oxidation state. Thus, an arbitrary point at FMQ+1.8 and [S] = 0.1536 (as above) was used for the calculations.

123

For model 2, the empirical sulfur solubility function of oxidation state is:

$$[S]_t = \frac{1.36}{1 + exp(7.72 - 4.47\Delta FMQ)} + 0.14 \qquad (5.39)$$

For model 3, the empirical sulfur solubility function of oxidation state is:

$$[S]_t = \frac{1.36}{1 + exp(189.54 - 102.75\Delta FMQ)} + 0.14 \qquad (5.40)$$

Figure 5.12 compares the change in sulfur solubility for the three models presented. Additional experimental work on sulfur solubility in the range 0<FMQ<+2 would allow testing of the three models. In the absence of additional data, the curve defined for model 2 is the preferred model because it takes into consideration the results from this work and the constraints placed by the work of Carroll and Rutherford (1987) (although it requires that there be no significant control of the bulk composition on sulfur solubility). According to this model (and for the conditions of the experiments in this work) sulfur solubility is expected to increase from ~0.14 wt.% to ~1.5 wt.% S between FMQ+1 and FMQ+2.5. The implications of this change in sulfur solubility are discussed in section 5.4.
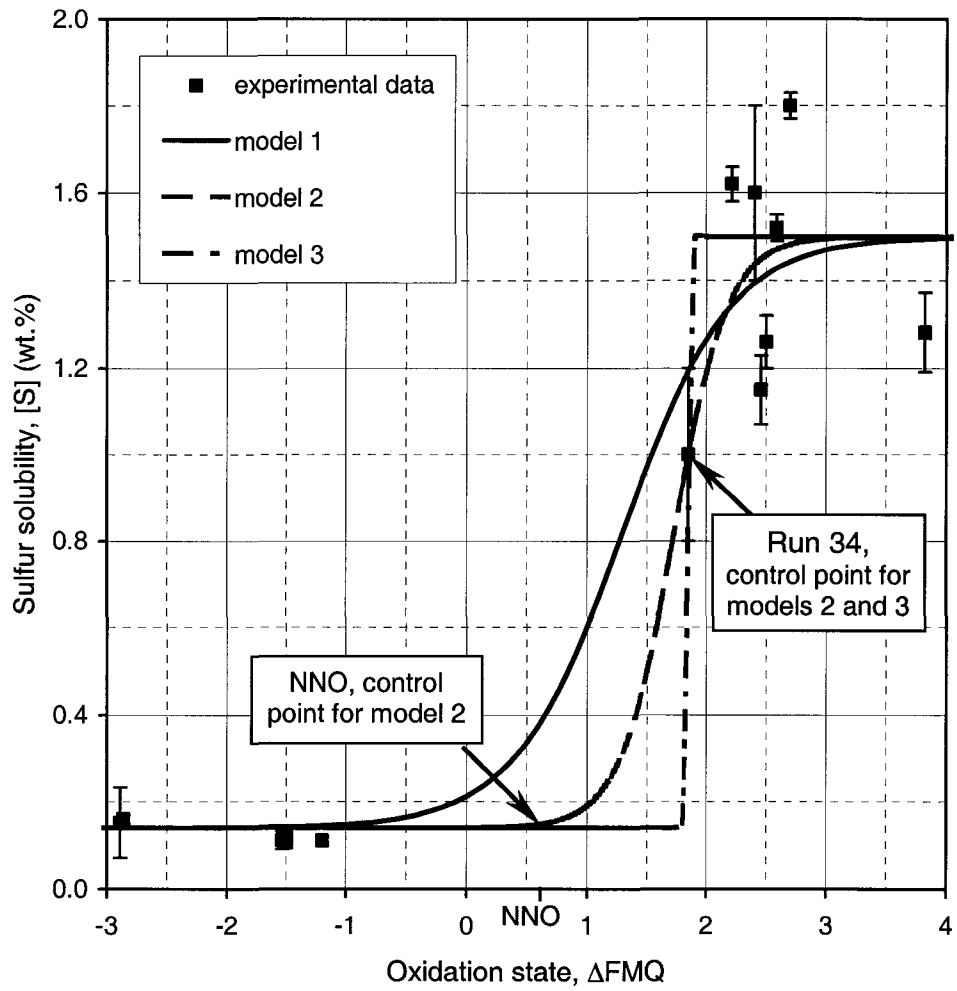
Figure 5.12. Comparison of the three models derived for sulfur solubility as a function of oxidation state. Run 34 (control point for models 2 and 3) is indicated.

## 5.4. Generation of sulfur-undersaturated magmas in oxidized systems

The marked increase in sulfur solubility with increasing oxidation state, shown in the previous section, has significant implications for the behavior of sulfides during partial melting of the mantle. To produce a sulfur-undersaturated magma, the most commonly proposed mechanism is dissolution, either by a large degree of melting (e.g., Keays, 1995) or by two-stage melting (e.g., Wyborn and Sun, 1994). The importance of oxidation as a possible mechanism for sulfide elimination in primitive magmas has not been studied in detail, although it has received some attention (Richards et al., 1991; Sillitoe, 1997; Mungall, 2002). In this section, the models for sulfur solubility as a function of oxidation state obtained in the previous section will be used to derive models to estimate the degree of partial melting required to produce sulfur-undersaturated melts in subduction zone settings.

Keays (1995) presented a simple model for the generation of sulfur-undersaturated melts and O'Hara et al. (2001a,b) present a more complex model for the effects of minor phases on the behavior of trace elements. Most of the notation adopted here is from the work of O'Hara et al. (2001a,b). O'Hara et al. (2001b, p. 1887) defined "carrier phases" as "minor phases which strongly concentrate selected trace elements [and which] release relatively large amounts of those elements to the liquid phase when they are eliminated during partial melting and glean relatively large amounts of those elements when they first appear during progressive crystallization". This definition clearly applies to sulfide phases as carriers of the HSE, which is indeed the example discussed in O'Hara et al. (2001b).

Based on 1 atm experiments (e.g., Craig and Kullerud, 1969), no solid phases are expected above 1200 °C in the system Fe-Cu-Ni-S. For this reason, modeling the behavior of mantle sulfides typically involves a single phase (an immiscible sulfide liquid) although distinctive sulfide populations of different composition have been documented in mantle assemblages (e.g., Alard et al., 2000). Assuming a single sulfide phase and that sulfides are the only sulfur-bearing phase in the mantle, the melt fraction

needed for sulfide elimination can be estimated following the approach implicitly used by Keays (1995):

$$F_s = [S]_o / [S]_m \tag{5.41}$$

where $F_s$ is the melt fraction at sulfur saturation, $[S]_o$ is the initial sulfur concentration in the mantle assemblage, and $[S]_m$ is the sulfur solubility of the silicate melt. Assuming an initial mantle concentration of 250 ppm S (McDonough and Sun, 1995) and a S solubility (S capacity) in the melt of 1000 ppm, Keays (1995) concluded that a minimum 25% partial melting ($F_s = 0.25$) is needed to produce a sulfur undersaturated melt.

Estimations of the degree of partial melting needed to produce sulfur undersaturated melts by one or two stages of melting may be based on equation 5.41. Therefore, this equation will be used to model the effect of changes in sulfur solubility with oxidation state on the degree of partial melting required to generate a sulfur undersaturated melt by substituting the denominator for the expression of [S]$_t$ obtained in the previous section for equation 5.36.

The resulting generic equation for the critical melt fraction at which the silicate melt is sulfur undersaturated is:

$$F_s = [S]_o \times \frac{(1 + exp(a - b \times \Delta FMQ))}{([S]_{max} + [S]_{min} \times exp(a - b \times \Delta FMQ))} \tag{5.42}$$

The curves defined by this equation for the three models for sulfur solubility derived in the previous section are shown in Figure 5.13 for [S]$_o$ = 500 ppm. Figure 5.14 illustrates the effect of different [S]$_o$ using model 2. As expected, the curves show that as sulfur solubility increases with increasing oxidation state, the degree of partial melting required to generate a sulfur undersaturated melt decreases. The shaded region in both Figures

127

Figure 5.13. Melt fraction needed to produce sulfur-undersaturated melts as a function of oxidation state for the three models for sulfur solubility derived in the previous section. The vertical shaded band is the range of oxidation state at the arc magma source estimated by Parkinson and Arculus (1999).
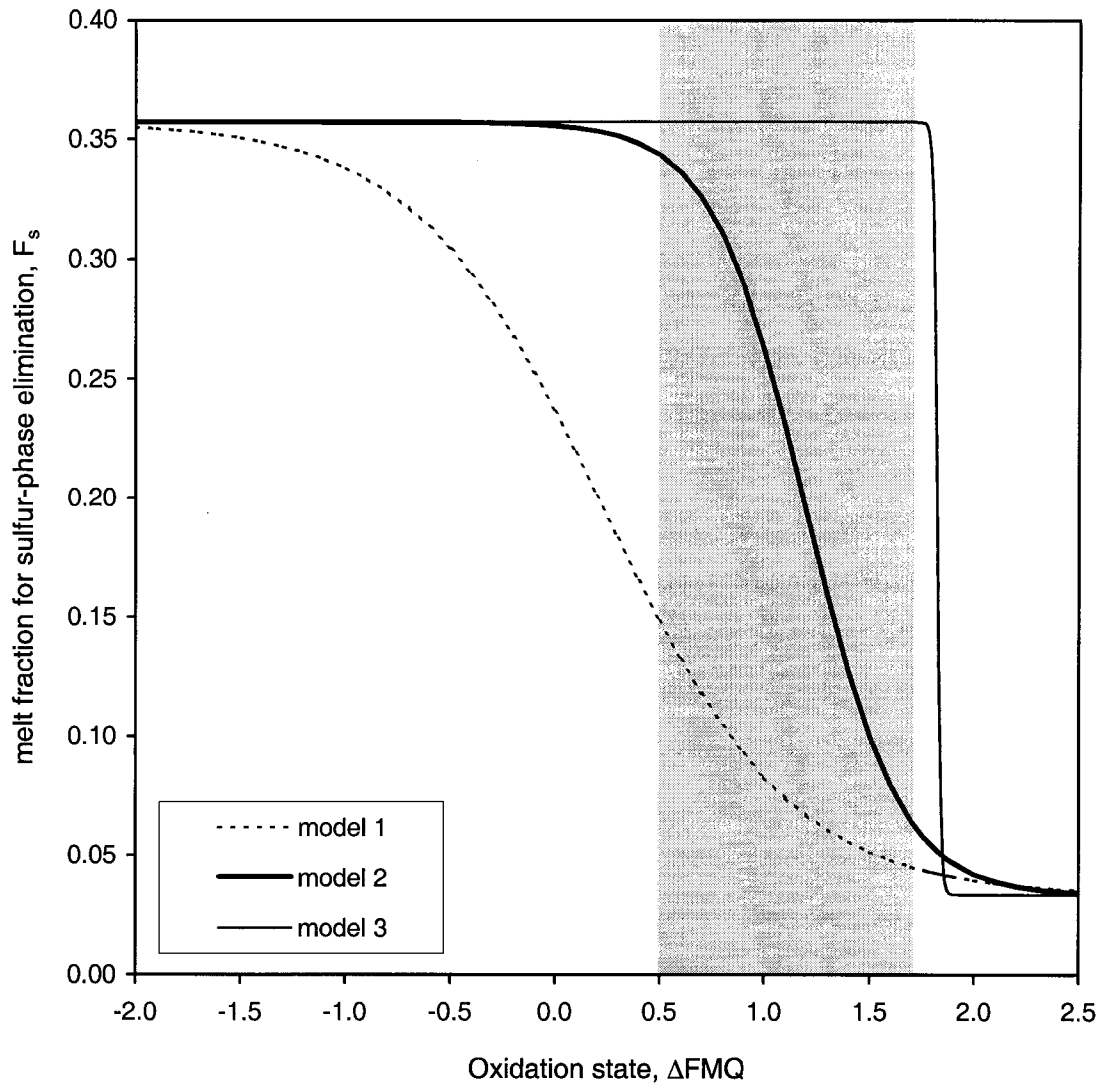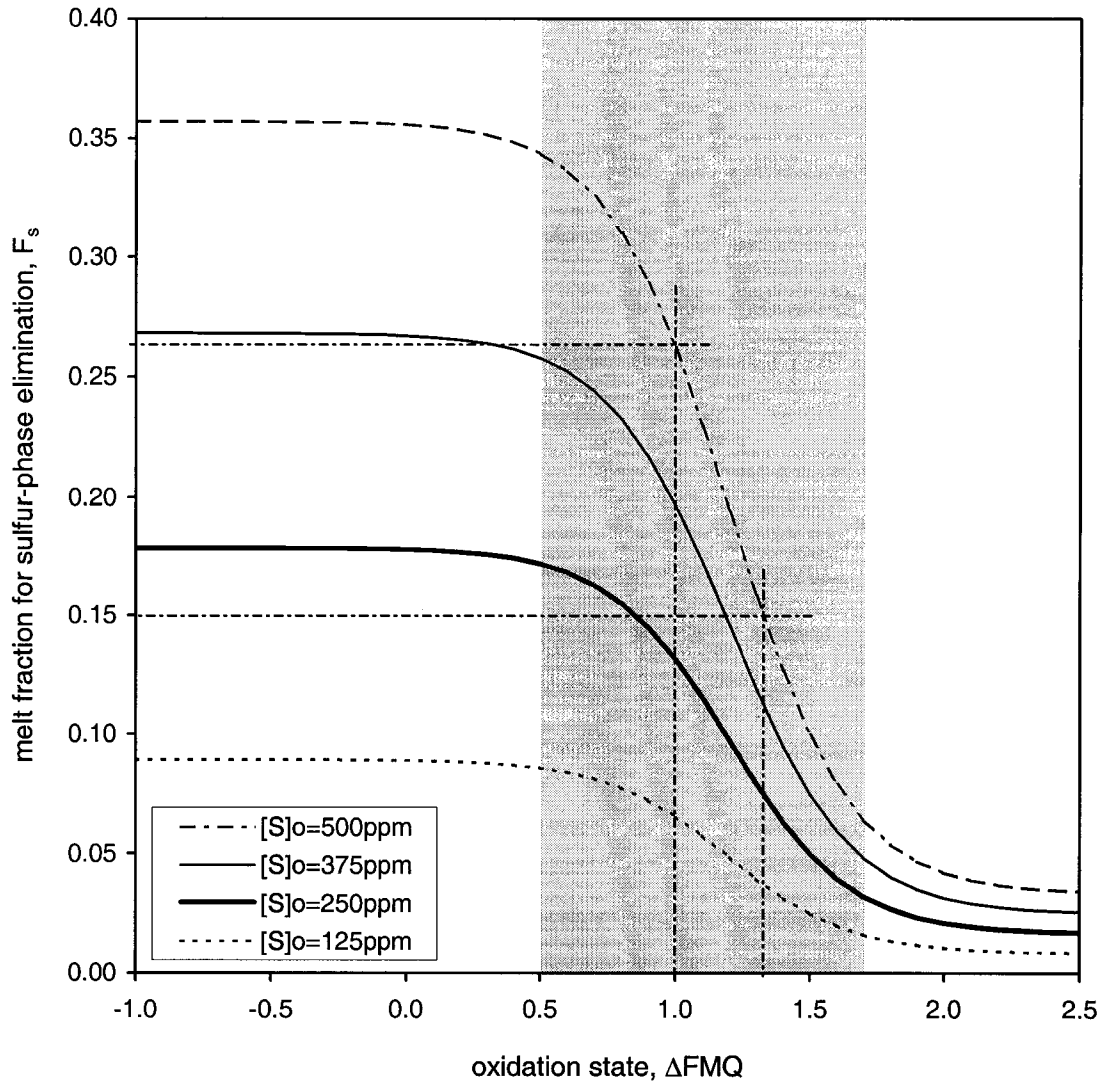
128

Figure 5.14. Melt fraction needed to produce sulfur-undersaturated melts as a function of oxidation state for model 2 and different initial sulfur concentrations. The vertical shaded band is the range of oxidation state at the arc magma source estimated by Parkinson and Arculus (1999).

129

defines the range of oxidation state estimated by Parkinson and Arculus (1999) to be that in which arc magmas are typically generated (FMQ+0.5 to FMQ+1.7). Although the average sulfur concentration in the mantle was estimated at $250 \pm 50$ ppm by McDonough and Sun (1995), sulfur concentrations in mantle assemblages in supra-subduction zones are expected to be higher due to sulfur flux from the subducting slab (Alt et al., 1993; de Hoog et al., 2001). Minimum sulfur concentrations in the mantle source in subduction zones were estimated to be ~ 470 ppm by de Hoog et al. (2001) based on measurements of olivine-hosted melt inclusions from basalts of the Galunggung volcano (Indonesia). A value of [S] = 500 ppm is used in Figure 5.13 to compare the three models. The maximum and minimum melt fractions needed to produce sulfur undersaturated magmas are $F_s = 0.36$ and $F_s = 0.03$, respectively, for all models. The difference between the models is the range in oxidation state at which the transition takes place, but even using in the extreme scenario (model 3) it can be concluded that above FMQ+1.9 all sulfur is expected to be dissolved in the basaltic melt.

Using model 2 as the most reasonable model based on the available experimental data, and for a relatively high initial sulfur concentration in the mantle source (500 ppm), Figure 5.14 shows that at FMQ+1 Fs $\approx 0.26$, and that Fs $\leq 0.15$ for FMQ $\geq +1.33$. Thus, it is reasonable to conclude that magmas generated in oxidized mantle sources are likely to be sulfur undersaturated, and that two-stage melting (e.g., Wyborn and Sun, 1994) is not a prerequisite for this. However, two-stage melting may also favor the generation of sulfur-undersaturated magmas, the two processes (sulfide oxidation and two-stage melting) not being mutually exclusive.

## 5.5. Implications for magmatic systems

### 5.5.1 Implications for the behavior of the HSE

The control of sulfides on the behavior of the highly siderophile elements has been extensively documented. Mitchell and Keays (1981), for example, measured Au, Pd, and Ir in mineral separates from spinel and garnet lherzolites from four different localities. From mass balance calculations they concluded that between 60 to 80% of the bulk HSE was hosted as sulphide-rich intergranular components, the remaining fraction being hosted in the oxides and silicates. Alard et al. (2000) documented HSE concentrations in mantle sulfides that range from 10 to 105 times their concentration in primitive mantle, enough to account for the bulk concentration of the HSE even if sulfides represent ~0.1wt% of the mantle assemblage. However, the nature of the association between sulfides and the HSE is complex. Alard et al. (2000) described two distinctive sulfide populations in mantle assemblages and showed that sulfides enclosed in silicates approach the composition of monosulfide solid solution and preferentially host Os and Ir relative to Pd and Au whereas interstitial sulfides (in particular those with higher Cu content) contained more Pd and Au. Lorand et al. (1999) studied variations of the HSE in lherzolite and harzburgites from Pyrenean orogenic massifs. Based on systematic variations of the HSE with Cu and S, they concluded that, except for Au and Pd, the HSE resided as "melting resistant atomic clusters or microalloys" (Lorand et al., 1999, p. 957). Ballhaus and Sylvester (2000) documented the presence of HSE in sulfides from the Merensky reef (Bushveld Complex, South Africa). Their work shows that Ir-Os-Pt are the dominant type of nuggets in sulfides. Ballhaus and Sylvester (2000) also showed that Pd is present in solution in pentlandite, which is consistent with the interpretation of Lorand et al. (1999) for the chalcophile behavior of Pd. In any case, regardless of whether the HSE are hosted in the sulfides as solution or as micro-inclusions, sulfide stability plays a significant role on the behavior of the HSE. The different behavior of the HSE become significant for their fractionation once sulfides are removed.

The results of this work confirm the markedly chalcophilic behavior of Pd relative to Ir and Pt, which have more affinity to form alloys (Table 4.15, Figures, 4.18 and 4.19), but are inconclusive for Au, which did not partition as strongly as Pd into the sulfide. This could be explained by the lack of Cu in the experiments. Jugo et al. (1999) showed that, at 800 °C and 100 MPa, Au partitions strongly into intermediate solid solution (iss, roughly the high temperature equivalent of chalcopyrite) relative to pyrrhotite. This behavior is not expected to change significantly with increasing temperature and pressure, and is consistent with the high Au concentrations in Cu-rich pyrrhotites documented in Alard et al. (2000).

My experiments also indicate that all four HSE studied (Pd, Ir, Pt and Au) have strong affinities for iron. This is shown by the ubiquitous occurrence of submicrometer-nuggets in these experiments (e.g., Figure 4.17) compared to experiments in Fe-free systems (Borisov et al., 1994; Borisov and Palme, 1995 ) in which nugget formation apparently did not occur in experiments saturated with HSE. However, the correlation of Au and Pd concentrations with increasing oxidation state (0.52 ± 0.08 ppm in reduced experiments to 4.7 ± 0.9 in oxidized experiments for Au; 0.63 ± 0.31 ppm to 11.9 ± 1.2 ppm for Pd) is comparable to that estimated by Borisov and Palme (2000) (0.2 ppm at FMQ-2 to 2 ppm at FMQ+2 for Au; 1.6 ppm to 9 ppm for Pd). This is consistent with these two metals dissolving as oxides as proposed by Borisov and Palme (2000).

In contrast, Ir and Pt behaved differently in my experiments compared to the Fe-free experiments conducted by Borisov and Palme (2000). Iridium concentrations were roughly one order of magnitude higher (from 70 to 240 ppb Ir in my experiments vs. 2 to 18 ppb in Borisov and Palme, 2000). Platinum showed the most significant differences, the Pt concentrations in my experiments being up to 1000 times higher than in Fe-free experiments (1.2 to 1.6 ppm in my runs vs. 2.1 to 85 ppb in Borisov and Palme, 2000). In addition, neither Ir nor Pt concentrations showed the positive correlation with increasing oxidation state documented for the Fe-free experiments (Borisov and Palme, 2000). On the contrary, the concentration of Ir in oxidized experiments in this dissertation was smaller than the Ir concentration in the glass in reduced experiments.
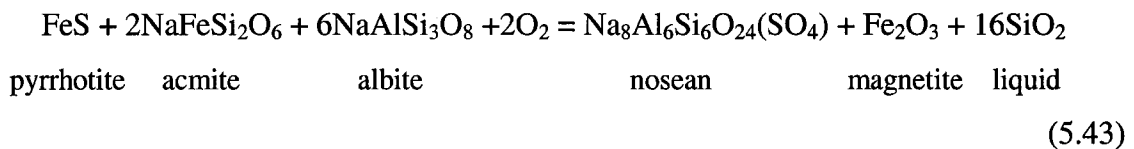
132

The critical question is whether these nuggets would form under natural conditions. The solubility data (in the melt) for the four HSE obtained in this work (Tables 4.11 and 4.12) are significantly higher than the estimated concentration of these metals in the mantle (1 to 7 ppb, McDonough and Sun, 1995). Thus, if sulfides are eliminated these HSE should be dissolved in the melt unless they are compatible in other phases. Capobianco et al. (1994) showed that in the absence of sulfide, Rh and Ru strongly partition into oxides, whereas Pd behaves as an incompatible element. Based on the similar behavior for the solubility of Pd and Au observed in my experiments coupled with their expected chalcophile behavior, I suggest that Au is likely to behave as an incompatible element as well. Regarding the behavior of Pt and Ir, the results of this work only show that they behave differently than Au and Pd. Based on their more siderophile behavior, one can speculate that they may behave in a similar way than Rh and Ru and partition preferentially into oxides, but otherwise the results of my experiments indicate that in the absence of sulfides, the four analyzed HSE would behave as incompatible elements.

### 5.5.2 Implications for the generation of gold-rich porphyry and epithermal deposits

Gold enrichment and high Au/Cu in porphyry and epithermal deposits has been attributed to oxidized conditions during partial melting of the mantle wedge, which favor incorporation of Au in the melt (Richards, 1995; Sillitoe, 1997). The results of the present work support this hypothesis. Oxidation in the mantle source would promote elimination of sulfides and increase Au and Pd solubility in the silicate melts. Sulfide elimination by oxidation, rather than by dissolution has the advantage that the oxidized magmas are less likely to saturate sulfides during magma evolution and fractionation, thus preserving ore metals until water-rich volatile phases are generated (Candela, 1992). Also, because sulfide precipitation is not only a function of oxidation state but also of sulfur concentration in the melt, sulfur removal during magma evolution by incorporation and fractionation of oxidized sulfur in crystalline phases (e.g., apatite, anhydrite, nosean) would enhance the probabilities of ore metals to remain as incompatible elements in a silicate melt. An example of sulfur removal is found in the phonolites associated with the

133

Au-rich Cripple Creek (Colorado) epithermal deposit. Lindgren and Ransome (1906) documented sodalite and nosean in the phonolites associated with this deposit. Based on textural relationships they concluded that "these two minerals were among the very first to crystallize from the phonolite magma and in consequence occur as inclusions in all the other important constituents, though they are not common in nepheline" (Lindgreen and Ransome, 1906, p. 62). They also concluded that the feldspathoids containing sulfur were haüyne ($(Na_6Ca_2(Al_6Si_6O_{24})(SO_4)_2)$), based on the presence of calcite in one decomposed crystal of nosean ($Na_8Al_6Si_6O_{24}(SO_4)$), and lack of calcite in the rest of the assemblage.

Low degrees of partial melting of an oxidized mantle source are also more consistent with the alkalic nature of some of the magmas related to Au-rich epithermal deposits, because of the incompatible nature of the alkalis in mantle mineral assemblages. The connection between some Au-rich epithermal deposits and alkalic magmatism is perhaps more related to the silica-undersaturated nature of these magmas, because silica-undersaturation favors sulfide oxidation at a given oxidation state. Stormer and Carmichael (1971) illustrated this using the reaction:

$$FeS + 2NaFeSi_2O_6 + 6NaAlSi_3O_8 + 2O_2 = Na_8Al_6Si_6O_{24}(SO_4) + Fe_2O_3 + 16SiO_2$$

pyrrhotite  acmite  albite  nosean  magnetite  liquid

$$(5.43)$$

but an analogous reaction, related to the equilibria discussed in section 5.1 and appropriate for the system described here, can be written as:

$$FeS^{sulfide} + Fe_2SiO_4^{ol} + 2O_2 = SO_2^{melt} + Fe_3O_4^{spl} + SiO_2^{melt} \qquad (5.44)$$
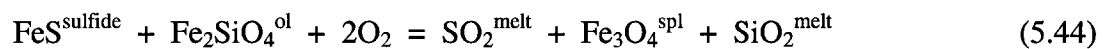
In both cases, at constant oxygen fugacity, a decrease in the silica activity pushes the reaction to the right, favoring the formation of sulfate at the expense of the pyrrhotite component in the sulfides. Therefore, the effect of sulfide oxidation for the generation of sulfide-undersaturated, Au-rich magmas is enhanced for silica-undersaturated melts.

134

### 5.5.3. Implications for the generation of orthomagmatic deposits

Changes in sulfur solubility with oxidation state may also have implications for the generation of orthomagmatic deposits. These deposits form when a sulfur-undersaturated magma attains sulfur saturation and the PGE are sequestered by the precipitated sulfides. The most currently accepted model for the generation of these deposits was summarized by Naldrett (1997, 1999). In this model, sulfide saturation is achieved either by assimilation of sulfur from the countryrock or by contamination of the mafic magmas with a felsic magma, which decreases the sulfur solubility in the mixed magma. The results of my work provide an additional mechanism: sulfide saturation can also be produced by reduction of a relatively oxidized magma by assimilation of reduced materials, with carbon being one of the most efficient reducing agents.

Carbon association with orthomagmatic deposits is well documented. In the Bushveld complex graphite is present in many reef sections (Ballhaus, 1988). In Stillwater, graphite is present as a film on cracks, grain boundaries, and cleavage surfaces (Mathez et al., 1989). In the Noril'sk region (Russia) the massive sulfides are developed at the base of the intrusion in contact with coal seams (Naldrett et al., 1996). Diakov et al. (2002) points out that the different intrusive units in the Noril'sk area normally occur within the basal portion of the flood basalts or within the coal-bearing sedimentary rocks, with some intrusions entirely hosted within them. In the Duluth complex, Acuri et al. (1998) related the sulfide mineralization to externally derived sulfur, mostly from the Virginia formation, which consists of intercalated pyritic, carbonaceous shales and graphitic argillite beds. Naldrett (1999) described the mineralized zones in Duluth as characterized by inclusions of country rock and the occurrence of up to 10% graphite in certain zones. In the Pechenga district (Russia), Barnes et al. (2001) described the massive sulfides as occurring at the contact between the ferropicrites and the country-rock, which contains sulfides and graphite and is referred to as black schist. They suggested that sulfides and carbon were extracted from the schist and acknowledged that sudden increase in sulfur concentration and decrease in $fO_2$ induced sulfide saturation in the magma. In the Voisey's Bay deposit, Brenan and Li (2000) document the presence of graphite as

135

inclusions in sulfides, and identified the carbon-bearing Tasiuyak gneiss as the source of carbon.

The initial oxidation state of the magmas associated with orthomagmatic deposits is difficult to constrain because of serpentinization, alteration and re-equilibration of their mineral assemblages. In addition, if sulfide precipitation is caused by a decrease in the oxidation state of the system, estimates of the oxidation state in areas containing sulfides would reflect the reduced assemblage (unless sulfide precipitation occurs after fractionation of the phases used for estimation of oxidation state). Estimates for the oxidation state of rocks in the Bushveld Complex, for example, are variable and inconsistent. Snethlage and Klemm (1978) provide estimates that range from $\log fO_2 = 10^{-5}$ to $10^{-8.6}$ whereas Elliot et al. (1982) estimated ranges from $fO_2 = 10^{-11}$ to $10^{-15.6}$. In the first case, temperatures range from 1120 °C to 1237 °C, and in the second the values are reported relative to T = 1150 °C. For comparison, the $fO_2$ of the FMQ buffer at 1150 °C and 500 MPa is $fO_2 = 10^{-7.92}$. Thus, the results of Snethlage and Klemm (1978) indicate that the oxidation state of the magmas are slightly above FMQ whereas the results of Elliot et al. (1982) would put them at oxidation states as low as FMQ-7 (conditions under which metallic iron should be present).

No direct estimates of the oxidation state of the rock at Noril'sk are available, but the composition of the spinels from the Noril'sk and Talnakh Intrusions (Barnes and Kunilov, 2000) range from Ti-enriched chromites to aluminous magnetite. The high $Fe^{3+}$ content in these spinels is consistent with spinel equilibration at a high oxidation state. Barnes and Kunilov (2000) explain the high $Fe^{3+}$ content in the Noril'sk-Talnakh spinels by "sulfate-assimilation, followed by extraction of S due to combination with Fe, Ni, and Cu in immiscible sulfide liquid" which "may have resulted in extensive oxidation of the silicate melt component" (Barnes and Kunilkov, 2000, p.1707). However, their work shows that spinel occurs predominantly as inclusions in silicate phases, whereas the sulfides are interstitial. These textural relationships are more supportive of precipitation of spinels with high $Fe^{3+}$ content at high oxidation states first, followed by reduction of the system and precipitation of interstitial sulfides. This interpretation is consistent with

the sulfur being assimilated from the evaporites and reduced to form sulfide by assimilation of graphite, in the same manner as sulfate-bearing experiments produced sulfides in graphite-bearing experiments (e.g., Figure 4.20).

Brenan and Li (2000) estimated oxygen fugacities in different sulfide segregations from the Voisey's Bay intrusion using Fe-Ni content in olivine and sulfides. They obtained oxygen fugacities that range from $\log fO_2 = -10.4$ to $-12.4$ (for reference, at 1200 °C and 500 MPa, $\log$ FMQ $= -7.3$). They modeled the change in oxidation state expected for reduction (by graphite assimilation) of a magma initially at FMQ and found that the final oxidation state was consistent with their measurements. They concluded that "assimilation of graphite by an oxidized magma at high temperature, then closure at lower temperature, can account for both the absolute values and variations in $fO_2$ exhibited by the Voisey's Bay samples" (Brenan and Li, 2000, p. 913).

Based on the results of this dissertation and the work of Barnes and Kunilov (2000) and Brenan and Li (2000), I suggest that the presence of externally-derived graphite in orthomagmatic ore deposits is evidence of a critical process in the generation of these deposits. This critical process is the precipitation of sulfides by abrupt reduction of an oxidized magma. If this is true, a potential tool for the exploration of these deposits is the identification of contacts between mafic intrusions and reduced country rocks. Detailed estimates of the oxidation state of mineral assemblages in orthomagmatic deposits and comparison with the oxidation state of barren mineral assemblages from the same intrusive suites should be able to test this hypothesis.

## 5.5.4. Implications for high-S volcanic degassing

An outstanding problem in the explanation of high-sulfur volcanic degassing known as the "excess sulfur" problem results from the poor correlation between the amount of $SO_2$ released and the amount of sulfur dissolved in the magma prior to eruption. This "excess" sulfur, which is characteristic of explosive eruptions of intermediate and felsic volcanoes

137

in subduction settings, has been attributed to the coexistence of the silicate melt with S-rich volatile phases (Wallace, 2001).

One of the most studied volcanic events is the S-rich eruption of Mount Pinatubo in 1991. Recent estimates of the oxidation state of the basalts associated to the Pinatubo eruption (deHoog et al., 2003) based on Cr-spinel-bearing olivine yield NNO+1.4 (~FMQ+2.1). These estimates and the lack of a "sulfur solubility minimum" as discussed in section 5.3.1 disprove the hypotheses of mixing of reduced basaltic magma with oxidized dacitic magma (Hattori, 1993; Kress, 1997) as a mechanism for the high-sulfur release in the 1991 eruption of Pinatubo. The models presented here for sulfur dissolution during partial melting as a function of oxidation state (Figure 5.11) indicate that at FMQ+2.1 no sulfide phases are present and all available sulfur is dissolved in the melt. Melt inclusions in amphiboles interpreted to have grown during mixing of the basaltic and dacitic magmas contain >1700 ppm sulfur (deHoog et al. 2003). Metrich et al. (1999) and deHoog et al. (2001) measured sulfur concentrations in basaltic glasses from melt inclusions in olivine in subduction zones as high as 3000 ppm, and Wallace (2002) measured up to 6000 ppm S in olivine-hosted melt inclusions from cinder cones associated with Popocatepetl volcano (Mexico). These high sulfur contents in basaltic melts are consistent with the high sulfur solubilities of basaltic melts in oxidized systems presented in this dissertation.

The results from Carroll and Rutherford (1987) (summarized here in Figure 5.10) show that at 200 MPa (a pressure consistent with shallow magma chambers) the solubility of sulfur, at 1025 °C and FMQ+2, is [S] $\approx$ 1000 ppm. The models presented in this dissertation for sulfur solubility in basaltic melts (Figure 5.12) show that at FMQ+2 the amount of sulfur that can be dissolved in the melt is much larger. Although the effect of pressure was not investigated in this dissertation, the work of Carroll and Rutherford (1987) and Luhr (1990) show that sulfur solubility in silicate melts decreases with decreasing pressure (i.e., sulfur solubility has the same pressure dependency as does water solubility). Based on the results of this work I propose a simple mechanism for the sulfur enrichment in the Pinatubo magmas and the high sulfur release: decompression and

138

cooling of a sulfur-rich basaltic melt as it ascended and mixed with the overlying hydrous dacitic magma. Because sulfate sulfur partitions preferentially into a hydrous phases (Keppler, 1999), water exsolution would strip the hybrid melt (andesitic in the case of Mount Pinatubo) of most of its sulfur and partition it into the vapor phase. Aside from the implications for sulfur-rich degassing, other consequences include the fact that the measured concentrations in the silicate melt (after the exsolution and degassing) would not be a reliable indicator of the initial sulfur concentrations in the magmas.

# 6. Summary and Conclusions

The solubility and speciation of sulfur, and the solubility of Pd, Ir, Pt, and Au under sulfide- and sulfate-saturated conditions in basaltic melts at 1300-1355 °C and 1.0 to 1.2 GPa was investigated. The results of this work provide the first experimental data on the speciation and solubility of sulfur in basaltic melts at oxidation states similar to those inferred for oxidized island arcs (~FMQ+2). This work also provides the first experimental data on the variations in Pd, Ir, Pt, and Au solubility in Fe-bearing basaltic melts as a function of oxidation state.

At the conditions of the experiments, both sulfide and sulfate were present as immiscible liquids forming spherical blebs within the basaltic melt and producing pyrrhotite and calcium-rich sulfate upon quenching. The sulfur solubility in sulfide-bearing melts, estimated from 13 sulfide-bearing experiments, was [S] = 0.14 ± 0.02, which is consistent with previous estimates of sulfur solubility under reduced conditions (e.g., ~1300 ppm or 0.13 wt% using the equations derived by Poulson and Ohmoto, 1990). The sulfur solubility in sulfate-bearing melts, estimated from eight sulfate-bearing experiments, was [S] = 1.5 ± 0.2 wt.%. These results indicate that, at constant pressure and temperature, oxidation of sulfides to sulfates and dissolution of sulfur as sulfate species in a basaltic melt increases sulfur solubility by a factor of ~10.

The $fO_2$ at which the transformation of sulfide to sulfate occurred could not be determined with precision, but the results of the experiments require that complete sulfide elimination and maximum sulfur solubility be obtained by ~ FMQ + 2.

Sulfur speciation for sulfate-saturated experiments was estimated at $X(S^{6+})$ = 0.81 ± 0.06 (n = 8) and is consistent with estimations of sulfur speciation in basalts and basaltic andesites from Lascar volcano and Cerro Overo (Matthews et al., 1999). These values are lower than expected if sulfur is present as sulfate ($S^{6+}$) in which case $X(S^{6+})$ = 1. Based on these results, the discrepancies between the measured and the expected values for $X(S^{6+})$ can be explained if sulfur is dissolved in the melt as sulfite ($S^{4+}$) or if the

140

assumption that the change in speciation is linear with the shift in SKα is not valid. Future work, using more precise techniques for estimation of speciation (e.g., XANES), could help constrain the speciation of sulfur in sulfate-saturated basaltic melts.

Compilation of data from this work and other available data on sulfur speciation as a function of oxidation state in basaltic melts was used to generate an equation (5.30) that relates sulfur speciation in the melt with the oxidation state of the system. This equation provides a more appropriate fit to the data from basaltic systems than the models of Wallace and Carmichael (1994) and Matthews et al. (1999), although the differences among the three models are rather small.

A linear regression (equation 5.34) of equation 5.32 (solved for ΔFMQ) could be used for preliminary estimations of the oxidation state of basaltic glasses from $X(S^{6+})$ estimates in the range $0.2 < X(S^{6+}) < 0.7$, but more direct methods (e.g., olivine-orthopyroxene-spinel equilibria) are recommended when possible. Additional independent estimations of oxidation state and sulfur speciation are needed to test the validity of equation 5.34, before using this function with confidence.

The data obtained in this work for sulfur solubility under sulfide-saturation (minimum solubility) and sulfate-saturation (maximum solubility) were used to generate three models for the change in sulfur solubility as a function of oxidation state. The three models share the same boundary conditions for minimum and maximum solubility and differ in the parameters used to constrain the range in oxidation state in which the change in solubility takes place. The first model (equation 5.37) assumes that sulfur solubility mirrors sulfur speciation (equation 5.32) and, therefore, uses some of the same parameters. The second model (equation 5.38) assumes that sulfides need to be eliminated before the effect of speciation as sulfate affects sulfur solubility and used data from Carroll and Rutherford (1985, 1987) to help constrain the oxidation state for the onset of the increase in sulfur solubility. The third model (equation 5.39) provides the limiting case, in which the increase in sulfur solubility occurs over a very narrow range in oxidation state.

141

The differences in the three models emphasize the need of additional experimental data in the range $0 < \Delta FMQ < 2$ to understand how oxidation state affects sulfur solubility, although model 2 (with more experimental constraints) constitutes the preferred model at this point.

The three models of sulfur solubility as a function of oxidation state were used to estimate the degree of partial melting required to produce sulfur-undersaturated basaltic melts in supra-subduction zone settings (where P and T are consistent with those of this study). The results show that, over the range of oxidation states prevalent in arc settings, the increase in sulfur solubility with oxidation state results in a decrease in the degree of partial melting needed to produce sulfur-undersaturated melts. Therefore, reasonably low melt fractions (~0.15) could produce sulfur-undersaturated basaltic melts, depending on the initial sulfur content and oxidation state in the source. These results avoid the need for large degrees of partial melting (e.g., Keays, 1995) or two-stage melting processes (e.g., Wyborn and Sun, 1994) to eliminate sulfide and produce HSE enrichments in mantle sources.

As a complement for the behavior of sulfur, the solubilities of Pd, Ir, Pt and Au in the experiments were also measured. The solubilities of Pd and Au in oxidized and sulfate-saturated experiments (Pd = $11.9 \pm 1.2$ ppm; Au = $4.7 \pm 0.9$ ppm) were significantly higher that the solubilities of those metals in sulfide-saturated melts (Pd = $0.63 \pm 0.31$ ppm; Au = $0.52 \pm 0.08$ ppm). For Pt, the solubility was similar in sulfide and sulfate saturated experiments (Pt = $1.23 \pm 0.46$ and Pt = $1.6 \pm 0.3$ ppm, respectively), whereas Ir solubility behaved opposite to Pd and Au, being more soluble in reduced than in oxidized melts (Ir = $0.24 \pm 0.08$ and Ir = $0.07 \pm 0.02$ ppm, respectively).

In addition to being dissolved in the melt, the four HSE were also present in all experiments as nuggets randomly dispersed throughout the glass and showing no apparent correlation with sulfides, oxides or silicates. Comparisons with the Fe-free experiments of Borisov and Palme (2000), in which nugget formation was less

142

problematic, indicate that nugget nucleation is correlated to the presence of FeO in the melt.

The textures observed in sulfide-saturated experiments demonstrate the differences in chemical affinities of the four HSE studied. Palladium showed a marked chalcophile behavior being incorporated in an immiscible sulfide liquid and quenching to form a Pd-rich sulfide. Gold, was relatively inert not showing strong chalcophile or siderophile behavior, but this can be related to the Cu-poor nature of the system studied, because Au has been shown to have marked chalcophile behavior in Cu-rich systems (Jugo et al., 1999). Pt and Ir showed strong siderophile behavior relative to Pd and Au, being preferentially hosted in Pt-Ir-Fe alloys.

The results of this work support the hypothesis that oxidation of mantle sulfides in supra-subduction zone settings favors Au-enrichment in the generated magmas, which translates to potentially higher Au-content in associated porphyry and epithermal deposits. Oxidized melts are not only Au-rich relative to sulfide-saturated magmas but also, because of their high oxidation state, are less likely to precipitate sulfides during magma evolution enhancing the chances of derived magmas to retain Au until the magmas reach shallow levels, where they can form volatile phases that incorporate the Au.

The results of this work also show that reduction of a relatively oxidized melt can be produced by assimilation of carbon, which forces the oxidation state to very low (reducing) values. The ubiquitous occurrence of externally derived graphite in orthomagmatic deposits, the presence of $Fe^{3+}$-rich spinels in assemblages from the Noril'sk areas, and the variations of oxidation state documented in the Voisey's Bay deposit are consistent with a model in which sulfide saturation is triggered by graphite assimilation into an originally oxidized melt. Evaluation of this hypothesis is difficult because of the difficulties in the estimation of the oxidation state in the associated magmas or by the wide discrepancies that they produce. However, studies aimed to constraining graphite occurrence in mineralized and barren intrusions, and detailed

143

studies on the variations of oxidation state (e.g., Brenan and Li, 2000) should be able to test this hypothesis. If graphite contamination is the trigger for sulfide precipitation in orthomagmatic systems, identification of the contact of the intrusive with reduced, graphite-bearing lithologies could be used as an exploration tool for these deposits. Finally, the high sulfur solubility measured in oxidized basaltic melts at relatively high pressure and temperatures coupled with the expected decrease in solubility with decompression can help explain the causes of high-sulfur degassing in some arc-related volcanoes. A model for the Pinatubo eruption in which oxidized, water- and sulfur-rich basaltic magma mixes with an oxidized dacitic magma could result in the generation of a sulfur-rich volatile phase to account for the "excess sulfur" problem, but in contrast to other proposed models, the trigger for sulfur saturation is the decrease in sulfur solubility that results from decompression.

# 7. References

Arcuri, T., Ripley, E.M., and Hauck, S.A., 1998, Sulfur and oxygen isotopes studies of the intersection between pelitic xenolith and basaltic magma at the Babbitt and Serpentine Cu-Ni deposits, Duluth Complex, Minnesota: Economic Geology, v. 93, p. 1063-1075.

Alard, O., Griffin, W.L., Lorand, J.-P., Jackson, S.E., and O'Reilly, S.Y., 2000, Non-chondritic distribution of the highly siderophile elements in mantle sulphides: Nature, v. 407, p. 891-894.

Alard, O., Griffin, W.L., Pearson, N.J., Lorand, J.-P., and O'Reilly, S.Y., 2002, New insights into the Re-Os systematics of sub-continental lithospheric mantle from in situ analysis of sulphides: Earth and Planetary Science Letters, v. 203, p. 651-663.

Alt, J.C., Shanks, W.C.III, and Jackson, M.C., 1993, Cycling of sulfur in subduction zones: The geochemistry of sulfur in the Mariana Island Arc and back-arc trough: Earth and Planetary Science Letters, v. 119, p. 477-494.

Anderson, G.M., and Crerar, D.A., 1993, Thermodynamics in Geochemistry: The equilibrium model, Oxford University Press, pp. 588.

Arculus, R.J., Johnson, R.W., Chappell, B.W., McKee, C.O., and Sakai, H., 1983, Ophiolite-contaminated andesites, trachybasalts, and cognate inclusions of Mount Lamington, Papua New Guinea: Anhydrite-amphibolite lavas and the 1951 cumulodome: Journal of Volcanology and Geothermal Research, v. 18, p. 215-247.

Baker, L.L., and Rutherford, M.J., 1996a, Crystallization of anhydrite-bearing magmas: Transaction of the Royal Society of Edinburgh: Earth Sciences, v. 87, p. 243-250.

Baker, L.L., and Rutherford, M.J., 1996b, Sulfur diffusion in rhyolite melts: Contributions to Mineralogy and Petrology. Petrology, v. 123, p. 335-344.

Ballhaus, C.G., 1988, Potholes of the Merensky Reef at Brakspruit Shaft, Rustenburg platinum mines; primary disturbances in the magmatic stratigraphy: Economic Geology, v. 83, p. 1140-1158.

Ballhaus, C., 1993, Redox states of lithospheric and asthenospheric upper mantle: Contributions to Mineralogy and Petrology, 114, p. 331-348.

Ballhaus, C., and Frost, B.R., 1994, The generation of oxidized CO2-bearing basaltic melts from reduced CH4-bearing upper mantle sources: Geochimica et Cosmochimica Acta, v. 58, p. 4931-4940.

Ballhaus, C., and Sylvester, P., 2000, Noble Metal Enrichment Processes in the Merensky Reef, Bushveld Complex: Journal of Petrology, v. 41, p. 545-561.

Ballhaus, C., Berry, R.F., and Green, D.H., 1990, Oxygen fugacity controls in the Earth's upper mantle: Nature, v. 348, p. 437-440.

Ballhaus, C., Berry, R.F., and Green, D.H., 1991, High-pressure experimental calibration of the olivine-orthopyroxene-spinel oxygen geobarometer: implications for the oxidation state of the upper mantle: Contributions to Mineralogy and Petrology, v. 107, p. 27-40.

Barnes, S.J., Kunilov, 2000, Spinels and Mg ilmenites from the Noril'sk 1 and Talnakh intrusions and other mafic rocks of the Siberian Flood Basalt province: Economic Geology, v. 95, p. 1701-1717.

Barnes, S-J., Melezhik, V.A., and Sokolov, S.V., 2001, The composition and mode of formation of the Pechenga nickel deposits: Canadian Mineralogist, v. 39, p. 447-471.

Barnes, S-J., Naldrett, A.J., and Gorton, M.P., 1985, The origin of the fractionation of platinum-group elements in terrestrial magmas: Chemical Geology, v. 53, p. 303-323.

Barth, A.P., and Dorais, M.J., 2000, Magmatic anhydrite in granitic rocks: First occurrence and potential petrologic consequences: American Mineralogist, v. 85, p. 430-435.

Bezmen, N.I., Asif, M., Bregmann, G.E., Romanenko, I.M., and Naldrett, A.J., 1994, Distribution of Pd, Rh, Ir, Os, and Au between sulfide and silicate melts: Geochimica et Cosmochimica Acta., v. 58, p. 1251-1260.

Bohlen, S.R., 1984, Equilibria for precise pressure calibration and a frictionless furnace assembly for the piston-cylinder apparatus: Neues Jahrbuch Mineralogie Monatshefte, 9, p. 404-412.

Borisov, A., and Palme, H., 1995, The Solubility of iridium in silicate melts: New data from experiments with $Ir_{10}Pt_{90}$ alloys: Geochimica et Cosmochimica Acta, v. 59, p. 481-485.

Borisov, A., and Palme, H., 2000, Solubilities of noble metals in Fe-containing silicate melts as derived from experiments in Fe-free systems: American Mineralogist. v. 85, p. 1665-1673.

Borisov, A., Palme, H., and Spettel, B., 1994, Solubility of Pd in silicate melts: Implications for core formation in the Earth: Geochimica et Cosmochimica Acta, v. 58, p. 705-716.

Boyd, F.R., and England, J.L., 1960, Apparatus for phase-equilibrium measurements at pressures up to 50 kilobars and temperatures up to 1750 °C: Journal of Geophysical Research, v. 65, p. 741-748.

Brenan, J.M., and Li, C., 2001, Constraints on oxygen fugacity during sulfide segregation in the Voisey's Bay Intrusion, Labrador, Canada: Economic Geology, v. 95, p. 901-915.

Brey, G.P., Köhler, T., and Nickel, 1990, Geothermobarometry in four-phase lherzolites I. Experimental results from 10 to 60 kbar. Journal of Petrology, v. 31, p. 1313-1352..

Candela, P.A., 1992, Controls on ore metal ratios in granite-related ore systems: An experimental and computational approach: Transactions of the Royal Society of Edinburgh, v.83, p. 317-326.

Canil, D., Virgo, D., and Scarfe, C.M., 1990, Oxidation state of mantle xenoliths from British Columbia, Canada: Contributions to Mineralogy and Petrology, v. 104, p. 453-462.

Capobianco, C.J., Hervig, R.L., and Drake, M.J., 1994, Experiments on crystal/liquid partitioning of Ru, Rh and Pd for magnetite and hematite solid solutions crystallized from silicate melt: Chemical Geology, v. 113, p. 23-43.

Carmichael, I.S.E., 1991, The redox state of basic and silicic magmas: a reflection of their source regions?: Contributions to Mineralogy and Petrology, v. 106, p. 129-141.

Carroll, M.R., and Rutherford, M.J., 1985, Sulfide and sulfate saturation in hydrous silicate melts: Journal of Geophysical Research, v. 90, p. C601-C612.

Carroll, M.R., and Rutherford, M.J., 1987, The Stability of igneous anhydrite: Experimental results and implications for sulfur behavior in the 1982 El Chichón trachyandesite and other evolved magmas: Journal of Petrology, v. 28, p. 781-801.

Carroll, M.R., and Rutherford, M.J., 1988, Sulfur speciation in hydrous experimental glasses of varying oxidation state: Results from measured wavelength shifts of sulfur X-rays: American Mineralogist, v. 73, 845-849.

Chappell, B.W., and White, A.J.R., 1968, The x-ray spectrographic determination of sulfur coordination in scapolite: American Mineralogist, v. 53, p. 1735-1738.

Chou, I-M., 1987, Oxygen buffer and hydrogen sensor techniques at elevated pressures and temperatures. In: Ulmer, G.C., and Barnes, H.L., (eds.), Hydrothermal Experimental Techniques, p. 61-99.

Chou, I-M., 1997, The use and misuse of the $H_2$ sensors: a discussion of the paper by Dachs (1994): Contributions to Mineralogy and Petrology, v. 128, p. 302-305.

Christie, D.M., Carmichael, I.S.E., and Langmuir, C.H., 1986, Oxidation states of mid-ocean ridge basalt glasses: Earth and Planetary Science Letters, v. 79, p. 397-411.

Craig, J. R., and Kullerud, G, 1969, Phase relations in the Cu-Fe-Ni-S system and their application to magmatic ore deposits: In: Magmatic Ore Deposits: A Symposium, H.D.B. Wilson (ed), Economic Geology Monograph 4, p. 344-358.

De Hoog, J.C.M., Mason, P.R.D., and van Bergen, M.J., 2001, Sulfur and chalcophile elements in subduction zones: Constraints from a laser ablation ICP-MS study of melt inclusions from Galunggung Volcano, Indonesia: Geochimica et Cosmochimica Acta, v. 65, p. 3147-3164.

De Hoog, J.C.M., Hattori, K.H., and Hoblitt, R.P., 2003, Oxidized, sulfur-rich mafic magma at Mount Pinatubo, Philippines: Geophysical Research Abstracts, v. 5, 01660.

Diakov, S., West, R., Schissel, D., Krivtsov, A., Kochnev-Pervoukhov, V., and Migachev, I., 2002, Recent advances in the Noril'sk model and its application for exploration of Ni-Cu-PGE sulfide deposits: Society of Economic Geology, Special Publication 9, p. 203-226.

Droop, G.T.R., 1987, A general equation for estimating $Fe^{3+}$ concentrations in ferromagnesian silicates and oxides from microprobe analyses, using stoichiometric criteria: Mineralogical Magazine, v. 51, p. 431-435.

Dunn, T., 1993, The piston-cylinder apparatus: Mineralogical Association of Canada Short Course Handbook, v. 21, p. 39-94.

Elliot, W.C., Grandstaff, D.E., Ulmer, G.C., Buntin, T., and Gold, D.R., 1982, An intrinsic oxygen fugacity study of platinum-carbon associations in layered intrusions: Economic Geology, v. 77, p. 1493-1510.

Fincham, C.J.B., and Richardson, F.D., 1954, The behaviour of sulphur in silicate and aluminate melts: Proceeding of the Royal Society of London, v. 223A, p. 40-61.

Fournelle, J., 1990, Anhydrite in Nevado del Ruiz November 1985 pumice: relevance to the sulfur problem: Journal of Volcanology and Geothermal Research, v. 42, p. 189-201.

Gaetani, G.A., and Grove, T.L., 1998, The influence of water on melting of mantle peridotite: Contributions to Mineralogy and Petrology, v. 131, p. 323-346.

Garuti, G., Oddone, M., and Torres-Ruiz, J., 1997, Platinum-group-element distribution in subcontinental mantle: Evidence from the Ivrea Zone (Italy) and the Betic-Rifean cordillera (Spain and Morocco): Canadian Journal of Earth Sciences, v. 34: 444-463.

Gerlach, T.M, Westrich, H.R., and Symonds, R.B., 1996, Preeruption vapor in magma of the climactic Mount Pinatubo eruption; source of giant stratospheric sulfur dioxide cloud, In: Fire and mud; eruptions and lahars of Mount Pinatubo, Philippines, C.G. Newhall and R.S. Punongbayan, (eds.), p. 415-433.

Goldsmith, J.R., and Newton, R.C., 1977, Scapolite-plagioclase stability relations at the high pressures and temperatures in the system $NaAlSi_3O_8-CaAl_2Si_2O_8-CaCO_3-CaSO_4$: American Mineralogist, v. 62, p. 1063-1981.

Grove, T.L., 1981, Use of Fe-Pt alloys to eliminate the iron loss problem in 1 atmosphere gas mixing experiments: Theoretical and practical considerations, Contribution to Mineralogy and Petrology, v. 78, p. 298-304.

Gurenko, A.A., and Schmincke, H.-U., 1998, Petrology, geochemistry, S, Cl, and F abundances, and S oxidation state of sideromelane glass shards from Pleistocene ash layers north ands south of Gran Canaria (ODP Leg 157): Contributions to Mineralogy and Petrology, v. 131, p. 95-110.

Gurenko, A.A., and Schmincke, H.-U., 2000, S concentrations and its speciation in Miocene basaltic magmas north and south of Gran Canaria (Canary Islands): Constraints from glass inclusions in olivine and clinopyroxene: Geochimica et Cosmochimica Acta, v. 64, p. 2321-2337.

Hattori, K.H., 1993, High-sulfur magma, a product of fluid discharge from underlying mafic magma: Evidence from Mount Pinatubo, Philippines: Geology, v. 21, p. 1083-1086.

Hattori, K.H., De Hoog, J.C.M., Keith, J.D., 2002, Role of oxidized, sulfur-rich mafic magmas for porphyry copper mineralization: GSA annual meeting, Abstracts with Programs.

Holloway, J.R., Pan, V., and Gudmundsson, G., 1992, High-pressure fluid-absent melting experiments in the presence of graphite: oxygen fugacity, ferric/ferrous ratio and dissolved $CO_2$: European Journal of Mineralogy, v. 4, p. 105-114.

Holzheid, A., and Grove, T.L., 2002, Sulfur saturation limits in silicate melts and their implications for core formation scenarios for terrestrial planets: American Mineralogist, v. 87, p. 227-237.

Huebner, J.S., and Sato, M., 1970, The oxygen fugacity-temperature relationships of manganese oxide and nickel oxide buffers: American Mineralogist, v. 55, p. 934-952.

Jaques, A.L., and Green, D.H., 1980, Anhydrous melting of peridotite at 0-15 kbar pressure and the genesis of tholeiitic basalts: Contributions to Mineralogy and Petrology, v. 73, p. 287-310.

Jugo, P.J., Candela, P.A., and Piccoli, P.M., 1999, Magmatic sulfides and Au:Cu ratios in porphyry deposits: An experimental study of copper and gold partitioning at 850 °C, 100 MPa in a haplogranitic melt-pyrrhotite-intermediate solid solution-gold metal assemblage, at gas saturation., In: Granites; crustal evolution and associated mineralization. A.N. Sial; W.E. Stephens and V.P. Ferreira (Eds.): Lithos, v. 46, p. 573-589.

Katsura, T., and Nagashima, S., 1974, Solubility of sulfur in some magmas at 1 atmosphere: Geochimica et Cosmochimica Acta, v. 38, p. 517-531.

Keays, R.R., 1995, The role of komatiitic and picritic magmatism and S-saturation in the formation of ore deposits: Lithos, v. 34, p. 1-18.

Keith, J.D., Christiansen, E.H., Maughan, D.T., and Waite, K.A., 1998, The role of mafic alkaline magmas in felsic porphyry Cu and Mo systems: Mineralogical Association of Canada Short course, v. 26, p. 211-243.

Keppler, H., 1999, Experimental evidence for the source of excess sulfur in explosive volcanic eruptions: Science, v. 284, p. 1652-1654.

Kilinc, A. Carmichael, I.S.E., Rivers, M.L., and Sack, R.O., 1983, The ferric-ferrous ration of natural silicate liquids equilibrated in air: Contribution to Mineralogy and Petrology, v. 83, p. 136-140.

Košler, J., 2001, Laser-ablation ICPMS study of metamorphic minerals and processes: In P.J. Sylvester (ed.) Laser-ablation ICPMS in the earth sciences: Principles and applications, Mineralogical Association of Canada, Short Course Series v. 29, p. 185-202.

Kress, V.C., 1997, Magma mixing as a source for Pinatubo sulphur: Nature, v. 389, p. 591-593.

Kress, V.C., and Carmichael, I.S.E., 1991, The compressibility of silicate liquids containing Fe (sub 2) O (sub 3) and the effect of composition, temperature, oxygen fugacity and pressure on their redox states: Contributions to Mineralogy and Petrology, v. 108, p. 82-92.

Kucha, H., Wouters, R., Arkens, O., 1989, Determination of sulfur and iron valence by microprobe: Scanning Microscopy, v. 3, p. 89-97.

Kushiro, I., 1976, A new furnace assembly with a small temperature gradient in solid-media, high-pressure apparatus. Carnegie Institution of Washington Yearbook, v. 68, p. 231-233.

Le Maitre, R.W. (ed.), 2002, Igneous rocks: A classification and glossary of terms: Recommendations of the International Union of Geological Sciences Subcommission on the systematics of igneous rocks (2nd ed.), Cambridge University Press, pp. 240.

Li, D., Bancroft, G.M., and Kasrai, M., 1995, A K- and L-edge X-ray absorption spectroscopy of metal sulfides and sulfates: Applications in mineralogy and geochemistry: Canadian Mineralogist, v. 33, p. 949-960.

Lindgren, W., and Ransome, F.L., 1906, Geology and gold deposits of the Cripple Creek district, Colorado: USGS, Professional paper 54, pp. 516.

Longerich, H.P., Jackson, S.E., and Günther, D., 1996, Laser ablation inductively coupled plasma mass spectrometry transient signal data acquisition and analyte concentration calculation: Journal of Analytical Atomic Spectrometry, v. 11, p. 899-904.

Lorand, J-P., Pattou, L., and Gros, M., 1999, Fractionation of platinum-group elements and gold in the upper mantle: A detailed study in Pyrenean orogenic lherzolites: Journal of Petrology, v. 40, p. 957-981.

Luguet, A., Alard, O., Lorand, J.P., Pearson, N.J., Ryan, C., and O'Reilly, S.Y., 2001, Laser-ablation microprobe (LAM)-ICPMS unravels the highly siderophile element geochemistry of the oceanic mantle: Earth and Planetary Science Letters, v. 189, p. 285-294.

Luhr, J.F., 1990 Experimental phase relations of water- and sulfur-saturated arc magmas and the 1982 eruption of El Chichón volcano: Journal of Petrology,, v. 31, p. 1071-1114.

Luhr, J.F., Carmichael, I.S.E., and Varekamp, J.C., 1984, The 1982 eruptions of El Chichón volcano, Chiapas, Mexico: Mineralogy and petrology of the anhydrite -bearing pumice: Journal of Volcanology and Geothermal Research, v. 23, p. 69-108.

Luth, R.W., 1989, Natural versus experimental control of oxidation state : Effects on the composition and speciation of C-O-H fluids: American Mineralogist, v. 74, p. 50-57.

Luth, R.W., 1993a, Apparatus and techniques for experiments at mantle pressures: Mineralogical Association of Canada Short Course Handbook, v. 21, p. 1-13.

Luth, R.W., 1993b, Measurements and control of intensive parameters in experiments at high pressure in solid-media apparatus: Mineralogical Association of Canada Short Course Handbook, v. 21, p. 15-37.

Luth, R.W., 1999, Carbon and carbonated in the mantle: The Geochemical Society Special Publications 6, p., 297-316.

Luth, R.W., and Canil, D., 1993, Ferric iron in mantle-derived pyroxenes and a new oxybarometer for the mantle: Contributions to Mineralogy and Petrology, v. 113, p. 236-248.

Massalski, T.B. (ed.), 1986, Binary alloy phase diagrams, American Society for Metals, p. 2224.

Mathez, E.A., Dietrich, V.J., Holloway, J.R., and Boudrea, A.E., 1989, Carbon distribution in the Stillwater Complex and evolution of vapor during crystallization of Stillwater and Bushveld magmas: Journal of Petrology, v. 30, p, 153-173.

Matthews, S.J., Jones, A.P., and Beard, A.D., 1994, Buffering of melt oxygen fugacity by sulphur redox reactions in calc-alkaline magmas: Journal of the Geological Society, London, v. 151, p. 815-823.

Matthews, S.J., Jones, A.P., and Bristow, C.S., 1992, A simple magma-mixing model for sulphur behaviour in calc-alkaline volcanic rocks: mineralogical evidence from Mount Pinatubo 1991 eruption: Journal of the Geological Society, London, v. 149, p. 863-866.

Matthews, S.J., Moncrieff, D.H.D., and Carroll, M.R., 1999, Empirical calibration of the sulphur valence oxygen barometer from natural and experimental glasses: method and applications: Mineralogical Magazine, v. 63, p. 421-431.

Mattioli, G.S., and Bishop, F.C., 1984, Experimental determination of the chromium-aluminum mixing parameter in garnet: Geochimica et Cosmochimica Acta., v. 48, p. 1367-1371.

Mattioli, G.S., and Wood, B.J., 1988, Magnetite activities across the $MgAl_2O_4$-$Fe_3O_4$ spinel join, with applications to themobarometric estimates of upper mantle oxygen fugacity: Contributions to Mineralogy and Petrology, v. 98, p. 148-162.

Mavrogenes, J.A., and O'Neill, H.St.C., 1999, The relative effects of pressure, temperature and oxygen fugacity on the solubility of sulfide in mafic magmas: Geochimica et Cosmochimica Acta., v. 63, p. 1173-1180.

McDonough, W.F., and Sun, S.-s., 1995, The composition of the Earth: Chemical Geology, v. 120, p. 223-253.

McInnes, B.I.A., and Cameron, E.M., 1994, Carbonated, alkaline hybridizing melts from a sub-arc environment: Mantle wedge samples from the Tabar-Lihir-Tanga-Feni arc, Papua New Guinea: Earth Planetary Science Letters, v. 122, p. 125-141.

Metrich, N., and Clocchiatti, R., 1996, Sulfur abundance and its speciation in oxidized alkaline melts: Geochimica et Cosmochimica Acta, v. 60, p. 4151-4160.

Metrich, N., Schiano, P., Clocchiatti, R., and Maury, R.C., 1999, Transfer of sulfur in subduction settings: An example from Batan Island (Luzon volcanic arc, Philippines): Earth and Planetary Science Letters, v. 167, p. 1-14.

Mitchell, R.H., and Keays, R.R., 1981, Abundance and distribution of gold, palladium and iridium in some spinel and garnet lherzolites: implications for the nature and origin of precious metal-rich intergranular components in the upper mantle: Geochimica et Cosmochimica Acta, v. 45, p. 2425-2442.

Morgan, J.W., 1986, Ultramafic xenolith - Clues to Earth's late accretionary history: Journal of Geophysical Research, Solid Earth, v. 91, p. 2375-2387.

Müller, D., Franz, L., Herzig, P.M., and Hunt, S., 2001, Potassic igneous rocks from the vicinity of epithermal gold mineralization, Lihir Island, Papua New Guinea: Lithos, v. 57, p. 163-186.

Mungall, J.E., 2002, Roasting the mantle: Slab melting and the genesis of major Au and Au-rich Cu deposits: Geology, v. 30, p. 915-918.

Nagashima, S., and Katsura, T., 1973, The solubility of sulfur in $Na_2O$-$SiO_2$ melts under various oxygen partial pressures at 1100°C, 1250°C, and 1300°C: Bulleting of the Chemical Society of Japan, v. 46, p. 3099-3103.

Nair, R.K., 2000, Fluid-absent melting of high-grade semi-pelites : P-T constraints on orthopyroxene formation and implications for granulite genesis, Thesis (M.Sc.), University of Alberta, 2000.

Naldrett, A.J., 1997, Key factors in the genesis of Noril'sk, Sudbury, Jinchuan, Voisey's Bay and other world-class Ni-Cu-PGE deposits: implications for exploration: Australian Journal of Earth Sciences, v. 44, p. 283-315.

Naldrett, A.J., 1999, World-class Ni-Cu-PGE deposits: key factors in their genesis: Mineralium Deposita, v. 34, p. 227-240.

Naldrett, A.J., Fedorenko, V.A., Mohammed, A., Shushen, L., Kunilov, V.E., Stekhin, A.I., Lightfoot, P.C., and Gorbachev, N.S., 1996, Controls on the composition of Ni-Cu sulfide deposits as illustrated by those at Noril'sk, Siberia: Economic Geology, v. 91, p. 751-773.

Nilsson, K, and Peach, C.L., 1993, Sulfur speciation, oxidation state, and sulfur concentration in backarc magmas: Geochimica et Cosmochimica Acta, v. 57, p. 3807-3813.

O'Hara, M.J., Fry, N., and Prichard, H.M., 2001a, Minor phases as carriers of trace elements in non-modal crystals-liquid separation processes I: Basic relationships: Journal of Petrology, v. 42, p. 1869-1885.

O'Hara, M.J., Fry, N., and Prichard, H.M., 2001b, Minor phases as carriers of trace elements in non-modal crystals-liquid separation processes II: Illustration and bearing on behaviour of REE, U, Th and the PGE in igneous processes: Journal of Petrology, v. 42, p. 1887-1910.

O'Neill, H.St.C., and Wall, V.J., 1987, The olivine-orthopyroxene-spinel oxygen geobarometer, the nickel precipitation curve, and the oxygen fugacity of the earth's upper mantle: Journal of Petrology, v. 28, p. 1169-1191.

O'Neill, H.St.C., Dingwell, D.B., Borisov, A., Spettel, B, and Palme, H., 1995, Experimental petrochemistry of some highly siderophile elements at high temperatures, and some implications for core formation and mantle's early history: Chemical Geology, v. 120, p. 255-273.

Paris, E., Giuli, G., Carroll, M.R., and Davioli, I., 2001, The valence and speciation of sulfur in glasses by X-ray absorption spectroscopy: Canadian Mineralogist, v. 39, p. 331-339.

Parkinson, I.J., and Arculus, R.J., 1999, The redox state of subduction zones: insights from arc-peridotites: Chemical Geology, v. 160, p. 409-423.

Peach, C.L., Mathez, E.A., and Keays, R.R, 1990, Sulfide melt-silicate melt distribution coefficients for noble metals and other chalcophile elements as deducted from MORB: Implications for partial melting: Geochimica et Cosmochimica Acta, v. 54: 3379-3389

Poulson, S.R., and Ohmoto, H., 1990, An evaluation f the solubility of sulfide sulfur in silicate melts from experimental data and natural samples: Chemical Geology, v. 85, p. 57-75.

Rehkämper, M., Halliday, A.N., Alt, J., Fitton, J.G., Lee, D.-C., Wieneke, M., and Arndt, N.T., 1999a, Ir, Ru, Pt, and Pd in basalts and komatiites: New constraints for the geochemical behavior of the platinum-group elements in the mantle: Geochimica et Cosmochimica Acta, v. 63, p. 3915-3934.

Rehkämper, M., Halliday, A.N., Alt, J., Fitton, J.G., Zipfel, J., and Takazawa, E., 1999b, Non-chondritic platinum-group element ratios in oceanic mantle lithosphere: petrogenetic signature of melt percolation?: Earth and Planetary Science Letters, v. 172, p. 65-81.

Richards, J.P., 1995, Alkalic-type Epithermal Gold Deposits - A Review: In : Magmas, Fluids and Ore Deposits, J.F.H. Thompson (ed.). Mineralogical Association of Canada, Short Course Series. P: 367-400.

Richards, J.P., McCulloch, M.T., Chappell, B.W., and Kerrich, R., 1991, Sources of metals in the Porgera gold deposit, Papua New Guinea: Evidence from alteration, isotope, and noble metal geochemistry: Geochimica et Cosmochimica Acta, v. 55, p. 565-580.

Righter, K., and Drake, M.J., 1997, Metal-silicate equilibrium in a homogeneously accreting earth: new results for Re: Earth and Planetary Science Letters, v. 146, p. 541-553.

Righter, K., and Drake, M.J., 1999, Effect of water on metal-silicate partitioning of siderophile elements: a high pressure and temperature terrestrial magma ocean and core formation: Earth and Planetary Science Letters, v. 171, p. 383-399.

Robinson, J.C.A, Wood, B.J., and Blundy, J.D., 1998, The beginning of melting of fertile and depleted peridotite at 1.5 GPa: Earth and Planetary Science Letters, v. 155, p. 97-111.

Roeder, P.L., and Emslie, R.F., 1970, Olivine-liquid equilibrium: Contributions to Mineralogy and Petrology, v. 29, p. 275-289.

Roeder, P.L., Poustovetov, A., and Oskarson, N., 2001, Growth forms and composition of chromian spinel in MORB magma: Diffusion-controlled crystallization of chromian spinel: Canadian Mineralogist, v. 39, p. 397-416.

Sillitoe, R.H., 1997, Characteristics and controls of the largest porphyry copper-gold and epithermal gold deposits in the circum-Pacific region: Australian Journal of Earth Sciences, v. 44, p. 373-388.

Solomon, M., 1990, Subduction, arc reversals, and the origin of porphyry copper-gold deposits in island arcs: Geology, v. 18, p. 630-633.

Snethlage, R., and Klemm, D.D., 1978, Intrinsic oxygen fugacity measurements on chromites from the Bushveld Complex and their petrogenetic significance: Contributions to Mineralogy and Petrology, v. 67, p. 127-138.

Stormer, J.C., and Carmichael, I.S.E., 1971, The free energy of sodalite and the behavior of
chloride, fluoride and sulfate in silicate magmas: American Mineralogist, v. 56, p. 292-306.

Streck, M.J., and Dilles, J.H, 1998, Sulfur evolution of oxidized arc magmas as recorded in
apatite from a porphyry copper batholith: Geology, v. 26: 523-526.

Takahashi, E., 1980, Olivine/liquid nickel partitioning at high pressures: experiments with an
olivine capsule: Eos, v. 61, p. 397.

Tarkian, M., and Stribrny, B., 1999, Platinum-group elements in porphyry copper deposits: A
reconnaissance study: Mineralogy and Petrology, v. 65, p. 161-183.

Taylor, G.A., 1958, The 1951 eruption of Mount Lamington, Papua: Bureau of Mineral
Resources, Geology and Geophysics Bulletin, v.38, 117 pp.
(not seen, referenced in Arculus et al., 1983)

Teertstra, D.K., Schindler, M., Sherriff, B.L., and Hawthorne, F.C., 1999, Silvialite, a new
sulfate-dominant member of the scapolite group with an Al-Si composition near the I4/m-
P42/n phase transition: Mineralogical Magazine, v. 63, p. 321-329.

Tredoux, M., Lindsay, N.M., Davies, G., and McDonald, I., 1995, The fractionation of platinum-
group elements in magmatic systems, with the suggestion of a novel causal mechanism:
South African Journal of Geology, v. 98, p. 157-167.

Ulmer, P., and Luth, R.W., 1991, The graphite-COH fluid equilibrium in P, T, $fO_2$ space: An
experimental determination to 30 kbar and 1600 °C: Contributions to Mineralogy and
Petrology, v. 106, p. 265-272.

Vairavamurty, A., Manowitz, B., Luther, G.W. III, and Jeon, Y., 1993, Oxidation state of sulfur
in thiosulfate and implications for anaerobic energy metabolism: Geochimica et
Cosmochimica Acta, v. 57, p. 1619-1623.

Van der Laan, S.R., and van Groos, A.F.K., 1991, Pt-Fe alloys in experimental petrology applied
to high-pressure research on Fe-bearing systems: American Mineralogist, v. 76, p. 1940-
1949.

Wallace, P.J., 2002, Volatile constituents and vapor saturation: Integrating petrological and
remote sensing perspectives to understand magmatic volatile budgets: Eos Transactions,
AGU, 83(47), Fall meeting Supplement, Abstract V52D-13.

Wallace, P.J., 2001, Volcanic $SO_2$ emission and the abundance and distribution of exsolved gas in
magma bodies: Journal of Volcanology and Geothermal Research, v. 108, p. 85-106.

Wallace, P.J., and Carmichael, I.S.E., 1992, Sulfur in basaltic melts: Geochimica et
Cosmochimica Acta, v. 56, p. 1863-1874.

Wallace, P.J., and Carmichael, I.S.E., 1994, S speciation in submarine basaltic glasses as determined by measurements of SKα X-ray wavelength shifts: American Mineralogist, v. 79, p. 161-167.

Walter, M.J., and Presnall, D.C., 1994, Melting behavior of simplified lherzolite in the system CaO-MgO-Al$_2$O$_3$-SiO$_2$-Na$_2$O from 7 to 35 kbar: Journal of Petrology, v. 35, p. 329-359.

Winther, K.T., Watson, E.B., and Korenwosky, G.M., 1998, Magmatic sulfur compounds and sulfur diffusion in albite melt at 1 GPa and 1300-1500 °C: American Mineralogist, v. 83, p. 1141-1151.

Wood, B.J., Virgo, D., 1989, Upper mantle oxidation state: Ferric iron contents of lherzolite spinels by [57]Fe Mössbauer spectroscopy and resultant oxygen fugacities: Geochimica et Cosmochimica Acta, v. 53, p. 1277-1291.

Wulff-Pedersen, E., Neumann, E-R., Burke, E.A.J., Vannucci, R., Bottazzi, P., Ottolini, L., Gjønnes, J., and Hansen, V., 2000, Origin and structural character of haüyne$_{ss}$ in spinel dunite xenoliths from La Palma, Canary Islands: American Mineralogist, v. 85, p. 1397-1405.

Wyborn, D., and Sun, S.-S., 1994, Sulphur-undersaturated magmatism - a key factor for generating magma-related copper-gold deposits: AGSO Research Newsletter, November 1994, p. 7-8.

# Appendix A. Piston-cylinder pressure calibration

## A.1. Theoretical considerations

This section summarizes the pressure calibration of 19 mm diameter pressure assemblies that differ from assemblies previously used in this lab in that the composition of the pieces inside the graphite furnace are made of magnesium oxide (as determined by XRD) instead of Alsimag (an $Al_2O_3$-$SiO_2$-MgO ceramic). A thorough discussion on pressure calibration for the piston-cylinder apparatus can be found in Luth (1993b).
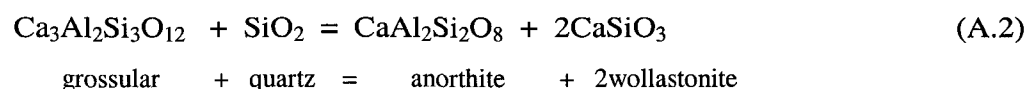
The nominal (ideal) pressure that the piston applies on the charge can be calculated by knowing the fluid pressure applied to the hydraulic ram (line pressure) and the ratio between the ram and the piston:

$$P_n = P_r \times (R_r / R_p)^2 \qquad\qquad (A.1)$$

were $P_n$ is the nominal pressure, $P_r$ is the fluid pressure applied on the ram, $R_r$ is the ram radius, and $R_p$ is the piston radius.

The real pressure applied to the sample is smaller than the ideal pressure mostly because of shear strength of the pressure medium. Mechanical friction in the hydraulic press and the pressure assembly are very small (Boyd and England, 1960; Bohlen, 1984). The amount of overstepping over the nominal pressure to ensure that the sample is at the desired conditions is called "friction correction".

Several well-calibrated equilibria can be used to estimate the deviation from ideal pressure (Bohlen, 1984; Mattioli and Bishop, 1984). The reaction:

$$Ca_3Al_2Si_3O_{12} \ + \ SiO_2 \ = \ CaAl_2Si_2O_8 \ + \ 2CaSiO_3 \qquad\qquad (A.2)$$

$$\text{grossular} \quad + \quad \text{quartz} \quad = \quad \text{anorthite} \quad + \quad \text{2wollastonite}$$

was used for this calibration because the pressure range of this equilibrium covers the pressures used in the experiments, and because the same equilibrium was used to

157

calibrate previously used assemblages, providing reasonable starting points for the calibration.

Mattioli and Bishop (1984) provided an empirical, linear P-T equation for the reaction based on a compilation of experimental data (P = 26.26T -13.827; P in bars, T in °C). They assumed that the shear strength depends only on temperature and, accordingly, calculated a linear function to estimate the real pressure applied on the charge from the pressure applied on the ram. They conclude that, for their assemblies and using the "hot piston-in" technique (i.e., sample is heated first and then pressurized), the correction factor was 17% at 1050 °C and nearly zero at 1300 °C.

A similar procedure is used here to estimate the friction correction factor of the pressure assemblies.

## A.2. Procedure

Starting material for the calibration was prepared by mixing approximately 234 mg of grossular, quartz, anorthite, and proto-wollastonite (which transforms to wollastonite at the calibration pressures) in stoichiometric proportions (103.34 mg grossular, 13.78 mg quartz, 63.83 mg anorthite, and 53.30 mg proto-wollastonite). R.W. Luth provided the phases used in the mixture; details on their preparation can be found in Nair (2000). This starting mixture was analyzed by X-ray powder diffraction and the obtained pattern was used as a basis of comparison to determine the direction of the reaction.

Aliquots of the mixture were fitted into 2 mm OD platinum capsules and welded shut. The capsules were enclosed into 19 mm pressure assemblages containing a rod of soft alumina to ensure that the capsules were positioned within 2-3 mm of the thermocouple junction.

158

Samples were run at 1100 °C and 1250 °C and different line pressures to estimate equilibrium at those temperatures. The "hot-piston-out" technique[2] was used to obtain the desired P-T conditions and samples were run for 24 hours. Run products were analyzed by XRD in the same fashion as the starting mixture. The ratio of the relative intensities of the main peaks for grossular (d = 2.65) and anorthite (d = 3.18) were compared with the ratio of the starting mixture (3.15) to determine the direction of the reaction. Changes smaller than 10% in this ratio were deemed to represent equilibrium conditions.

## A.3. Results

Results of the calibration are shown in Figure A.1. The results show that assemblies with inner parts made of magnesium oxide behave much closer to ideal than those having Alsimag components. For example at 1050 °C Mattioli and Bishop (1984) used a pressure correction of 17% whereas the assemblies calibrated here would require only 3% correction at that temperature. As noted by Mattioli and Bishop (1984) the friction correction decreases with increasing temperature. Table A.1 shows that for temperatures above 1250 °C no pressure correction is needed, a condition that applies for all the experiments presented here. Application of uniform pressure corrections as a percentage with disregard to temperature could potentially result in more error than using nominal pressures, especially when extrapolating to high temperatures to which unrealistic "negative" pressure corrections would be applied.

Table A.1. Friction correction (in %) for different assemblies as function of temperature.

| T (°C) | M-B '84 | Hauth '91 | this work |
|--------|---------|-----------|-----------|
| 1050 | 17 | 11 | 2 |
| 1100 | 12 | 8 | 2 |
| 1150 | 8 | 5 | 1 |
| 1200 | 4 | 3 | 1 |
| 1250 | 1 | 1 | 0 |
| 1300 | -2 | 0 | 0 |
| 1350 | -4 | -2 | 0 |

[2] "Hot-piston out": samples are pressurized to ~1.7-2 times desired pressure, then heated. Final pressure is obtained by decreasing line pressure, hence moving the piston outwards.
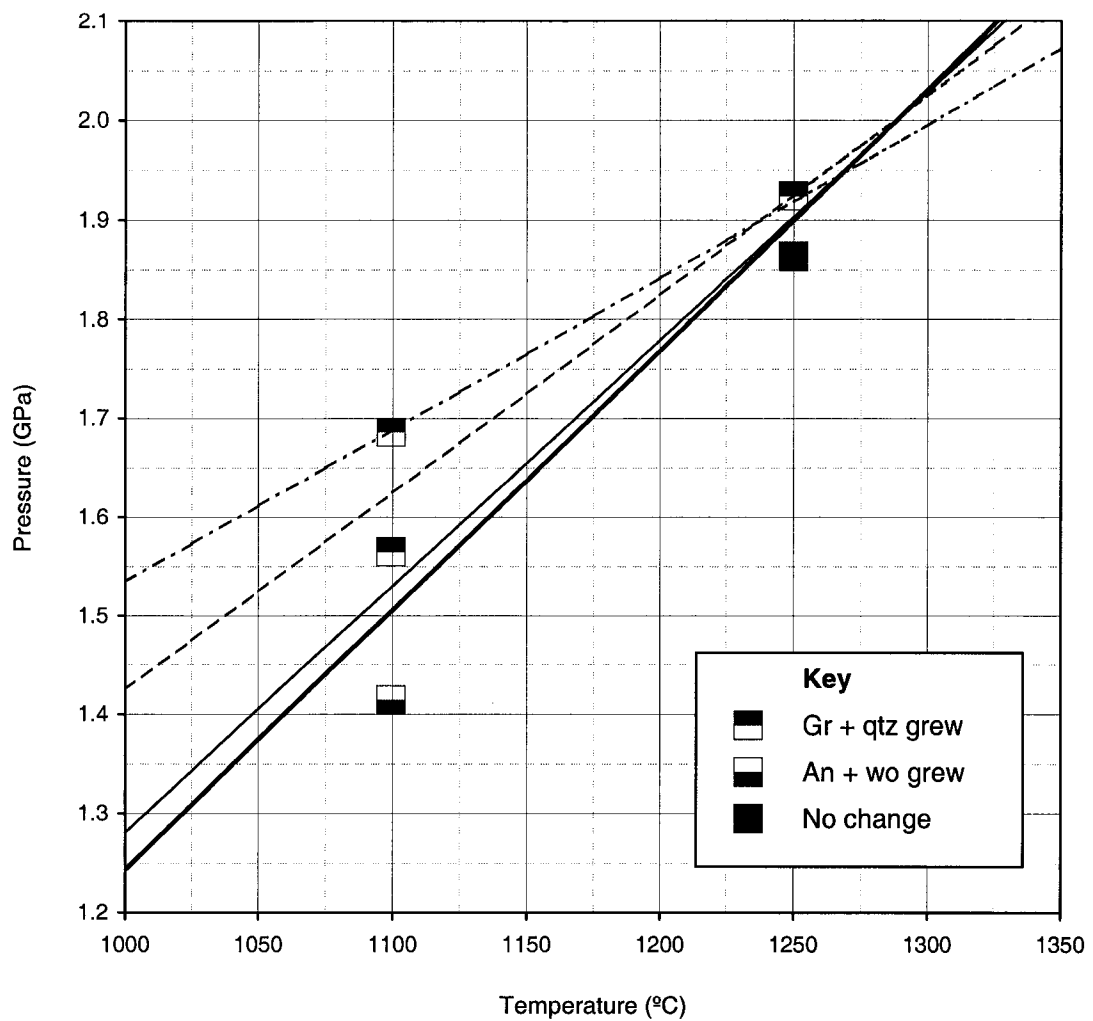
Figure A.1. Results of the calibration for the 19 mm assemblies (0.75") with MgO inner parts and comparison with nominal values and results of calibration for other assemblies using Alsimag components.